August 2021

MFL-based Detection of Flaws of Pre-stressed Concrete Girders

Azam Elyasigorji
University of Wisconsin-Milwaukee

MFL-BASED DETECTION OF FLAWS OF PRE-STRESSED CONCRETE GIRDERS

by

Azam Elyasigorji

A Dissertation Submitted in

Partial Fulfillment of the

Requirements for the Degree of

Doctor of Philosophy

in Engineering

at

The University of Wisconsin-Milwaukee

August 2021

ABSTRACT

MFL-BASED DETECTION OF FLAWS OF PRE-STRESSED CONCRETE GIRDERS

by

Azam Elyasigorji

The University of Wisconsin-Milwaukee, 2021
Under the Supervision of Professor Al Ghorbanpoor

Magnetic-based methods to evaluate structural defects have gained interest over recent decades. Magnetic flux leakage (MFL) has been used as an important nondestructive evaluation (NDE) method for detection of structural flaws such as surface cracks or corroded regions. MFL has been studied through experimental works, numerical simulations, and field testing for flaw detection. This work utilizes experimental results and 3-D finite element simulations to develop a methodology for flaw detection in pre-stressing steel in concrete members. MFL occurs after magnetic saturation of the defect region through the application of a strong DC magnetic field. Hall-effect sensors are located in the MFL apparatus, which also contains two blocks of strong DC magnets, to measure the vertical magnetic field variation. The superposition of the individual effects of stirrups and flaws on the MFL signal is validated by comparing signals given from experiments, numerical simulation, and an analytical method. A 3-D analysis of MFL signals is developed to determine the position and orientation angle of stirrups in addition to initial estimate of a flaw's location along the sample. The 2-D analysis of the MFL signals characterizes the flaw more accurately and identifies geometric properties of flaws. From experiments and numerical

simulations, the MFL-related properties of flaws are tabulated and visualized for several section loss percentages and lengths of flaws as well as the various distances between the magnet blocks and embedded strands within concrete. The methodology suggested by this work determines the stirrups' position and orientation with good accuracy and detects and estimates the level of corrosion in embedded prestressing steel in pre-stressed concrete girders.

TABLE OF CONTENTS

LISTP OF FIGURES

LIST OF TABLES

ACKNOWLEDGEMENTS

I would like to thank my supervisor, Professor Al. Ghorbanpoor for guiding and supporting me over the years. You have set an example of excellence as a researcher, mentor, and instructor.

I would like to thank my thesis committee members for all of their guidance through this process; your discussion, ideas, and feedback have been absolutely invaluable. In particular, I would like to thank Professor Tabatabai. Your constant enthusiasm, encouragement, and mutual scientific understanding are exemplary.

I would like to thank Mrs. Elisabeth Warras.

I would like to thank Dr. Marjorie Piechowski for her help in editorial section.
I would like to thank Mr. Rahim Reshadi for his great helping hand, considerations, and attention in the structural lab.

I would like to thank my husband, Maysam Rezaee, and sister, Farzaneh Elyasigorji for their love, support, and patience. Maysam, thank you for being such an equal partner; for loving me without wavering and for accepting me without questioning.

I also appreciate all the support I received from the rest of my family, particularly, my dear parents Firoozeh and Es'hagh, who revived my burned body with their love, and have humbly supported me and taught me to work hard to grab my achievements.

Chapter 1 **INTRODUCTION**

1.1 **Motivation and objectives**

Reinforced concrete bridges as a key component of worldwide transportation systems have been built during the last century and are expected to resist several types of loads such as traffic (including loads from moving vehicles and fatigue-related effects), gravity, seismic, meteorological (such as wind, snow, rain, temperature gradient, freeze and thaw cycles, and chemical attacks), and long-term effects (or deteriorations).

After prestressed concrete was introduced, using pre/post-stressed strands in concrete girders became popular because of their high load-carrying capacity, which allows the use of long spans for concrete bridges. Despite all the advantages of prestressed concrete components, the corrosion of embedded steel has remained as the main concern during the lifetime of such structures. Corrosion causes section loss in steel that degrades the serviceability of a prestressed member through capacity reduction (Al Ghorbanpoor, Borchelt, Edwards, & Abdel Salam, 2000; Kamaitis, 2002). On the other hand, the gradual growth of corrosion in steel strands or rebars could significantly reduce the load-carrying capacity of prestressed concrete components by decreasing the bonding of strands and concrete, potentially causing a failure by concrete brittle fracture. Several corrosion-related collapses of bridges in the US and abroad have been reported in the available literature. Florida Department of Transportation (FDOT) has reported corrosion-related

failures of post-tensioned steel strands in the Niles Channel Bridge, Mid Bay Bridge, Sunshine Skyway Bridge, and Garcon Point Bridge. Virginia Department of Transportation (VDOT) has reported corrosion of post-tensioning tendons in the Varina-Enon Bridge. At the time of corrosion detection, these bridges were in service for only between 7 to 18 years (Permeh, Vigneshwaran, Echeverría, Lau, & Lasa, 2018).

The main objective of this work is to develop an effective corrosion (or flaw) detection methodology that will allow bridge owners and engineers to assess the structural condition assessment of prestressed concrete girders. This is achieved based on performing magnetic flux leakage (MFL) laboratory testing and Finite Element (FE) simulation. Employing a MFL system of non-destructive testing (NDT), FE simulation, and mathematical data analysis methods, a methodology is proposed to characterize the corroded region of strands in prestressed concrete members. In particular this study has demonstrated the use of MFL as a reliable NDT technique for detection and estimation of the extent of corrosion in embedded prestressing steel, crack detection on the metal surface or welds, defects in pipelines, and defects in steel within conventional reinforced concrete members (Antipov & Markov, 2014; Mandal & Atherton, 1998; Okolo & Meydan, 2018; Zhou, Qiu, Zhou, Zhou, & Xia, 2018).

1.2 **Proposed research**

To address the issue of corrosion detection in prestressed concrete girders, using an MFL measurement system, a series of laboratory experiments is performed to determine the corrosion effects and evaluate the influencing parameters.

The MFL method is based on applying a powerful magnetic field close to the ferrous parts and monitoring the field variations due to changes in the cross-section of parts. Since a near magnetic saturation of ferrous material is necessary for the flux leakage to occur, using a strong

magnetic field is required for an effective MFL system. A system including two powerful DC permanent magnet blocks, a package of electronics, and mechanical components (to support and control the system) has been used to evaluate the magnetic field near the strand surface.

A major influencing factor in the MFL data acquisition and analysis is the distance between each point of data measurement and the magnetized strand that includes one or more flaws. In prestressed concrete girders, it is usual to place the strands in multiple layers. Therefore, detection of defects in strand layers farther from the MFL test device becomes more difficult as the distance between each point of measurement and a flawed strand increases. Also, any discontinuity or sudden volumetric change in the steel (such as when stirrups or chairs are present) will cause an additional flux leakage. This normally results in superposition of additional magnetic signals on the actual flaw signals that cause more complexities in the MFL signal analysis and interpretation.

To overcome the issue, mathematical data analysis methods such as signal processing or pattern recognition are used to filter, or remove, the effects of undesirable pulses resulted by the presence of stirrups, chairs, and other artifacts for each test. The wavelet technique may also be used to digitally remove noise signals from actual flaw signals, or median filters to remove outliers or spikes. Finally, by utilizing an Improved Correlation Analysis, the corroded regions are characterized by finding their location, maximum loss of section, and length.

3-D transient magnetic finite element analyses (through ANSYS Maxwell) are conducted to simulate the experiments. After validating the simulation results from appropriate experiments, the FE analysis is extended to evaluate multiple other cases for which laboratory testing is not feasible.

Chapter 2 **Non-Destructive Evaluation Methods**

2.1 **Introduction**

As an integral part of transportation system, bridges are carrying significant portion of overall traffic in the US (and all around the world). Reporting from American Road & Transportation Builders Association (ARTBA), more than 45,000 structurally deficient bridges in poor condition (as shown in Figure 2-1) are carrying more than 170 million daily crossing in the US transportation system ("ARTBA Bridge Report," 2020). The replacement or rehabilitation of these bridges requires a huge annual budget as estimated by National Bridge Inventory (NBI) in order of $25 billion for replacement and $17 billion for rehabilitation in the US for 2020 ("Bridge Replacement Unit Costs 2020 - Federal Highway Administration," n.d.). Effective diagnostic methods help to reduce the replacement and rehabilitation costs in addition to increasing the serviceability age of existing bridges. With the general terms of structural health monitoring (SHM) and non-destructive evaluation (NDE), numerous methodologies have been developed for detection of structural defects to avoid infrastructures from major deficiency of collapse.

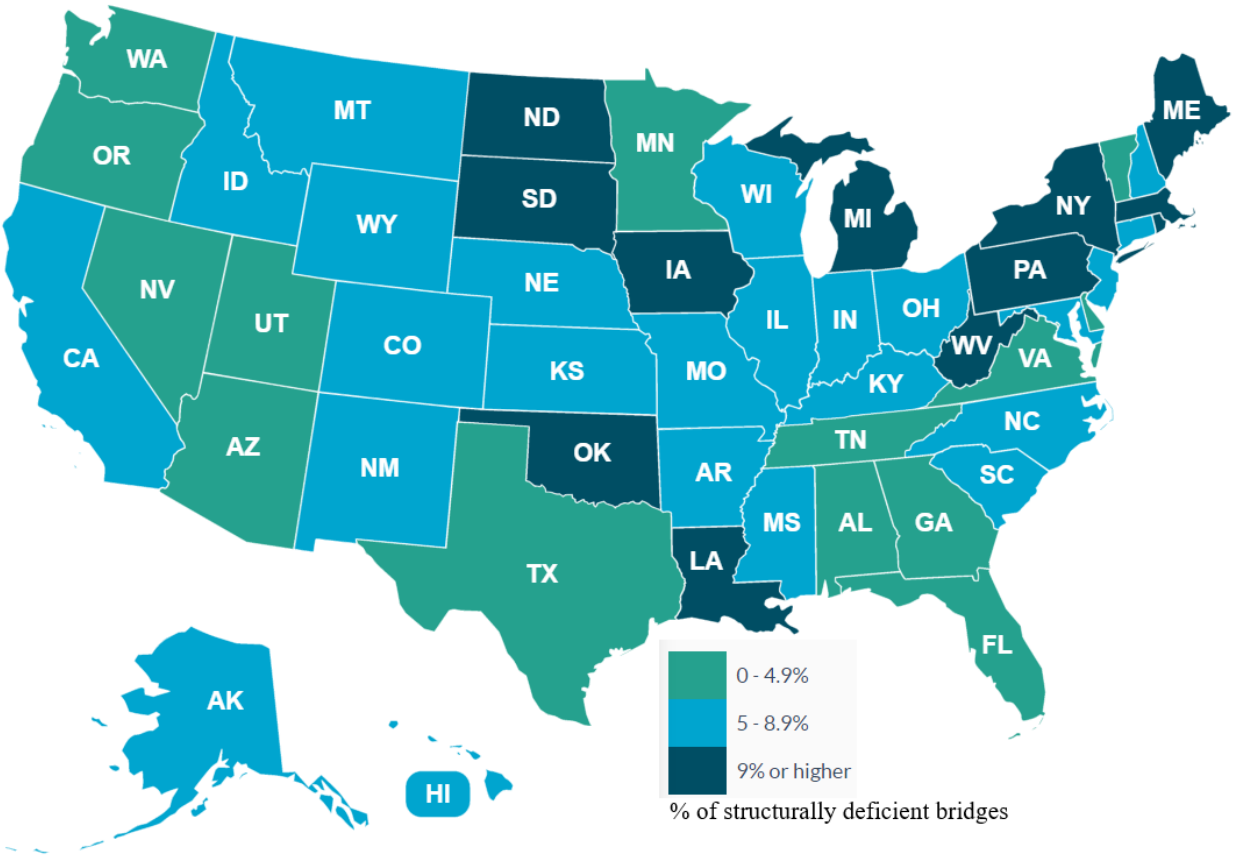

Figure 2-1: Structurally deficient bridge map in the US ("ARTBA Bridge Report," 2020)

Implementing an appropriate non-destructive evaluation (NDE) approach in infrastructure prevents structural collapse caused by service loads and natural disasters. Also, employing a proper NDE method will enhance the reliability and lifetime reliability of infrastructures. In what follows, a reliable, time-saving, and cost-effective NDE method is proposed to detect metal losses due to corrosion or cracking problems in prestressed steel strands embedded in concrete to assure safe operation of prestressed (PS) concrete structures.

There are two general approaches to evaluate the performance of PS concrete structures during their service life. The first is the invasive approach where partial undesirable damage is introduced in structural elements through taking samples or material removal or excavation. The

second, known as the NDE method, uses various technologies to detect defects in a structure non-destructively.

Using NDE methods allows discontinuities or flaws to be detected and evaluated without any damage to the structure. Through research and various laboratory and field applications over the last several years, it has been shown that NDE methods are valuable maintenance means that can maintain infrastructures in a safe and serviceable condition (Beattie, 2013; Krause et al., 2002).

2.2 Visual Testing (VT)

The visual or optical assessment of an object to monitor specific parameters is called Visual Testing (VT). This method is an important and complementary part of many other NDE methods such as magnetic particles, penetration, ultrasonic inspection, and radiography. Identifying the size, quantity, color, function, surface finish, shape, deformity, leakage, and surface discontinuities are the goals for using a visual testing method.

This method is one the most common and powerful NDE tools that requires illumination of the test surface and proper eyesight of the tester (IAEA, 2013). Two general types of direct visual testing and translucent (or remote) visual testing are currently used. This method usually needs simple equipment (as shown in Figure 2-2). For example, for internal inspection, light lens systems such as borescopes allow remote surfaces to be examined.

The following are some applications of this method:

a) The surface condition of a component

b) Alignment of mating surfaces

c) Shape of component

d) Internal side defects

e) Evidence of Leakage

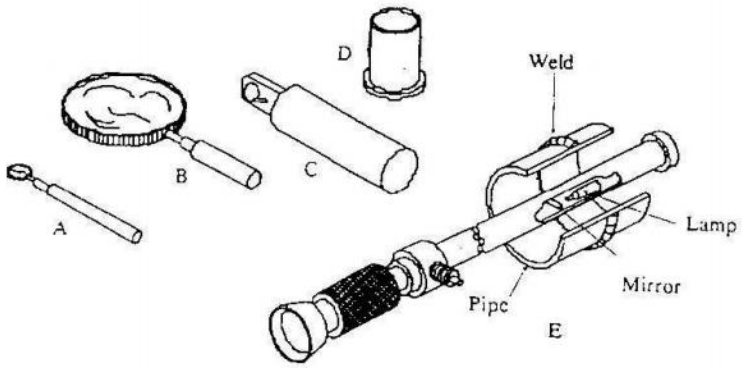

Figure 2-2: Visual Testing Equipment (IAEA, 2013)

Advantages of the visual method include a simple process, high speed, and availability of permanent records. Limitations include detection only of surface flaws, weakness of eye resolution, and eye fatigue.

2.3 **Acoustic Emission Testing (AE)**

This method works on the concept of short-lived and high-frequency released elastic waves (or energy) generated by the material subjected to external stress such as an abrupt mechanical load or temperature variation (Manson, Worden, Holford, & Pullin, 2001; Verstrynge, Lacidogna, Accornero, & Tomor, 2021). The acoustic emission was recognized by early miners who exited a mine when the rocks or supporting timbers started groaning. On the other hand, when a structure is unloaded, there is no acoustic emission and no ability to detect any discontinuities (James Li & Li, 1995).

The principle of the acoustic emission method is based on the dynamic input sources that produce a stress wave to form, transmit along with the structure, and create a transient surface displacement that is recorded by the sensors. Since the piezo-electric crystals create a voltage when they are being actuated by a transient surface strain, they are the typical material for acoustic

emission sensors (Schumacher, 2009). This method is applicable in aerospace industries and prestressed components such as prestressed concrete decks of slabs.

2.4 Guided Wave Testing (GW)

GW is a method of evaluating the reflected waves from controlled excited ultrasonic waves passed through a conductive medium such as a piping system. Since the late 1990s, GW has been popular because of the quick monitoring of long pipelines. The feasibility of remote screening of long pipes is one of the main advantages of this method (Demma et al., 2007). This method is applicable for pipeline inspection and monitoring, as well as boiler tube inspection, heat exchanger tube inspection, plate structure inspection, buried anchor rod inspection, suspension bridge cable inspection, and monitoring of matrix breakage in composite structures.

2.5 Thermal/Infrared Testing (IR)

Acquisition and processing of thermal information from non-contact measurement devices is a technique used for infrared thermography or thermal/infrared testing. This type of testing is based on infrared (i.e., below red) radiation with a longer wavelength than visible light. Emission of infrared radiation is possible for any object with a temperature higher than absolute zero.

The advantages of the IR method are the non-contact technology, two-dimensional thermal image, high-speed scanning of a target in real-time, no harmful radiation effects, and a non-destructive method, which is applicable in crack detection, medical preventing screening, and measurement of an animal body's temperature.

This phenomenon could be described by three factors: the spectral absorptance α_λ, which is the ratio of the spectral radiant power absorbed by the object, the spectral reflectance ρ_λ, which is the ratio of the spectral radiant power reflected by the object, and the spectral transmittance τ_λ, which is the ratio of the spectral radiant power transmitted by the object. These three parameters

are wavelength dependent. The sum of these three parameters must be one at any wavelength (Usamentiaga et al., 2014):

$$\alpha_\lambda + \rho_\lambda + \tau_\lambda = 1$$

Different thermal behavior of internal objects and flaws are the theoretical principle of this method. The defect (or flaw) affects the flow of the heat source because the test sample is heated or cooled at different rates, leading to the temperature difference on the surface (because of different radiation emissions), which can be screened by the infrared cameras. Figure 2-3 shows the schematic setup of an active IR inspection process.

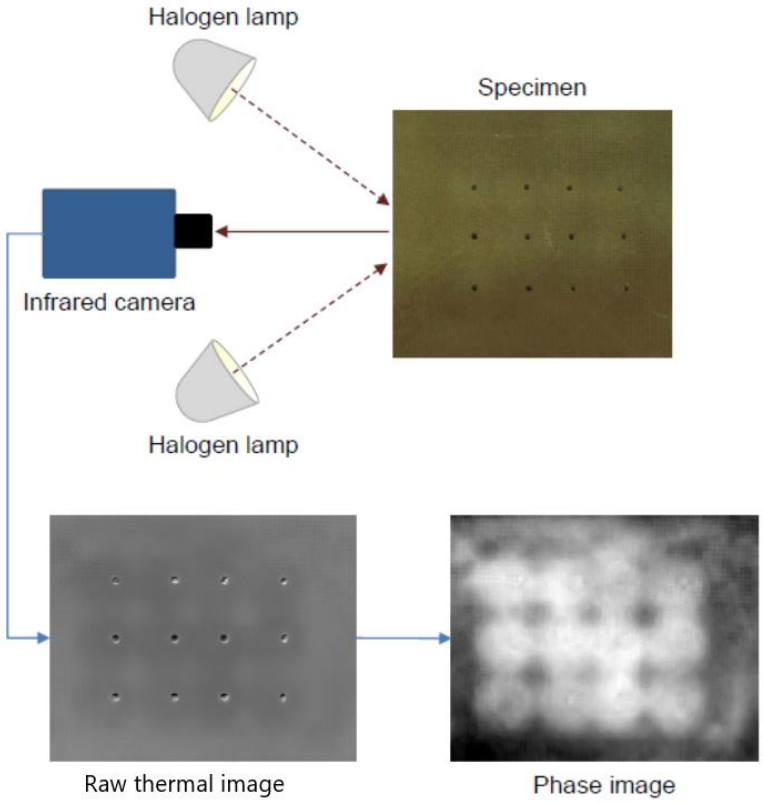

Figure 2-3: Schematic View of IR Method (Usamentiaga et al., 2014)

2.6 Ultrasonic Testing (UT)

Ultrasonic refers to sound waves of frequency greater than 20kHz. This frequency provides an appropriate penetrating power (Lohith, 2009). As shown in Figure 2-4, the energy reflects when

sound waves propagate from one medium to another one and the rest of waves will transmit at the interface.

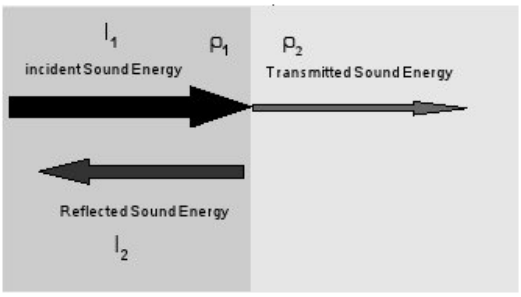

Figure 2-4: Sound Wave Propagation Through Two Media (Lohith, 2009)

This method works for detecting flaws since flaws can reflect ultrasonic energy. Higher frequencies produce stronger sound energy; therefore, the range of 0.5 MHz to 25 MHz is an appropriate ultrasound frequency. A particular shape of piezoelectric crystals or an electromagnetic acoustic transducer can be used as an actuator for sound waves (Lohith, 2009). The relation among the intensities of the incident and the reflected sound energy is given by:

$$I_2 = I_1 \left(\frac{\rho_1 - \rho_2}{\rho_1 + \rho_2} \right)^2$$

ρ_1 and ρ_2: densities of two media

I_1 and I_2 : intensities of sound in two media

Advantages of this method include sensitivity to both surface and subsurface discontinuities, high depth of penetration, highly accurate results, and minimal part preparation. However, direct access to the surface, the necessity for skill and training, ineffectiveness on rough or irregular surface shapes, and inability to detect flaws parallel to sound waves are some important issues of UT testing.

2.7 Radiography Testing (RT)

In this method, the under-inspection part is placed between a radiation source and a sensitive film. X-rays or gamma-rays can be employed as the radiation source (as shown in Figure 2-5). The energy level of the radiation must be well chosen so that sufficient radiation is transmitted through the object onto the detector (Rockley, 1977).

Surface and internal inspection, detection of significant variation of composition, few material limitations, ability to scan for hidden regions, and very minimal part preparations are some advantages of radiography testing. Alternatively, health issues for operators, the need for a high degree of skill, expensive equipment, and sensitivity to the orientation angle of the flaws, and required two side access are some disadvantages of this method.

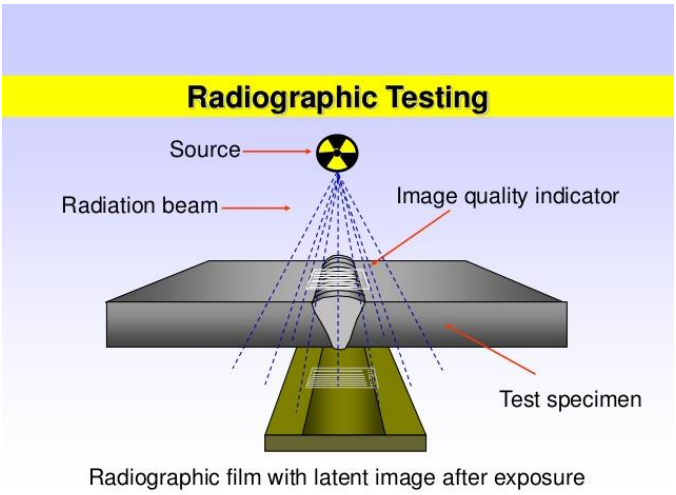

Figure 2-5: Schematic View of Radiographic Testing ("Radiographic Testing – SITAS," n.d.)

2.8 Magnetic Flux Leakage (MFL)

Most of the NDE methods are inspired by physical phenomena such as the wave propagation characteristics in materials or magnetic field properties. The Magnetic Flux Leakage (MFL) method is an electromagnetic NDE technique (S. H. Park, Kim, Nam, & Lee, 2012; S. Park, Kim, Lee, & Lee, 2014; Wang, Gu, & Wang, 2012) that is most suitable for detection of corrosion

and fracture in structures or members such as steel rebars and cables in RC[1] parts, prestressed concrete bridges, and pipes. The MFL has been applied for the inspection of steel cables in the mining industry, for ski lifts, elevators, and other applications (S. Park et al., 2014). The MFL technique is the only effective NDE method available to detect flaws in steel strands embedded in prestressed concrete bridges.

2.9 Other NDE Methods

Recently, many other NDE methods are being used with increasing numbers. They are mostly inspired by natural phenomena for specific applications. The following is a list of some other NDE methods that currently are used:

- Electromagnetic Testing (ET)
- Ground Penetrating Radar (GPR)
- Laser Testing Methods (LM)
- Leak Testing (LT)
- Microwave Testing (MT)
- Liquid Penetrant Testing (PT)
- Magnetic Particle Testing (MT)
- Neutron Radiographic Testing (NR)
- Vibration Analysis (VA)

[1] Reinforced Concrete

Chapter 3 **Magnetic Flux Leakage**

3.1 Introduction

The previous chapter presented a brief review of different NDE methods. Most NDE methods require the operator to have direct access to the deteriorated material (or flaw) surface to assess the condition of the material or member. This is not possible for corrosion detection in reinforcing steel that is embedded in concrete. The magnetic flux leakage (MFL) technique, however, is a suitable non-contact NDE method that has shown success for detection of corroded regions embedded in concrete (A. Ghorbanpoor, Steber, & Shew, 1991; Krause et al., 2002; Sawadw & Krause, H, 2010).

3.2 The Concept of MFL

Using the MFL method, a ferrous material, such as a prestressed steel strand, is magnetized with a powerful magnetic field up to the saturation level, and any discontinuity of the geometry such as corrosion, cracks, fractures, or rust pitting leads to the leakage of the magnetic field that can be detected by appropriate magnetic sensors (Belblidia et al., 2015).

In ferromagnetic materials, the atomic dipoles are normally oriented in random directions. By applying a magnetic field, the magnetic dipoles are aligned and oriented in the same direction as the magnetic field, as shown in Figure 3-1(a) and (b) (Ghorbanpoor, et al., 2000). This alignment permits magnetic flux to pass through the material without interruption if there are no discontinuities or flaws. Otherwise, the magnetic flux lines will leak out, as shown in Figure 3-2. The larger the flaw, the more leakage of flux lines.

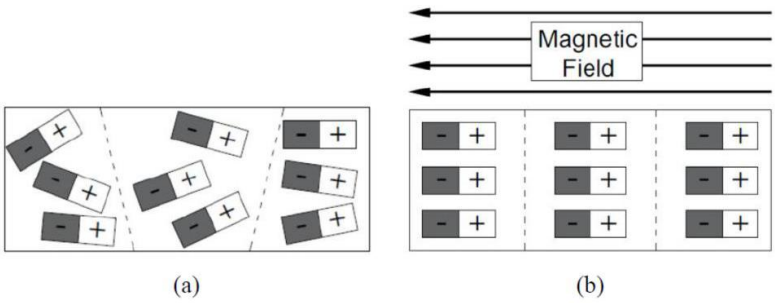

Figure 3-1: Alignment of Dipoles; (a) Before Applying Magnetic Field, (b) After Applying Magnetic Field

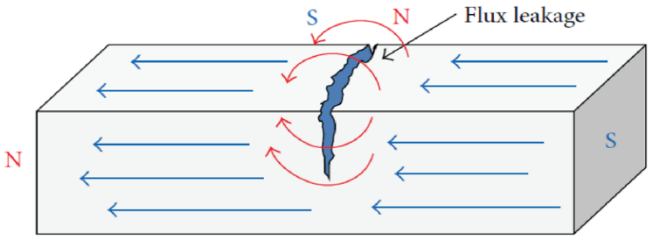

Figure 3-2: Schematic View of Magnetic Flux Leakage (S. Park et al., 2014)

The saturation level of materials strongly depends on the relationship between the magnetic flux density (B) and the magnetic field strength (H). Ferrous materials generally exhibit a nonlinear B-H curve. This may be seen for structural steel, as shown in Figure 3-3. The diagram shows that a field strength of at least 2.4 Teslas is needed to reach out to the full saturation point in structural steel. A magnetic field with an approximate intensity of 3.00 Tesla is used for reducing noises from data acquisition systems. To employ the MFL method, it is necessary to measure the magnetic field changes near flaws or discontinuities in ferromagnetic materials.

In general, the magnetic flux may be obtained by $\mathbf{B} = \mu.\mathbf{H}$ where **B** is the magnetic flux intensity (weber/m^2), μ is the magnetic permeability of the material (weber/Ampere-m), and **H** is the magnetic field strength (Ampere/m). When the magnetic flux lines encounter any discontinuity, for example, corrosion or fracture of a test component such as a prestressed steel strand, all or some parts of the magnetic flux leaks out of the material and into the surrounding media, such as air. The leakage field is detected by appropriate magnetic sensors.

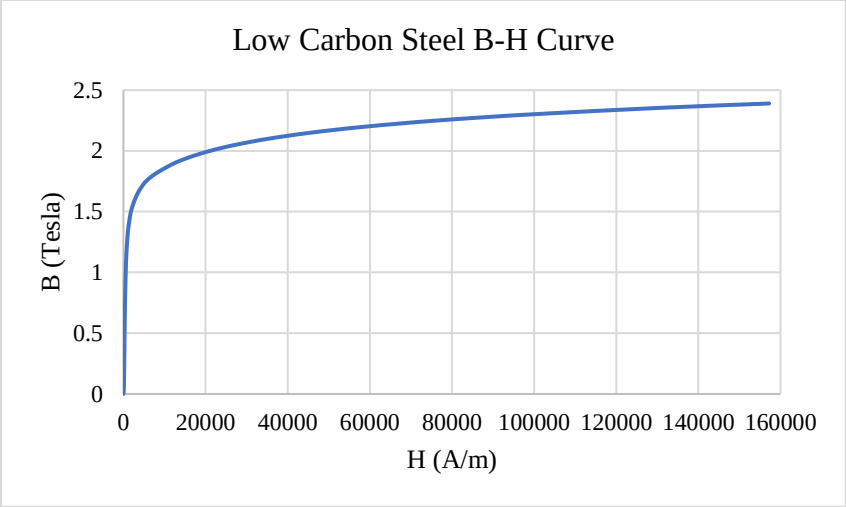

Figure 3-3. Non-linear B-H Curve of Low Carbon Steel

In practice, an MFL test system is used to continuously scrutinize the surface of the concrete member that includes the embedded strands and measure the magnitude of the leakage field by magnetic sensors. The most suitable and field-worthy magnetic sensors for such applications have proven to be the Hall-effect sensors, which are usually installed in a plane near and parallel to the concrete surface and at the mid-point between the two DC permanent magnets for the MFL system. Small Hall-effect sensors (1 mm by 1 mm in size) are normally laid out in a horizontal or flat orientation where they can sense the magnetic flux passing perpendicular to their surface. This sensor orientation allows the vertical component of the leakage field (B_z) to be detected. Recent studies have shown that flux leakage changes in the longitudinal, or horizontal, direction (B_y) can enhance data interpretation to detect and estimate flaw sizes (Belblidia et al., 2015; Okolo & Meydan, 2018; Shi, Zhang, Li, Cai, & Jia, 2015). The B_y component may be detected by orienting the hall-effect sensors on a vertical plane.

3.3 Application of the MFL Technique

Several studies have been completed on the detection of internal and surface cracks and corrosions in the metal members such as piping systems (Belblidia et al., 2015; Okolo & Meydan, 2018; Shi et al., 2015). For inspection of ferromagnetic members using the MFL technique, the

apparatus should be kept in proximity of the member to allow an effective detection process. In prestressed concrete girders, the closest steel strands to the concrete surface are covered by a concrete layer with a thickness of more than 2.0 inches. An increase in the distance between the points of measurement and the test piece leads to detection challenges requiring the use of stronger magnets, more complex instrumentation, and encountering undesirable interfering noise from the effects of other ferromagnetic components.

The MFL apparatus used in this study consisted of two DC permanent magnets, which were placed with a 7-inch clear distance between two magnets, and a set of Hall-effect sensors and supporting electronics, as shown in Figure 3-4 (Elyasigorji, Rezaee, & Ghorbanpoor, 2019). The system was previously fabricated at the University of Wisconsin-Milwaukee under Professor Ghorbanpoor direction.

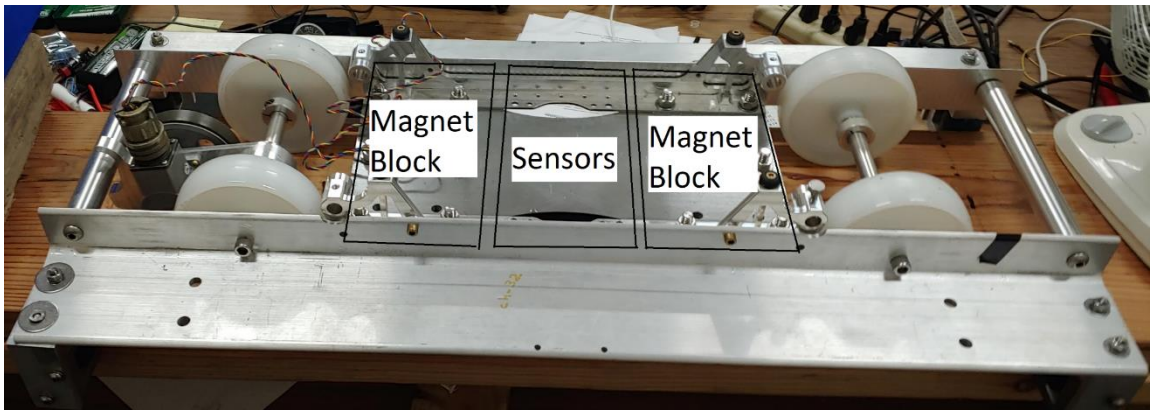

Figure 3-4: Prototype of Magnetic Blocks and Sensors (Elyasigorji et al., 2019)

Hall-effect sensors are placed along a line mid-way between the two magnets. The sensors are in a line perpendicular to the longitudinal axis of strands, and they sense the variation of the magnetic field in both vertical and longitudinal directions.

Schematic views of the MFL apparatus are shown in Figure 3-5. The apparatus consists of two DC permanent magnets, a bottom steel plate, steel strands, stirrups, and sensors.

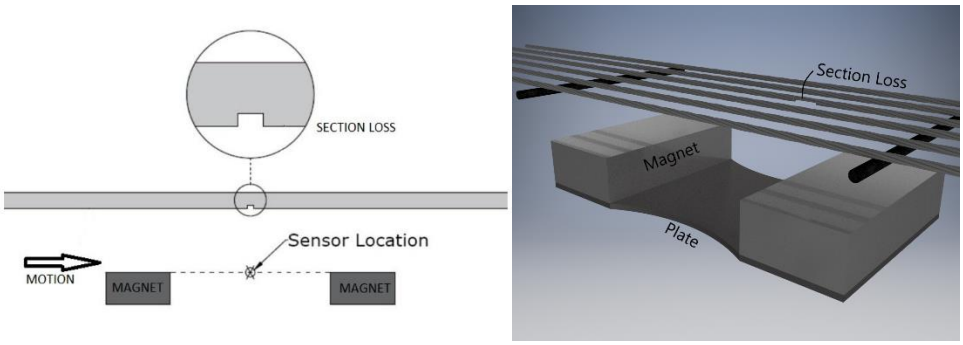

Figure 3-5: 2-D and 3-D Sketches of an MFL System

As shown in Figure 3-6, to facilitate an adequate level of magnetic field to penetrate inside test specimens, the magnet poles' orientation was selected with the north pole in one block and the south pole in the second block facing the test specimens. Therefore, moving the MFL apparatus through a corroded region causes flux leakage as shown in Figure 3-6.

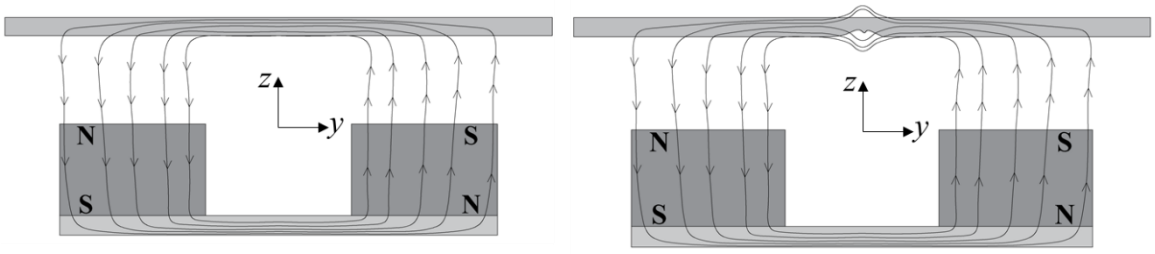

Figure 3-6: Schematic View of Flux Leakage

To measure the variation of the magnetic field along with a prestressed member in *y* and *z* axes, 32 hall-effect sensor channels were located for each direction. Therefore, for each of the *y* and *z* axes, 32 individual signals are given from the MFL system that contain variations of the magnetic field at the position of each channel. For example, Figure 3-7(a) and (b) show the variation of the magnetic field for the *y* and *z* axes, respectively, based on signals given from all channels. As expected, the sensors closer to the flaw measure stronger flux leakage. Two different patterns of signals are observed, which would be informative for further investigations. Most researchers have preferred the vertical component (*z*-axis) in their analysis for two reasons: 1) This component has a simpler pattern; 2) The *z*-component of the magnetic field has shown a larger

absolute variation than the *y*-component, which makes the signal analysis more facile. The variation of the resultant magnetic field (calculated as $\sqrt{B_x^2 + B_y^2}$) is shown in Figure 3-7(c), illustrating the 3-D variation magnetic field at a flaw position, which is analyzed later in this study.

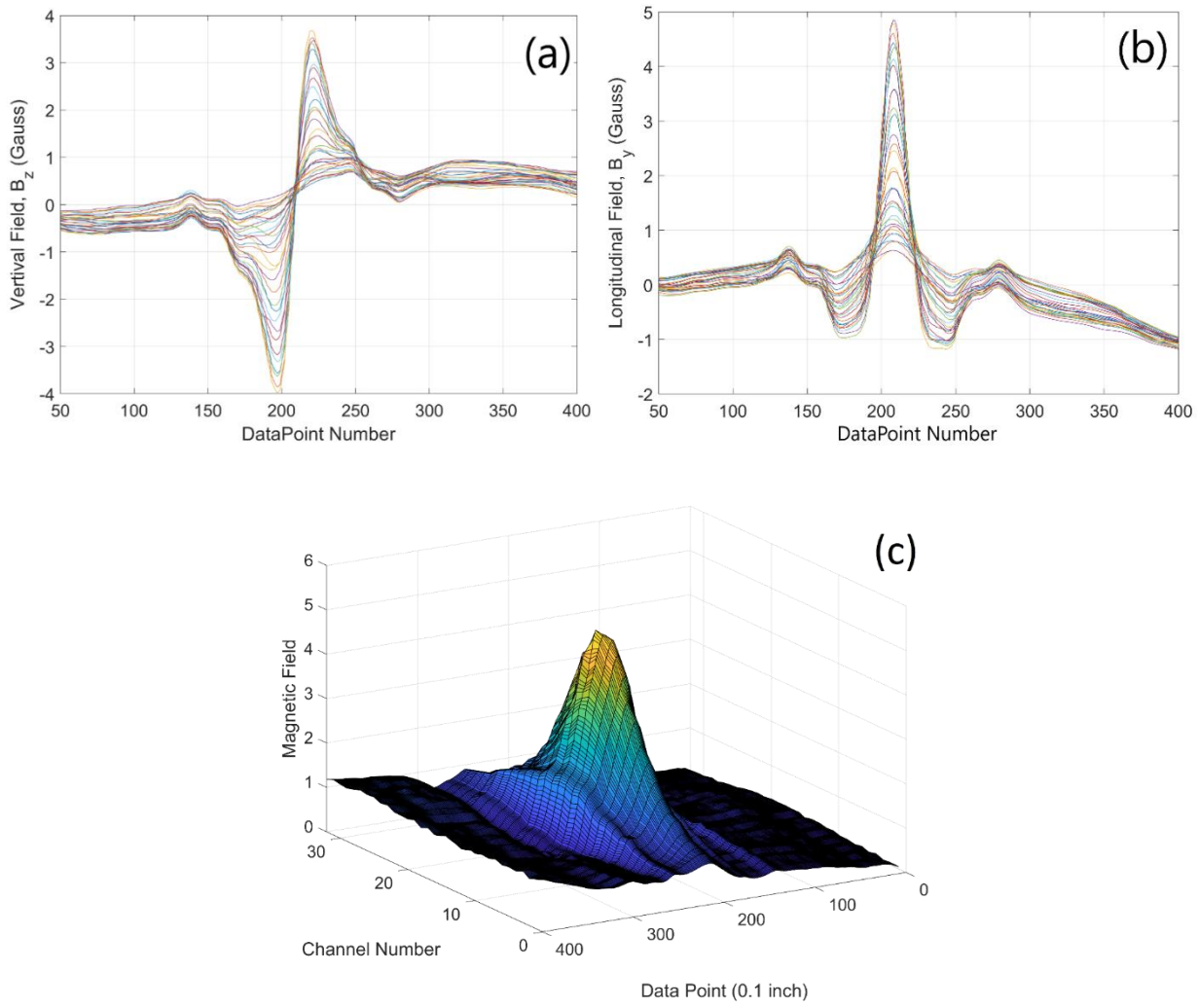

Figure 3-7: Signals for the Case of one Strand with no Stirrup Including a Flaw of 28% with One-Third of Inch Length; a) Vertical Component, b) Longitudinal Component, and c) Total Magnetic Field (B)

As explained earlier, the variation of the *z*-component of the magnetic field has a specific pattern (shown in Figure 3-8) that can be characterized with two parameters. The *amplitude* of the signal is defined as an absolute difference of the signal peaks and is quantified based on Gauss or Tesla. The *duration* of the signal is defined as horizontal distances of two peaks and is measured

by inch. The MFL system measures the magnetic field variation at each tenth of an inch while moving along test specimens.

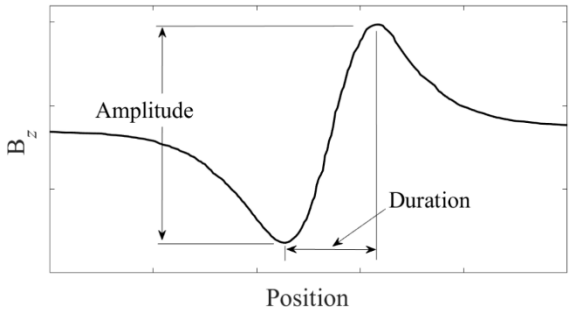

Figure 3-8: Signal Properties

The MFL apparatus moves through the prestressed concrete elements with a constant velocity. In fact, at the beginning of the experimental test, the initial acceleration makes significant changes in the magnetic field and the same fluctuations reoccur at the end of the test when the equipment stops. Figure 3-9 shows an output signal of the receptor of the Hall-effect sensor. The thicker blue curve indicates the central sensor. Highlighted red ellipses at the start and end parts of the graphs introduce the interruption from the acceleration effect at the start and end of the system's motion along the length of the test object.

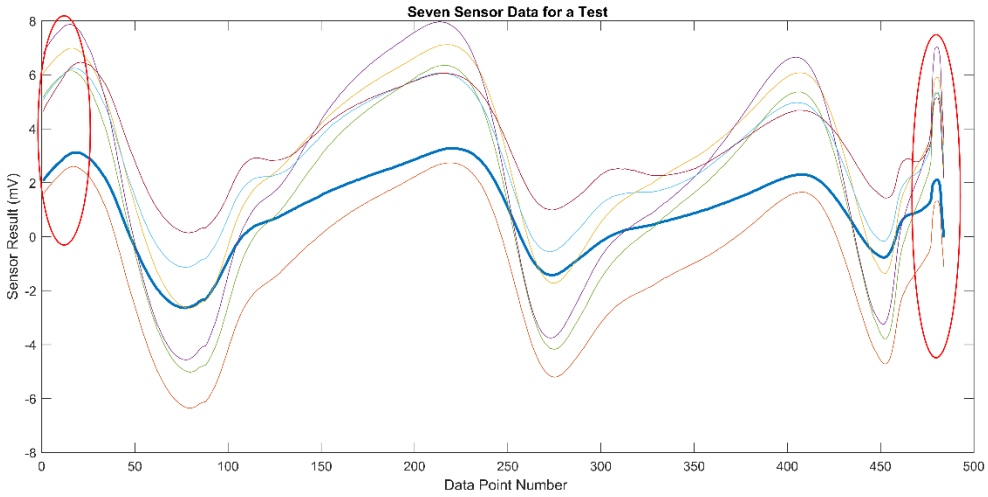

Figure 3-9: The Signal obtained from 32 sensors for a prestressed concrete beam

3.4 Magnetic Finite Element Method in Prestressed Concrete Beams

ANSYS Maxwell is a commercially available FEM software that is capable of simulating a magnetic flux leakage test for prestressed concrete girders under different influencing factors. Most of the previous numerical simulations of the MFL applications were conducted for the magneto-static 2-D simulations. In this study, 3-D transient finite element simulations are performed to evaluate the effect of various influencing parameters on MFL signals for the detection of flaws of steel strands embedded in concrete, as shown in Figure 3-10.

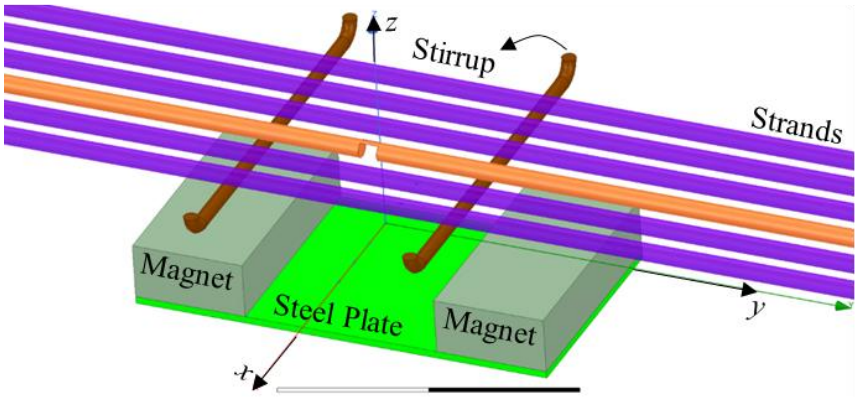

Figure 3-10: Simulation model view in ANSYS Maxwell

The simulation model may contain strands, stirrups, magnet blocks, a steel plate, and a sensor array. The orange-color strand may contain a section loss to model the flaw. The velocity of motion of the MFL system is set as 3 inch/sec for all simulation models. Since concrete is a non-ferrous material, in most cases, it is transparent to the magnetic field. Accordingly, it is modeled in the simulation as having the same characteristics as air. For a model such as the one shown in Figure 3-5, the flux density at the location of a Hall-effect sensor can be expressed by the following equation in which the $\boldsymbol{B_i}$ is the *i*-th component of Magnetic at the Hall Effect sensors field and *v* is the volume of the sensor:

$$B_i = \frac{\oint \boldsymbol{B_i} . dv}{\oint dv} , i = x, y, z \qquad 3\text{-}1$$

Figure 3-11(a) shows the results of FEM simulation for the magnetic field from two magnetic blocks where no steel strand is present. An adaptive FE mesh generation technique is utilized with less than 0.1% of error for total energy loss. Figure 3-11(b) and (c) also show the magnetic flux in two forms of streamlines and contour lines.

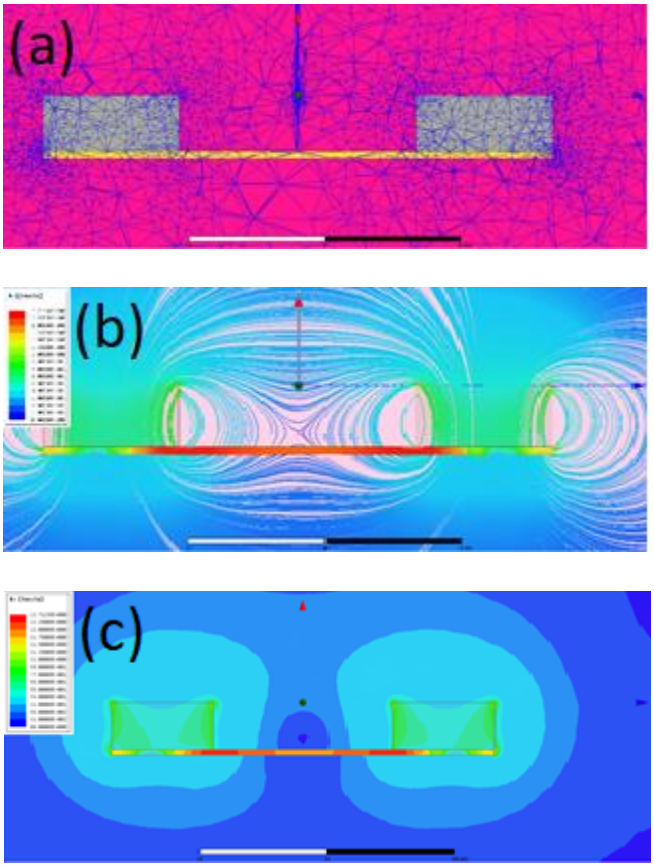

Figure 3-11: FEM field distribution simulating the resulting field from two magnetic blocks, after 15 cycles (a) fine FEM mesh, (b) magnetic field streamline, and (c) magnetic contour

In a follow-up simulation work, a steel strand with a flaw was included in the model; see Figure 3-12 and Figure 3-13. The simulation clearly shows the effect of the flaw in the strand, causing noticeable magnetic flux leakage that can be measured and correlated with the size of the flaw.

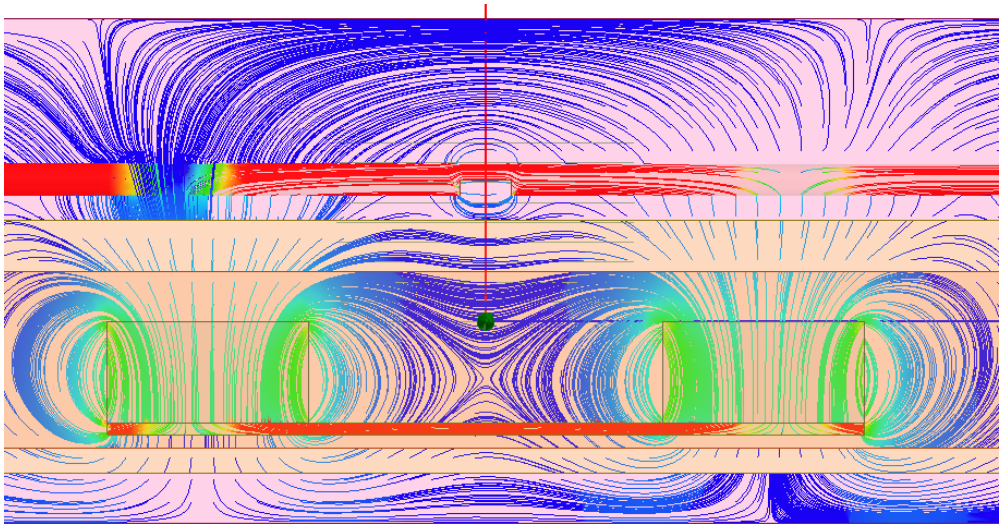

Figure 3-12: Magnetic fields changes due to MFL sensor detecting the presence of a flaw

As shown in Figure 3-13 by streamlines, the leaked flux has a magnitude much lower than the saturation level. Therefore, a strong magnetic field is required to bunch up around the corroded region to empower the ability of data reading. In the 3D transient model, the velocity of the magnets-sensors assembly is considered 3 inches per second, and data are recorded at each tenth of a second. The results of simulations are validated by experimental results.

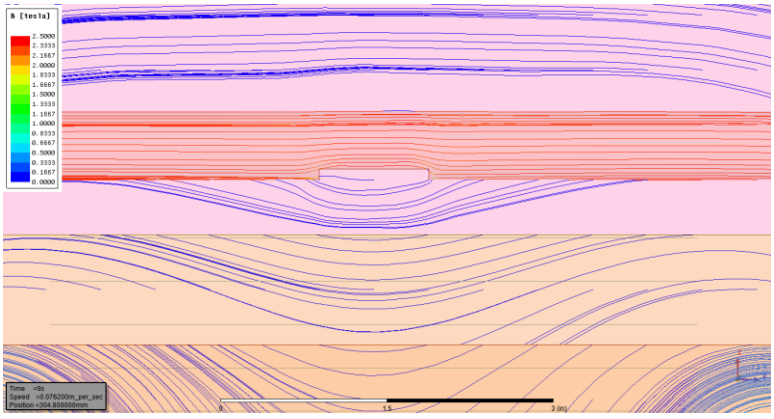

Figure 3-13: Flux leakage observed at the section loss

In real prestressed concrete elements, shown in Figure 3-14, there are two general types of reinforcements: 1) main flexural reinforcements that are parallel to the longitudinal axis of beams

(designed to resist against the bending moment); 2) the transverse reinforcements (stirrups) that are perpendicular to the beam's longitudinal axis and are designed to provide the girders' required shear capacity. Since the MFL system motion axis is parallel to the strands' longitudinal axis, a variation of the magnetic field will be sensed for any lateral or local volumetric changes of steel (or other ferrous) materials along the samples, such as stirrups, flaws, or chairs.

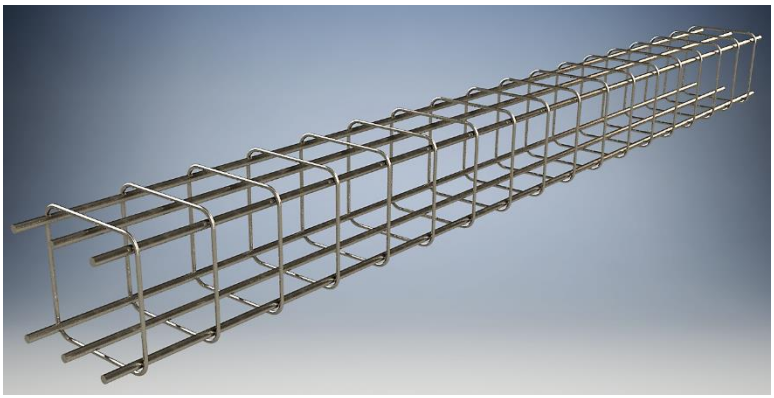

Figure 3-14: Two Types of Reinforcements in the Prestressed Concrete Elements

3.5 Simulation Cases

To examine the capability of the detection technique, different artificial defects are made on the specimens**.** Specimens include seven-wire uncoated strands (ASTM A416 /A416 M) with a nominal diameter of 1/2 inch. Considering the various configuration of steel components in the regular prestressed concrete beams, four general cases are considered for the simulations. The variation of magnetic field because of motion of magnet blocks is measured in the vicinity of section loss and, at the centerline of samples parallel to *x*-axis.

1. Six strands with multiple flaws with different section loss percentages created in one of the strands.

2. Six strands and one stirrup in which several lengths of stirrups are simulated.

3. Six strands and two stirrups in which several spacing values of stirrups are modeled.

4. Six strands, two stirrups, and a flaw in which the multiple configurations of stirrups and flaw are simulated.

Case 1: six strands and a flaw

The first set of simulations contains six strands with a diameter of 0.5 inches and a section loss in four states. Section losses are generated to model overall flaws of 2.36%, 4.77%, 7.14%, and 16.67%, comparing with the whole cross-section area of strands. The lengths of flaws are set to 1/3, 2/3, and 1.0 inches. Figure 3-15 shows the variation of the vertical magnetic field by the effects of several flaws with a length of 1/3 of an inch. The amplitudes of pulses are significantly affected by the percentage of section loss whereas their durations are not dominated by the intensity of flaws. Moreover, the duration of flaws is expected to vary by the length of the flaw. Figure 3-16 demonstrates the effect of the length of the flaw on the amplitudes of pulses from flaws. Also, in this figure, the nearly linear variation of amplitude response due to flaw size is illustrated.

Considering both Figure 3-15 and Figure 3-16, it can be concluded that the amplitude of pulses for flaws would be affected by the volume of the flaw such that higher volumetric change corresponds to a larger pulse.

Figure 3-17 shows the variation of the longitudinal magnetic field by the effects of several flaws with a length of 1/3 of an inch. A different pattern of variation of the longitudinal magnetic field is observed. Generally, the overall amplitude of the field variation for B_z is larger than that for B_y, which, in most cases, it makes B_z a better candidate for flaw detection.

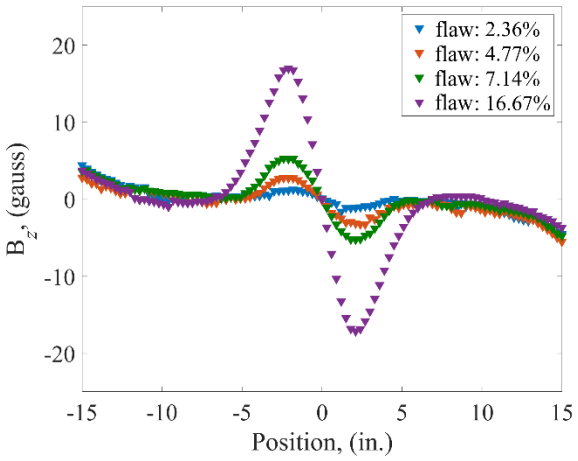

Figure 3-15: Variation of the vertical magnetic field for different flaws with a length of 1/3 of an inch

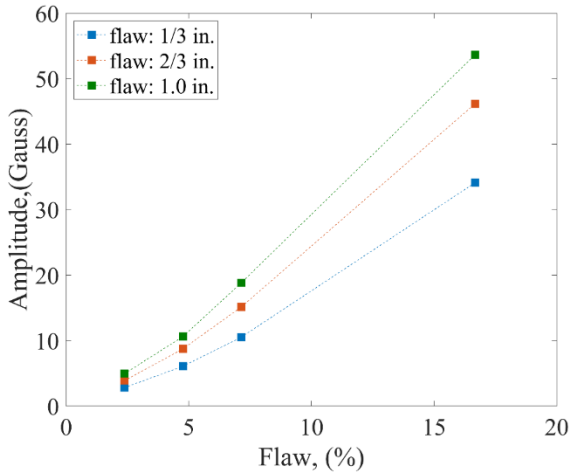

Figure 3-16: Variation of amplitudes for several flaws' percentages and lengths

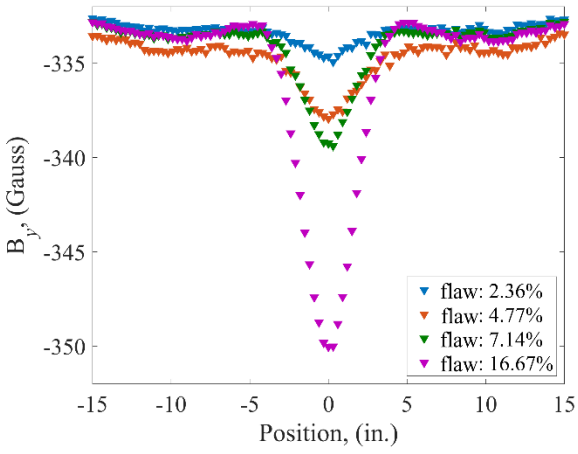

Figure 3-17: Variation of the longitudinal magnetic field for different flaws with a length of 1/3 of an inch

A 3D plot of the magnetic field variation in the corroded region is presented in Figure 3-18 (a) and (b) for B_z and B_y, respectively. The base magnitude of the B_z component of the magnetic field is around zero for all sensors, demonstrating that there is no vertical component for the magnetic field where there is no flaw. On the other hand, the base magnitude for the B_y component would be close to the saturation level of steel used for strands.

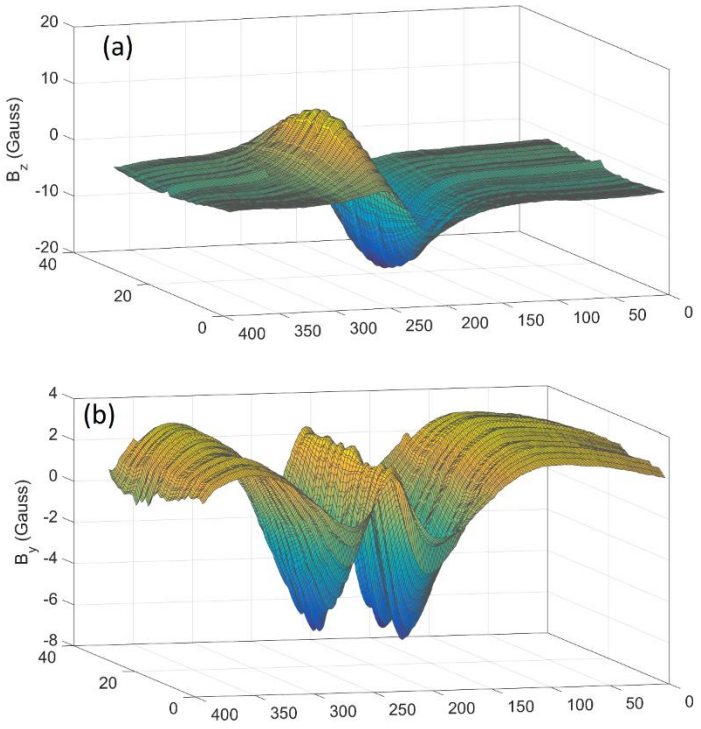

Figure 3-18: 3D Plot of the Magnetic Fields for case 1 a) Bz, b) By

Case 2: six strands and one stirrup

The second case contains six strands (without a section loss) and a stirrup. As illustrated in Figure 3-19, the presence of a stirrup is tantamount to considering a volumetric change of steel, which leads to a flux leakage. But because of the different geometry of the volumetric change, the pattern of variation of the magnetic field is different than a flaw.

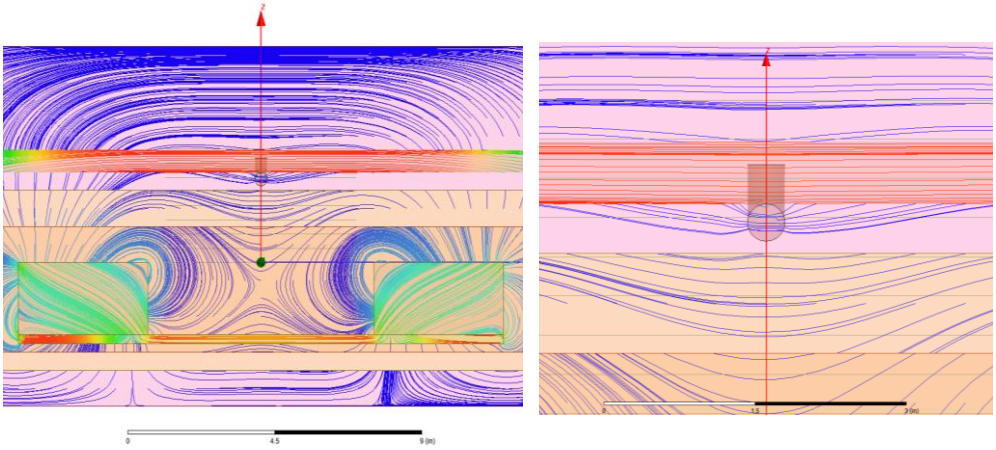

Figure 3-19: Flux Leakage for Case 2

The variations of B_z and B_y are shown for stirrups with different lengths of 8, 10, 12, and 18 inches (Figure 3-20). Despite the 0.5-inch diameter of all the stirrups, the pluses significantly vary by the length of stirrups, which illustrates the dependency of field variation on the volume of stirrups. Moreover, the duration of pulses did not vary by the length of the stirrup that is dependent on the diameter of the stirrup.

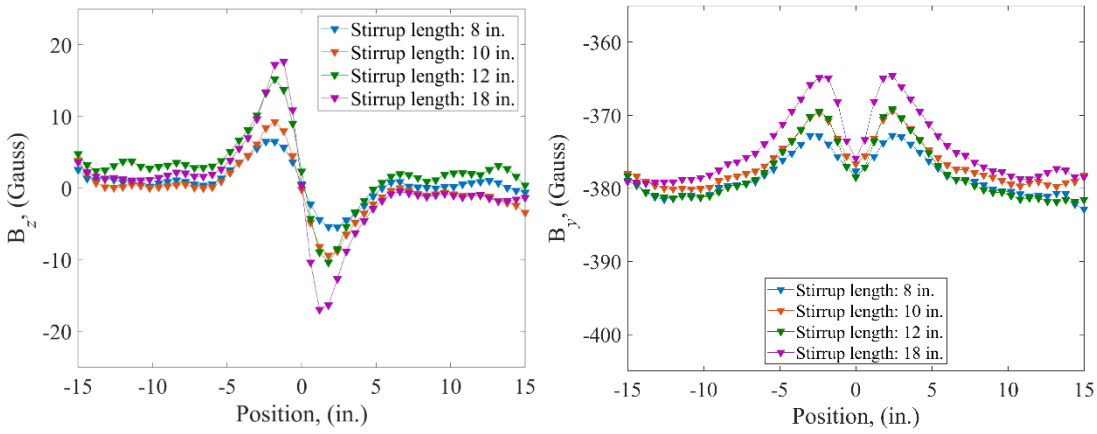

Figure 3-20: Output Signal for Several Stirrup Length (ANSYS Results); a) B_z and b) B_y

Variations of both B_z and B_y are presented in Figure 3-21, illustrating that the vertical component of the magnetic field has shown a higher variation than the longitudinal component.

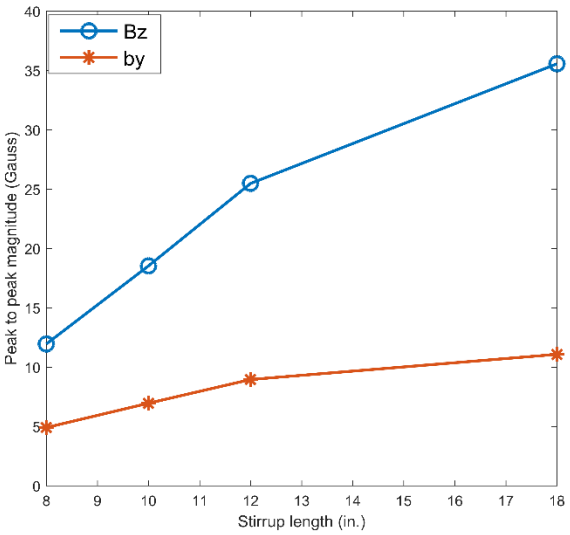

Figure 3-21: Peak to Peak Magnitude for Several Stirrup Lengths of Case 2

Case 3: six strands and two stirrups

In the third case, a sequence of two stirrups is modeled with six strands and the effects of the stirrups are assessed by simulation. Simulation results are shown for 12-inch-long stirrups with different spacing of 8, 12, and 16 inches in Figure 3-22 for both B_z and B_y. As observed, for closer stirrups, the interference of pulses may introduce complexity in the resultant signal.

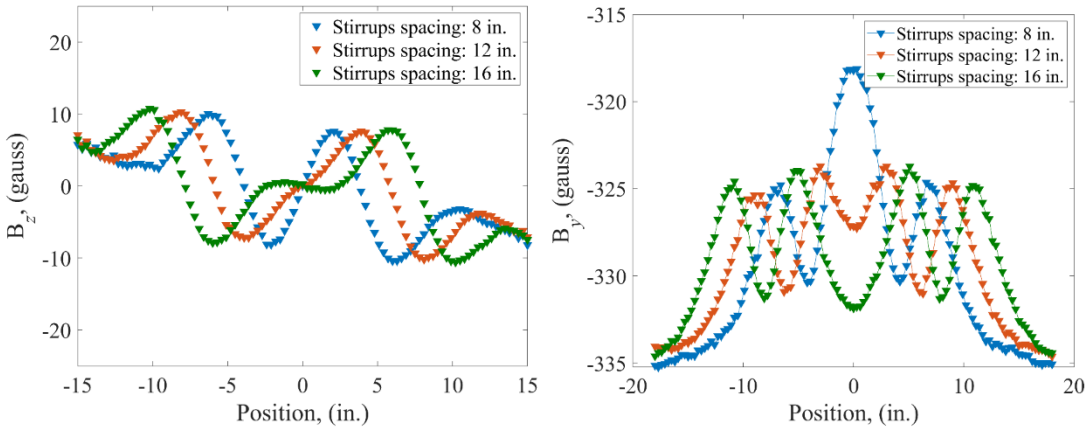

Figure 3-22: Effects of stirrups spacing on the magnetic field

Case 4: six strands, two stirrups, and a flaw

In this case, two stirrups with a specific distance, and a flaw located on one of the strands are modeled. A total of 24 simulations were conducted based on two stirrups' spacing of 12 and 16 inches, three relative distance of flaws from the first stirrup (0, 0.25, and 0.5[2]), and four percentages of section loss (2.36%, 4.77%, 7.14%, and 16.67%). Figure 3-23 shows the configuration of the magnetic field where the flaw is located at the same position as the first stirrup.

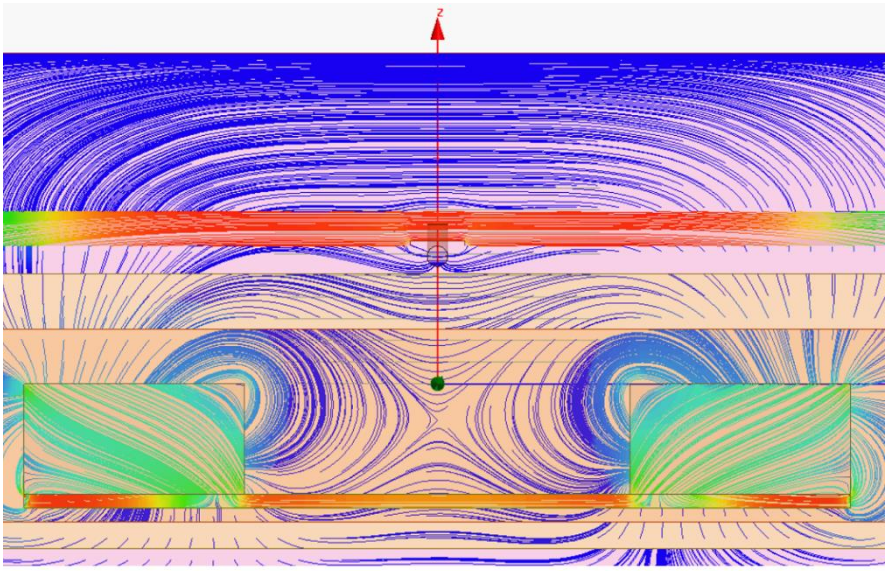

Figure 3-23: Flux Leakage for Case 3

Results from 24 simulations relevant to case 4 are presented in Figure 3-24 to Figure 3-29. Each figure contains plots for percentages of multiple flaws such that the effect of intensity of section loss is illustrated. In addition to the intensity of the flaw, its relative position with respect to the first flaw has shown significance on the resultant signal for each simulation. The next significant factor on the resultant signal is the distance of stirrups, which introduces more complexity into the signal analysis in samples with small distances of stirrups such as 8 inches or

[2] The relative distances are defined based on fractions of stirrups distance. Therefore, the relative distance of 0.25 equals to 4 inches for the stirrup spacing of 16 inches.

lower (referring to Figure 3-22). The closer stirrups may cause interference of effects of sequential stirrups that interrupts the common pattern of field variations. In such cases, evaluating the B_y variations of the magnetic flux leakage could help the data interpretation.

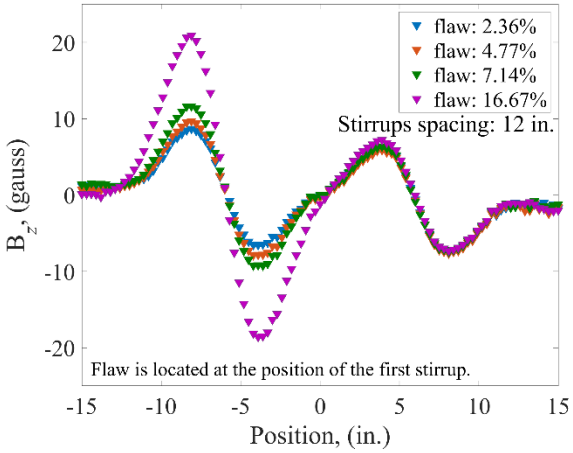

Figure 3-24: Vertical field variation where the flaw is located at the position of the first stirrup

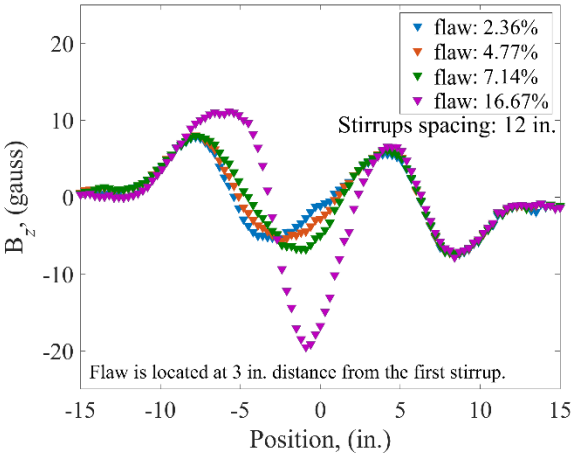

Figure 3-25: Vertical field variation where the flaw is located at the relative distance of 0.25 from the first stirrup

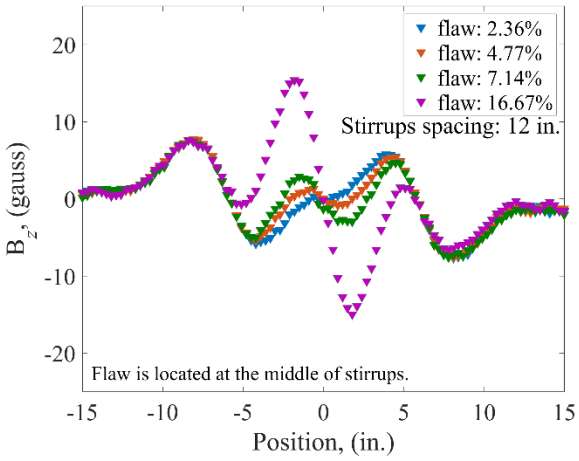

Figure 3-26: Vertical field variation where the flaw is located at the relative distance of 0.50 from the first stirrup

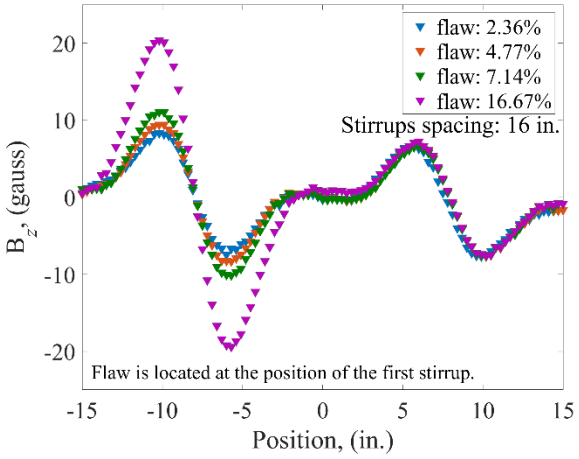

Figure 3-27: Vertical field variation where the flaw is located at the position of the first stirrup

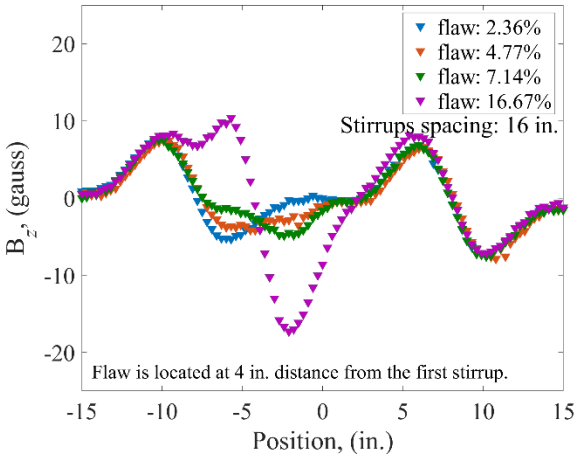

Figure 3-28: Vertical field variation where the flaw is located at the relative distance of 0.25 from the first stirrup

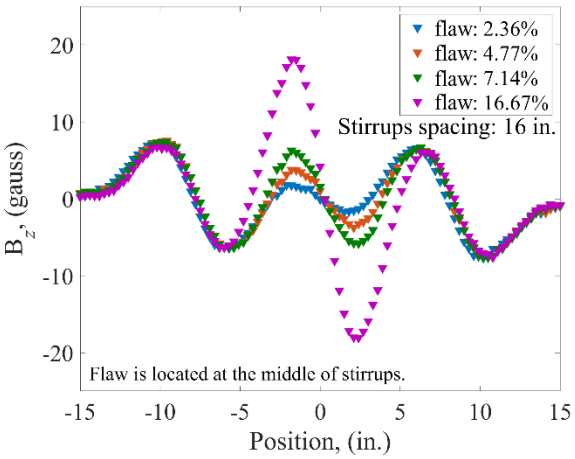

Figure 3-29: Vertical field variation where the flaw is located at the relative distance of 0.50 from the first stirrup

Chapter 4 **Experimental Results**

4.1 **MFL apparatus**

The test instrument used in this study includes two permanent magnet blocks, a thin steel shunting plate, an electronics package with sensors, circuits, and a data acquisition system that were assembled on a mechanical frame. Magnetic flux data was recorded with 120 data points per one inch of system's travel. A precision encoder was used to achieve this. Via wireless communication, the acquired data was transferred to a desktop computer for recording, analysis, and display. The test setup included various configurations where strands with/without man-made flaws were placed near the surface of each magnet. The clear distance between the lowest level strands and the magnets' surfaces was 2.0 inches. Two permanent magnets, with a thickness of 1.8 inch and with dimensions of 8.25 by 4.25 inch, are used as a field generator to magnetize the ferrous materials, see Figure 4-1a, b, c & d. The Neodymium Iron Boron Magnet grade 42 (NdFeB42) is used to have a strong enough magnetic field to create near saturation for a common number of steel strands in the first row of a typical prestressed concrete bridge girder. The magnet's relative permeability is μ_r=1.099778 and the *z*-component of the magnetic coercive force is H_c=-89000 A/m, whereas the *x* and *y* components of the coercive force are zero. The unit vector of the coercive force for the right-side magnet is $\overrightarrow{H_{c,R}}$= (0,0,1) and for the left side magnet is $\overrightarrow{H_{c,R}}$= (0,0, -1). Magnets are attached to a steel plate with the size of 15×8.25×0.25 inches including two arch cuts with the size of 6.5×1.625 inches to prevent magnetic flux dispersion and to concentrate the field around the strands. In real cases, the apparatus is moved along the surface of the lower flange of a prestressed concrete girder with a constant low velocity to detect defects by measuring the components of the magnetic field with Hall-effect sensors. In the laboratory test setting, the system

is moved at a distance of 2 inches over the prestressing strands to simulate the real conditions. This work was completed by using 32 sensors to detect the vertical component of the magnetic flux leakage although the system is equipped with an additional 32 sensors that can detect the horizontal component. The arrangement of 32 Hall-effect sensors across the width of MFL system (*x*-axis) is shown in Figure 4-1(f). Since a Hall-effect sensor measures the field normal to its plane, these sensors measure only the vertical component of magnetic field (B_z). Additionally, another set of 32 sensors were placed along *x*-axis with the face toward *y*-axis to measure the horizontal component (B_y).

The 3D plot in the Figure 4-1(g) shows the response of each sensor for the vertical component (B_z) given from all 32 channels for a test case with only a #4 stirrup. As shown in the Figure, the signal amplitudes from all sensors are nearly identical with small amplitude reductions for sensors located closer to the stirrup's ends. The blue dots in the inset plot of Figure 4-1(g) represent the amplitude of signals shown in 3D plot

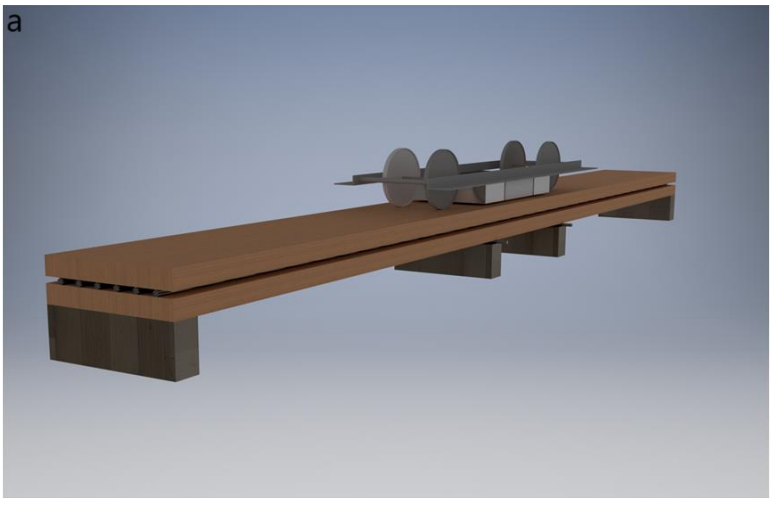

b

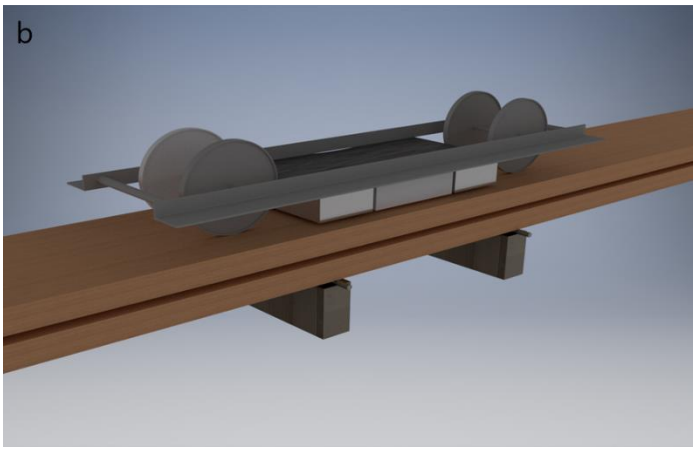

c

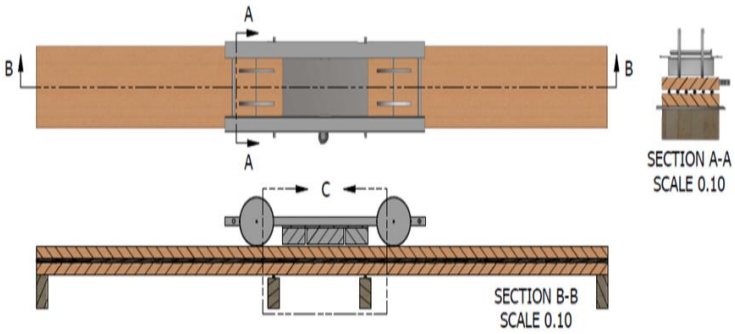
A
B
B
A
SECTION A-A
SCALE 0.10
C
SECTION B-B
SCALE 0.10

d

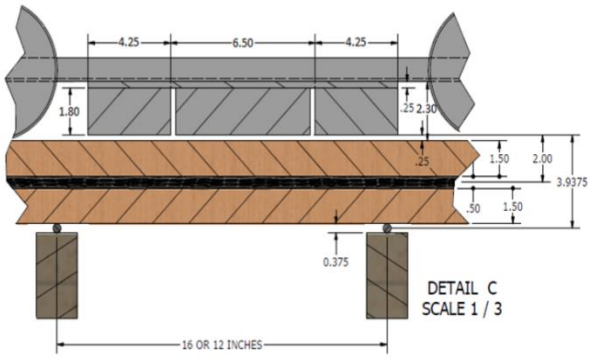
4.25
6.50
4.25
1.80
.25
2.30
.25
1.50
2.00
3.9375
.50
1.50
0.375
DETAIL C
SCALE 1 / 3
16 OR 12 INCHES

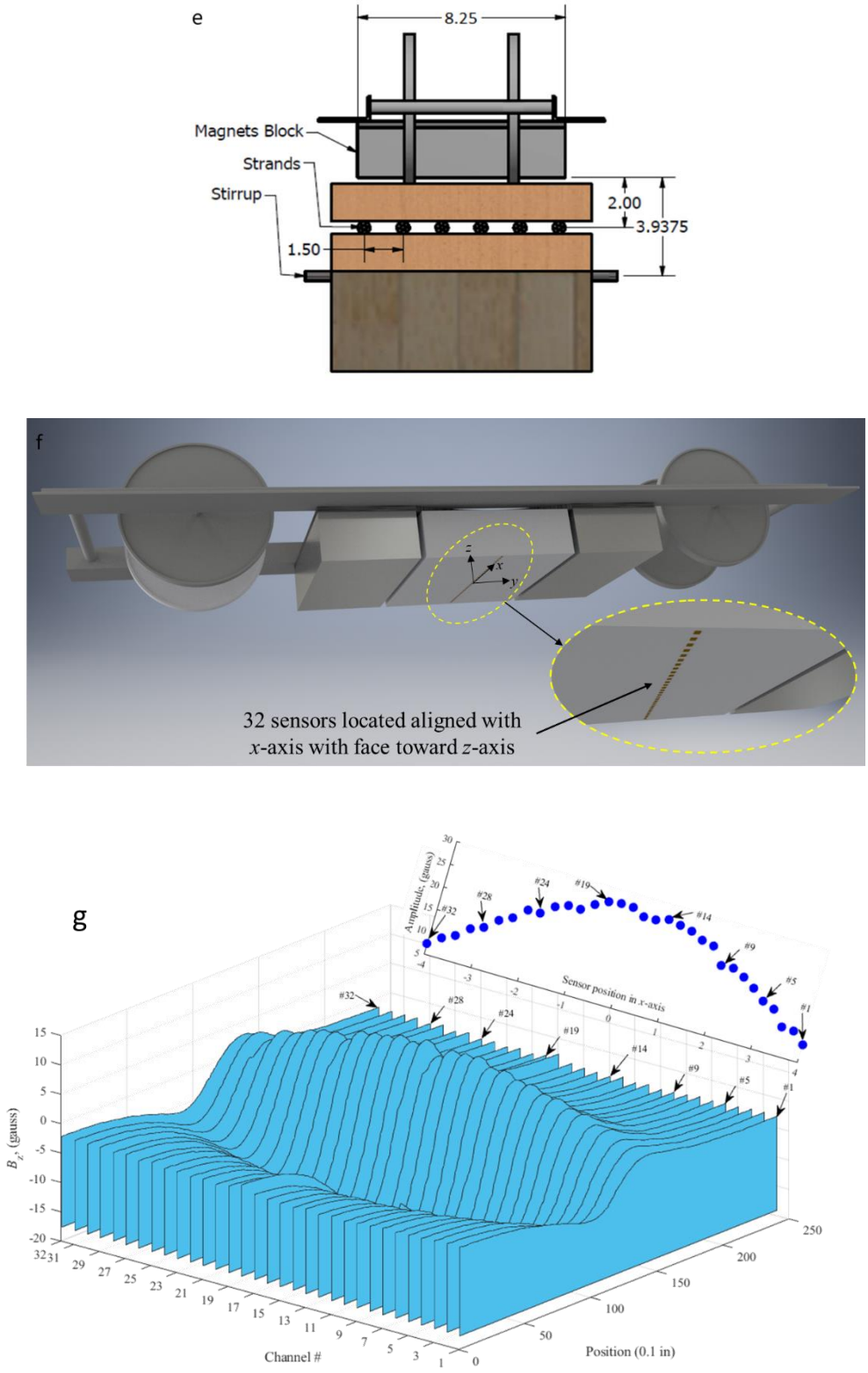

Figure 4-1: (a) 3D view of the test setup, (b) close 3D view of MFL instrument, (c) up and side view of the test setup, (d) detail view to show the dimensions of the test setup and distances between system components, (e) front view of the test setup and, (f) representation of hall-effect sensors arrangement, (g) presentation of the vertical component of magnetic field in 3D plot for 32 sensors and magnitude of pulses amplitude detected by each sensor

4.2 Experimentation

In real cases for bridge structures, several sources are causing magnetic flux leakage, as follows:

- Stirrups: effective factors are the stirrups' diameter, orientation angle, and spacing.
- Strands: the number and diameter of strands are of importance on the intensity of flux leakage.
- Flaws: can appear as an abrupt pitting, gradual section loss such as corrosion, or cuts in strands. Therefore, the length and intensity of the flaw are significant parameters on the MFL.

To consider these parameters in experimentation, four categories were defined that are explained later in this chapter.

- ***Category 1: six strands and a flaw***

As shown in Figure 4-2, in this study, the flaw is located on the third strand through man-made cuts of wires. For this project, cases with one, two, three, and seven cuts of wires have been used, which correspond to section losses of 2.38%, 4.77%, 7.14%, and 16.67% of the gross cross section (seven wires for six strands), respectively. The length of the flaw is another parameter with a noticeable effect on the signal duration, which was considered a third of an inch for experimentation.

Figure 4-2: Schematic View of Category 1

- ***Category 2: six strands and stirrups***

In this category, Figure 4-3, the cases with one or two stirrups are tested to assess the effects of the stirrups. The #4 bars were used as stirrups with center-to-center distances of 12 and 16 inches. To consider the unintended deviation angle of stirrups in construction, stirrups were aligned by angles of 90 and 80 degrees.

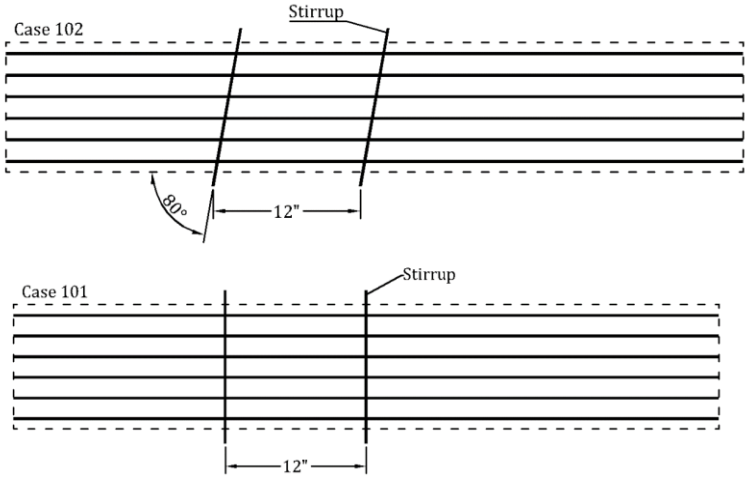

Figure 4-3: Schematic View of Category 2

- ***Category 3: six strands, one stirrup, and one flaw***

In this category, (Figure 4-4) the effect of flaws was assessed on the stirrup signal for several distances of the flaw from the stirrup. The stirrup orientation angle is also another parameter in this category.

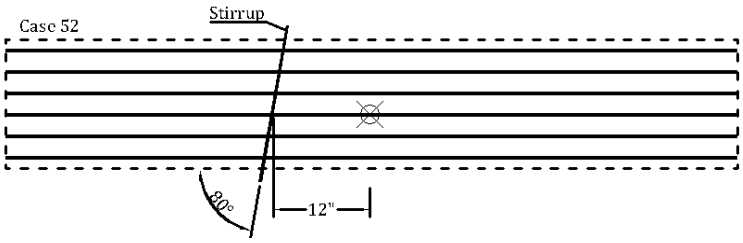

Figure 4-4: Schematic View of Category 3

- ***Category 4: six strands, two stirrups, and a flaw***

This category is divided into two sub-categories with different locations of the flaw. The first case contains a flaw between two stirrups while the second case has a flaw outside of two stirrups.

- ***flaw is located between two stirrups***

In these cases (Figure 4-5), the flaw is located between two stirrups and its effect has been assessed for three relative distances of 0, 0.25, and 0.50 from the first stirrup. The relative distances are the fractions of the stirrups' distance. Moreover, the orientation angle of the stirrups is another parameter in this category. Considering several configurations of stirrups and the flaw, this category simulates situations with the most similarity to real cases.

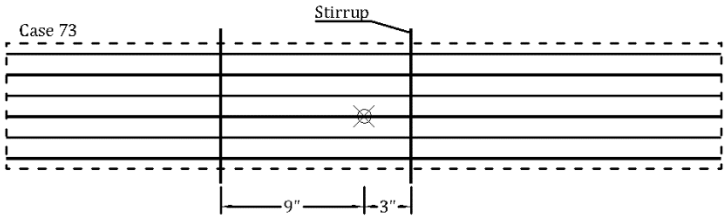

Figure 4-5: Schematic View of Category 4-a

- ***flaw is located out of two stirrups***

In these cases (Figure 4-6), the flaw is located between two stirrups and its effect has been assessed for four relative distances of 0, 0.25, 0.50, and 1.0 from the second stirrup. Moreover, the orientation angle of the stirrups is another parameter in this category.

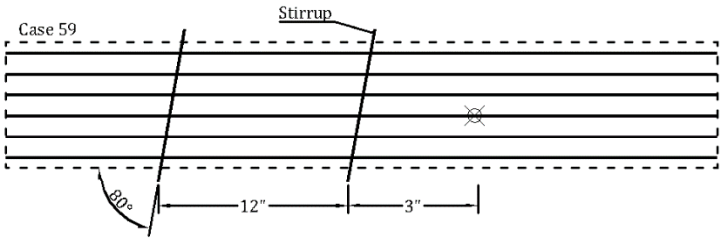

Figure 4-6: Schematic View of Category 4-b

4.3 Category 1: Six strands and a flaw

In category 1, the test specimens were made having six strands and a flaw, which is located on the third strand. As mentioned earlier and shown in Figure 4-7, section losses of 2.36%, 4.77%, 7.14%, and 16.67% were created through a third of an inch long cut on wires of the third strands. The amounts of section loss were calculated based on the whole cross-sectional area of six strands.

The amplitudes and durations of MFL signals for specimens with the above-mentioned section losses are presented in Figure 4-8 and

Table 4-1. The linearity of amplitude variation for different flaw sizes is presented in Figure 4-8, which is confirmed by both experimental and simulation results. The results also show that the signal duration remains nearly unchanged for flaw sizes commonly encountered in real cases. A good agreement is observed between the experimental and simulation results, confirming the 3D transient simulations results for several flaws.

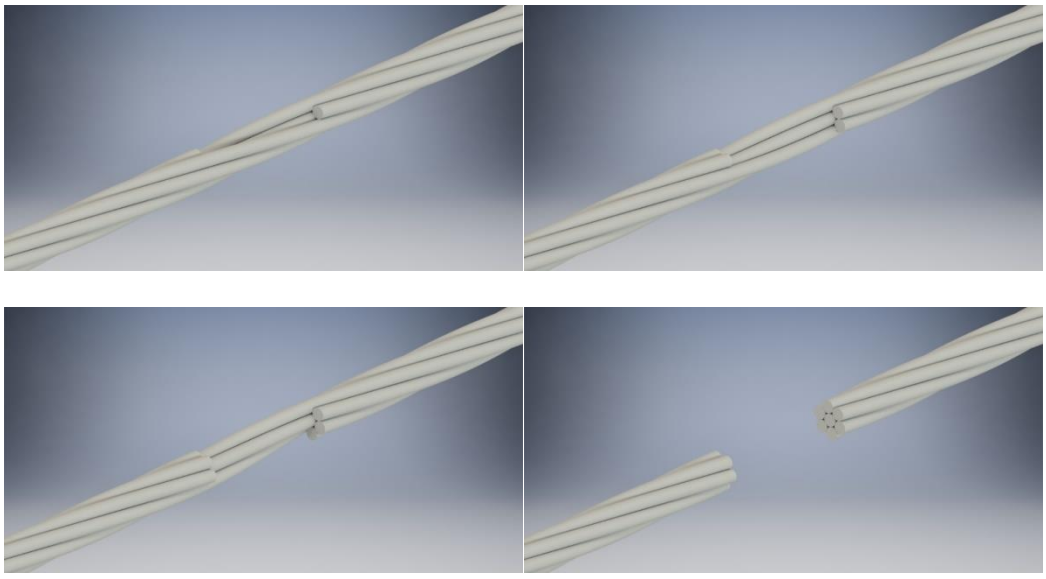

Figure 4-7: section losses for a seven-wire strand: one wire (2.38%), two wires (4.77%), three wires (7.14%), and seven wires (16.67%)

Table 4-1: Effect of flaw percentage on peak-to-peak values of MFL signals

Flaw (%)	Flaw length (in.)	Amplitude (Gauss)		Duration (in.)
		Experiment	Simulation	
2.38	1/3	4.96	2.83	2.4
4.77	1/3	6.89	6.09	2.7
7.14	1/3	10.44	10.53	2.6
16.67	1/3	29.61	34.11	2.6

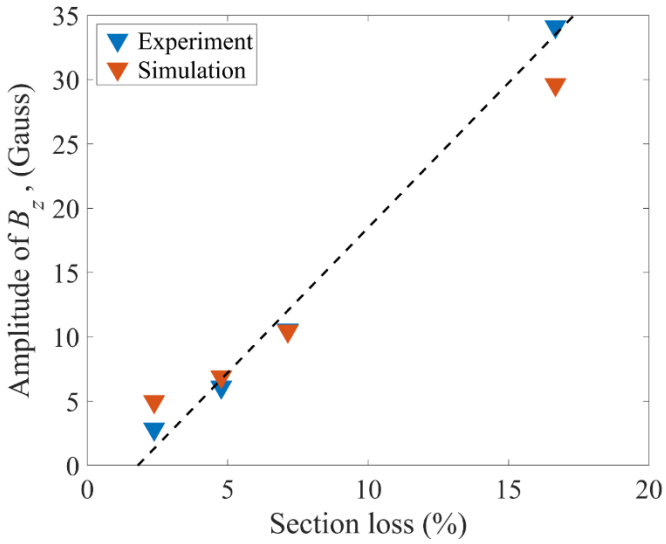

Figure 4-8: Variation of Amplitude Values Versus Flaw Percentage

In a separate experiment, strands with several lengths of the flaw were tested to evaluate the effect of the length of the flaw on MFL signal characteristics. These specimens have a strand with a complete fracture equivalent to 100% of section loss of a strand, which equals 16.67% of overall section loss). The results of this experiment are shown in Table 4-2 and Figure 4-10, in which graphs of the measured amplitude and durations are displayed. The variations of the length of the flaw have dominant effects on both the amplitude and duration of the MFL signals. For the flaws shorter than 7 inches, which is the clear distance of two magnet blocks, the amounts of amplitude and duration vary accordingly.

When the length of the flaw is longer than the clear distance between the two magnets, the MFL signal shows a separation of the two peaks observed in a typical signal for a short flaw, as

shown in Figure 4-9. At the start-point of the flaw, the MFL signal shows only one peak so that the second peak emerges at the endpoint of the flaw. It does mean that two peaks of the MFL signal are associated with two ends of the flaw and the distance between the two peaks indicates the flaw length.

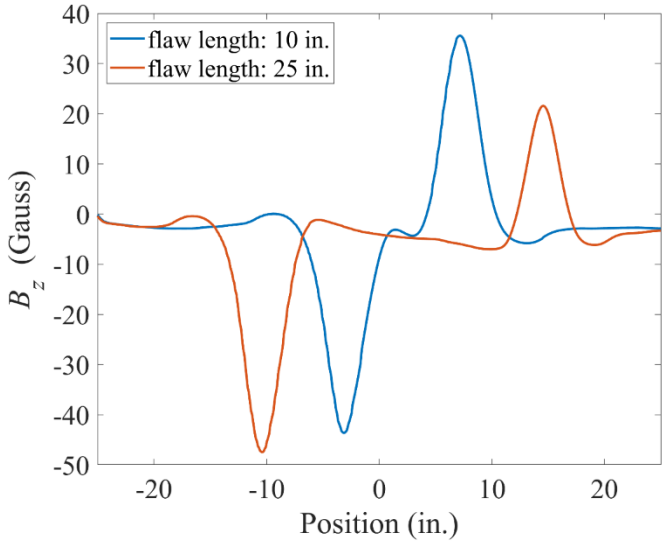

Figure 4-9: signal separation for long flaws

For flaws longer than about 7 inches, the amplitudes of MFL signals have not shown a significant variation. On the other hand, the duration of signals has shown a meaningful variation such that it presents the length of flaw with an acceptable accuracy, as depicted in Table 4-2.

Table 4-2: Effect of Flaw Length on the Signal Peak-to-Peak Magnitude

Flaw (%)	Flaw length (in.)	Amplitude (Gauss)	Duration (in
16.67	0	6.62	2.3
16.67	0.33	29.61	2.6
16.67	0.66	42.49	2.8
16.67	1	52.65	3
16.67	2	72.48	3.6
16.67	5	94.04	5.8
16.67	10	88	10.3
16.67	15	84.79	15.2
16.67	25	74.85	24.9

16.67	50	90.24	49.5

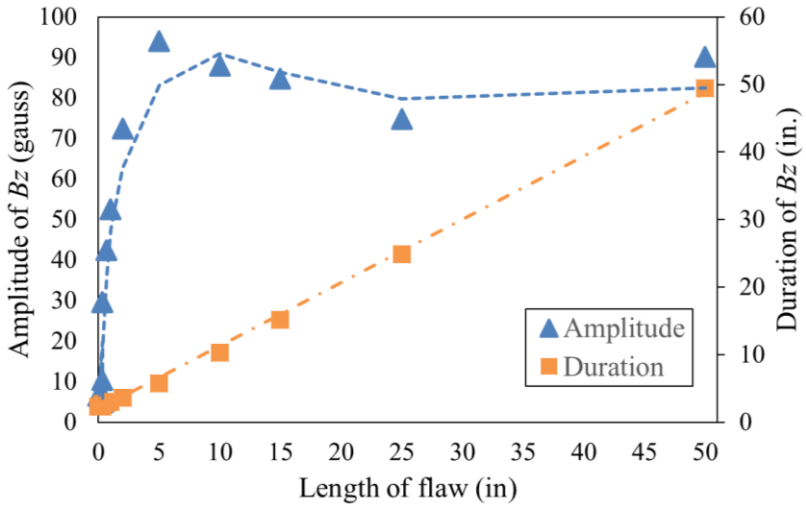

Figure 4-10: Amplitudes and duration versus the Length for a flaw of 16.67%

The Effect of the volume of the flaw on the MFL signal

As mentioned above, the section loss percentage and the length of the flaw are two significant factors on the amplitude and duration of signals. The volume of the flaw, which is defined as the product of section loss area and its length, seems to be useful in the assessment of MFL signals of flaws. Figure 4-11 shows a plot of the variation of amplitude by changing the volume of the flaw. Three parts are highlighted in Figure 4-11. In the first part, the length of the flaw is constant (and equals 1/3 inch) while the percentage of flaw changes from 2.38% to 16.67%. A linear variation of amplitude is seen for this part, as presented earlier in Figure 4-8. The second part is related to a constant section loss of 16.67% and variable lengths of flaw from 1/3 inch to five inches. A roughly linear relationship between the volume of flaw and amplitude was observed, demonstrating that the volume of the flaw can be considered as a significant factor on the MFL signal.

The last part of the diagram refers to cases with a constant percentage of flaw (16.67%) and variable length from 5inches to 50 inches. Considering the occurrence of a signal separation for the flaws longer than 7 inches, the variation of amplitude has not shown a significant variation. Therefore, for the flaw longer than the clear distance of magnets, the only significant factor on the MFL signal is the length of the flaw.

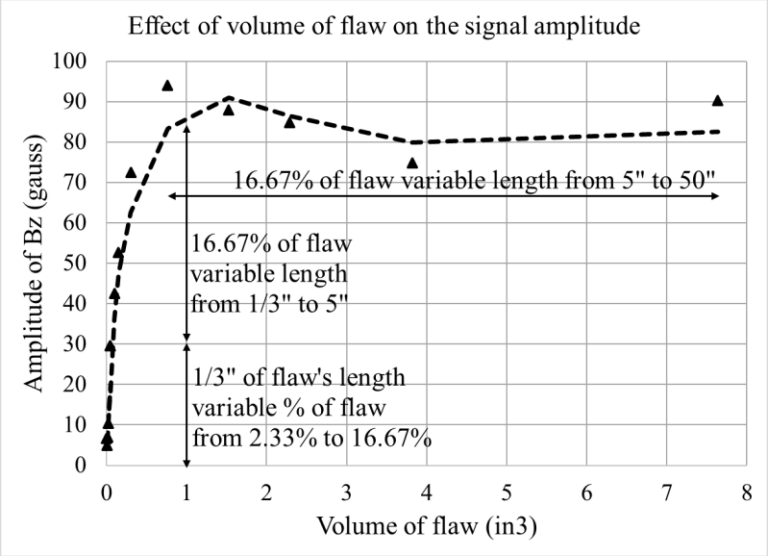

Figure 4-11: Variation of Signal Amplitude of Flaw by the Effect of Volume of Flaw

4.4 Category 2: six strands and stirrups

In this category, the cases with one or two stirrups have been tested to assess the effects of stirrups individually. Bar #4 has been used as a stirrup and the center-to-center distances of 12 and 16 inches were considered. To consider the deviation angle of the stirrups, the angles of 90 and 80 degrees were used, displayed in

Table 4-3.

These tests were done for configurations with/without strands, one or two stirrups, and 90 and 80 degrees as an orientation angle. As was expected, the amplitude of pulse for two stirrups is smaller than for one stirrup, which demonstrates the superposition of pulses. On the other hand,

the distance between stirrups has noticeable effects on the amplitude, which would be negligible for the lengths bigger than 16 inches, as shown in Figure 4-12. The orientation angle slightly shifts the position of peaks of MFL signals, which leads to a minor change in duration values.

The contour plots shown in Figure 4-13 illustrate the effect of the orientation angle on the MFL signals. These plots were drawn based on signals from all channels of the MFL apparatus and represent a 3D visualization of signals, which helps to identify the orientation angle of the stirrups.

Table 4-3: Results of Stirrups' Test

# of Stirrups	spacing	angle	Strands?	Amplitude (Gauss)		duration (in.)	
				stirrup #1	stirrup #2	stirrup #1	stirrup #2
1	-	90	NO	22.85	-	3.4	-
1	-	90	YES	26.11	-	4.4	-
1	-	80	NO	21.80	-	3.8	-
2	12	90	YES	17.99	16.99	4.7	4.7
2	12	80	YES	17.17	16.34	4.6	4.6
2	16	90	YES	18.41	17.39	4.8	4.5
2	16	80	YES	17.44	16.60	4.9	4.9

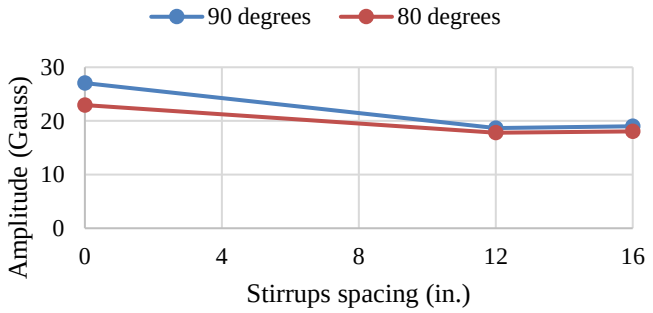

Figure 4-12: Effects of Stirrups Spacing and Alignment Angle on the Amplitude

Figure 4-14 shows the effect of the stirrup distance on the amplitude of the signal given from two stirrups. The maximum value for the amplitude of the signal happens at zero, which means two stirrups are at the same position. The minimum amplitude occurred at the space of

about six inches by the magnitude of 0.7 times the initial amplitude. Based on Figure 4-14, the amplitude of pulse for a distance of more than 15 inches is almost unchanged.

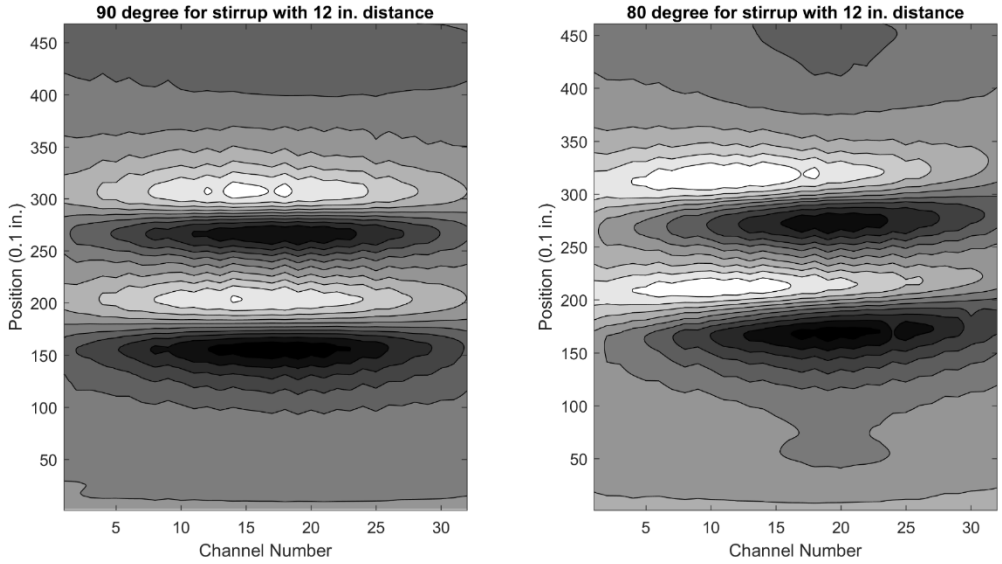

Figure 4-13: Effect of Orientation Angle of Vertical Component of Magnetic Field

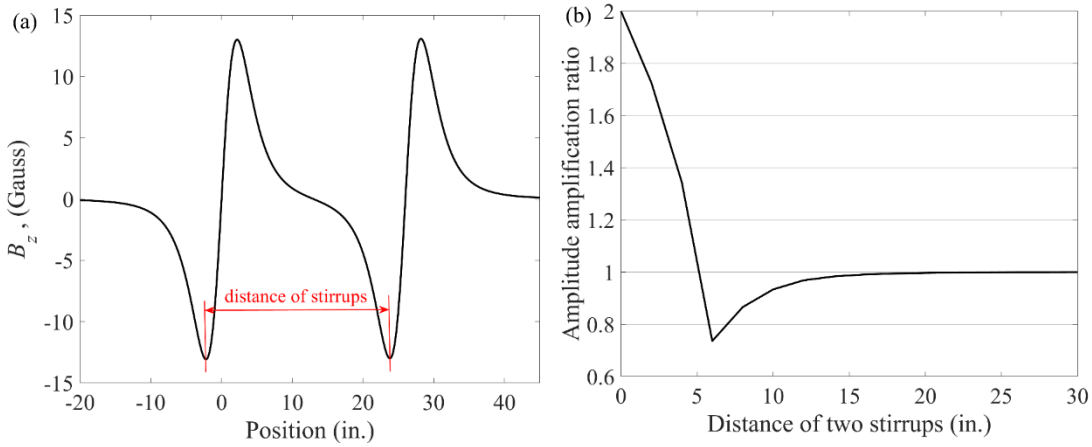

Figure 4-14: Stirrup Spacing Effect on Pulse Amplitude

4.5 Category 3: six strands, one stirrup, and one flaw

In this category, the effect of a flaw on the amplitude of the stirrup signal was considered for the several distances of the flaw from the stirrup. The stirrup orientation angle is also another factor in this category, Table 4-4. Figure 4-15 shows the effect of a flaw (of 2.38%) on the

amplitude of the stirrup's signal where the maximum amplitude occurs at eight inches distance from the stirrup and the minimum amplitude occurs at four inches.

Table 4-4: Effect of the Flaw Distance from the Stirrup on the Amplitude

Flaw (%)	Distance of flaw from stirrup	Angle of stirrups	Amplitude (Gauss)
2.38	3	90	17.42
2.38	4	90	16.93
2.38	6	90	18.44
2.38	8	90	19.59
2.38	12	90	18.98
2.38	16	90	18.53
2.38	3	80	16.22
2.38	4	80	16.07
2.38	6	80	17.55
2.38	8	80	18.73
2.38	12	80	18.04
2.38	16	80	17.58

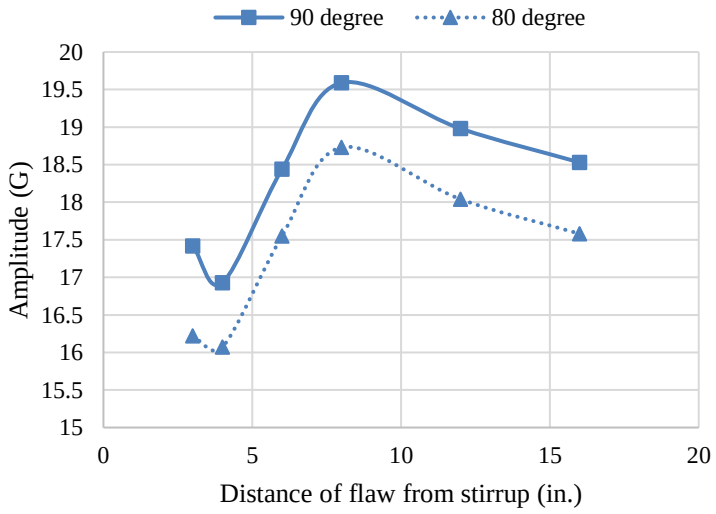

Figure 4-15: Effect of Flaw on the Stirrup Pulse

4.6 Category 4: six strands, two stirrups, and one flaw

Experiments in this category, which is close to convenient real-world structures, were conducted considering the following parameters:

I. Flaw percentage: 2.38%, 4.77%, 7.14%, and 16.67%

II. The relative distance of flaw from the first stirrup is tested by 0, 0.25, and 0.5 where the flaw is located between two stirrups. The relative distance is a fraction of the center-to-center distance of two stirrups which is considered from the first stirrup.

III. When the flaw is not placed between two stirrups: the relative distances of 0.25, 0.5, and 1 are fractions of the center-to-center distance of two stirrups, which is calculated from the right-hand side stirrup.

IV. Stirrup spacing: 12 and 16 inches

V. The angle of stirrups: 90 and 80 degrees

Considering the factors aforementioned, the amplitudes of the first and second stirrup have been measured to identify the effects of the above parameters accurately. For the first state, the flaw is located between two stirrups, as listed in Table 4-5.

Table 4-5: Category 4; Flaw between Stirrups

Flaw (%)	Stirrups spacing (in.)	Relative Distance of flaw from stirrup	Angle of stirrups	1st Amplitude (Gauss)	2nd Amplitude (Gauss)
2.38	12	0	90	19.8	17.69
2.38	12	0	80	18.43	16.25
2.38	12	0.25	90	15.51	17.88
2.38	12	0.25	80	16.06	17.09
2.38	12	0.5	90	16.6	17.4
2.38	12	0.5	80	15.46	16.38
2.38	16	0	90	20.73	16.59
2.38	16	0	80	19.09	16.25
2.38	16	0.25	90	16.34	18.12
2.38	16	0.25	80	15.38	16.79
2.38	16	0.5	90	18.01	18.76
2.38	16	0.5	80	16.81	17.2
4.77	12	0	90	23.71	16.7

Flaw (%)	Stirrups spacing (in.)	Relative Distance of flaw from stirrup	Angle of stirrups	1st Amplitude (Gauss)	2nd Amplitude (Gauss)
4.77	12	0	80	22.74	15.77
4.77	12	0.25	90	19.13	17.84
4.77	12	0.25	80	-*	-*
4.77	12	0.5	90	17.77	17.77
4.77	12	0.5	80	16.24	17.01
4.77	16	0	90	19.25	16.75
4.77	16	0	80	18.36	-
4.77	16	0.25	90	18.21	16.76
4.77	16	0.25	80	-*	-*
4.77	16	0.5	90	18.62	16.6
4.77	16	0.5	80	18.05	17.19
7.14	12	0	90	26.86	18.22
7.14	12	0	80	23.47	15.96
7.14	12	0.25	90	20.37	18.98
7.14	12	0.25	80	19.61	17.49
7.14	12	0.5	90	15.53	16.73
7.14	12	0.5	80	13.63	15.66
7.14	16	0	90	25.85	17.16
7.14	16	0	80	22.01	17
7.14	16	0.25	90	19.58	18.28
7.14	16	0.25	80	19.01	17.05
7.14	16	0.5	90	17.91	18.96
7.14	16	0.5	80	16.12	17.58
16.67	12	0	90	45.22	18.05
16.67	12	0	80	46.88	17.55
16.67	12	0.25	90	31.04	19.92
16.67	12	0.25	80	30.19	19.32
16.67	12	0.5	90	12.11	14.48
16.67	12	0.5	80	11.41	14.97
16.67	16	0	90	45.83	17.64
16.67	16	0	80	43.02	17.02
16.67	16	0.25	90	27.97	18.65
16.67	16	0.25	80	28.41	17.85
16.67	16	0.5	90	17.58	19.78
16.67	16	0.5	80	16.2	18.87

Figure 4-16 shows the plots of variations of amplitudes for both stirrups that are drawn based on the variable relative distance of flaw, the distance of stirrups, and the orientation angle of the stirrups. The effect of the flaw percentage and its relative position on the first and second pulse amplitude on MFL signals is illustrated in Figure 4-16. Since the relative distance of the flaw was defined from the first, the variation of amplitude of the first stirrup is more important than that of the second stirrup. As was expected, for the first stirrup a larger variation of amplitudes is observed such that the two factors of the flaw's intensity and its relative distance are more significant than the distance between the stirrups and their orientation angles.

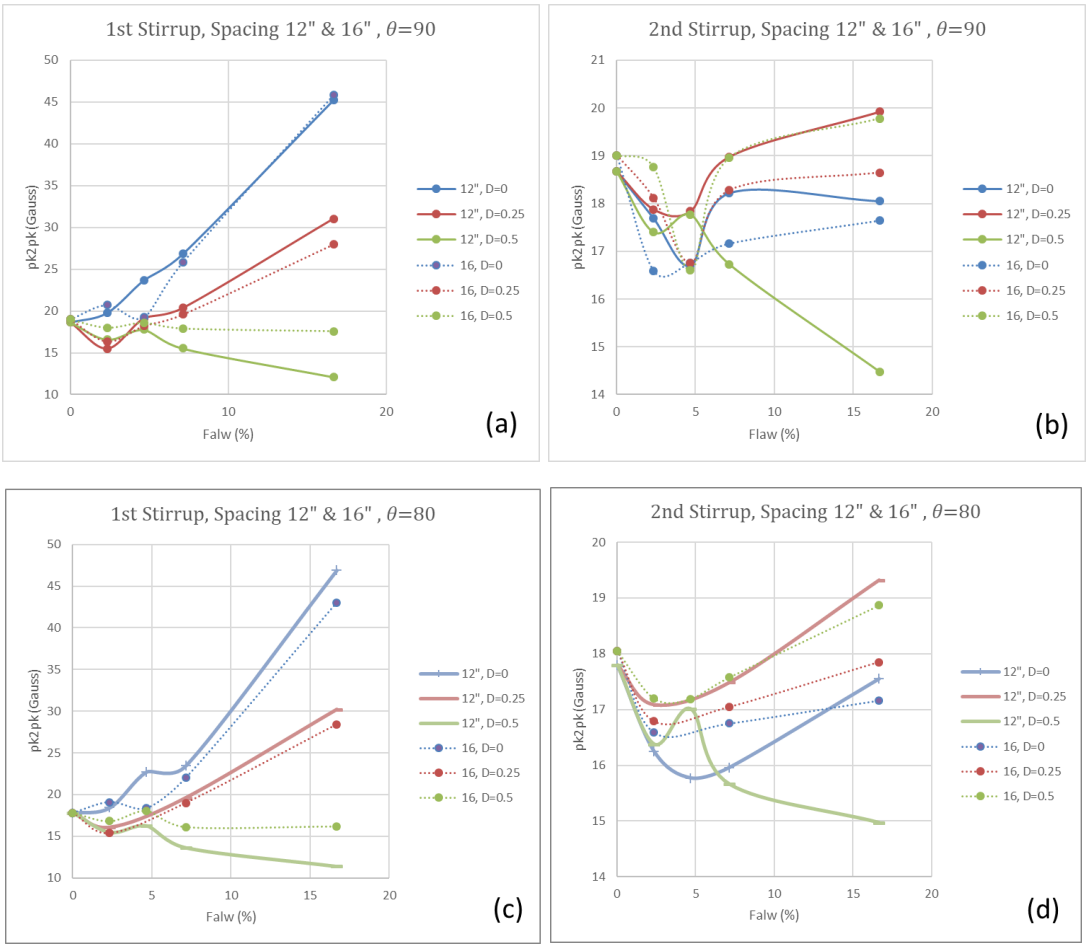

Figure 4-16 a, b, c, & d: Effect of Flaw Percentage and its Relative Position on the First and Second Pulse Amplitude

Another representation of the results of Table 4-5 is shown in Figure 4-17 and Figure 4-18. In these figures, the results are drawn based on the relative position of the flaw, which replicates the variations of amplitudes of stirrups while a flaw is moved from the first stirrup to the mid-point between the two stirrups.

As shown in Figure 4-17-a, b, c, and d for the stirrups' distance of 12 inches, except for 2.38% of the flaw, a decreasing trend of the first stirrup's amplitude exists but the second stirrup's amplitude does not change very much. For the flaw of 2.38%, the minimum value occurs at the relative distance of 0.25. According to Figure 4-18-a, b, c, and d, for the stirrups' distance of 16 inches and the flaws of 7.14% and 16.67%, higher amplitudes of the first stirrup have been observed for smaller relative distances while the second stirrup's amplitude does not change noticeably. For flaws of 2.38% and 4.77%, the variation of the first stirrup's amplitude is not remarkably high and there is a minimum value at the relative distance of 0.25. These plots were provided just for three relative distances, which does not seem enough to have strong results. However, in the next chapter, using the superposition of flaw and stirrups signals, an accurate set of graphs is provided using an analytical method.

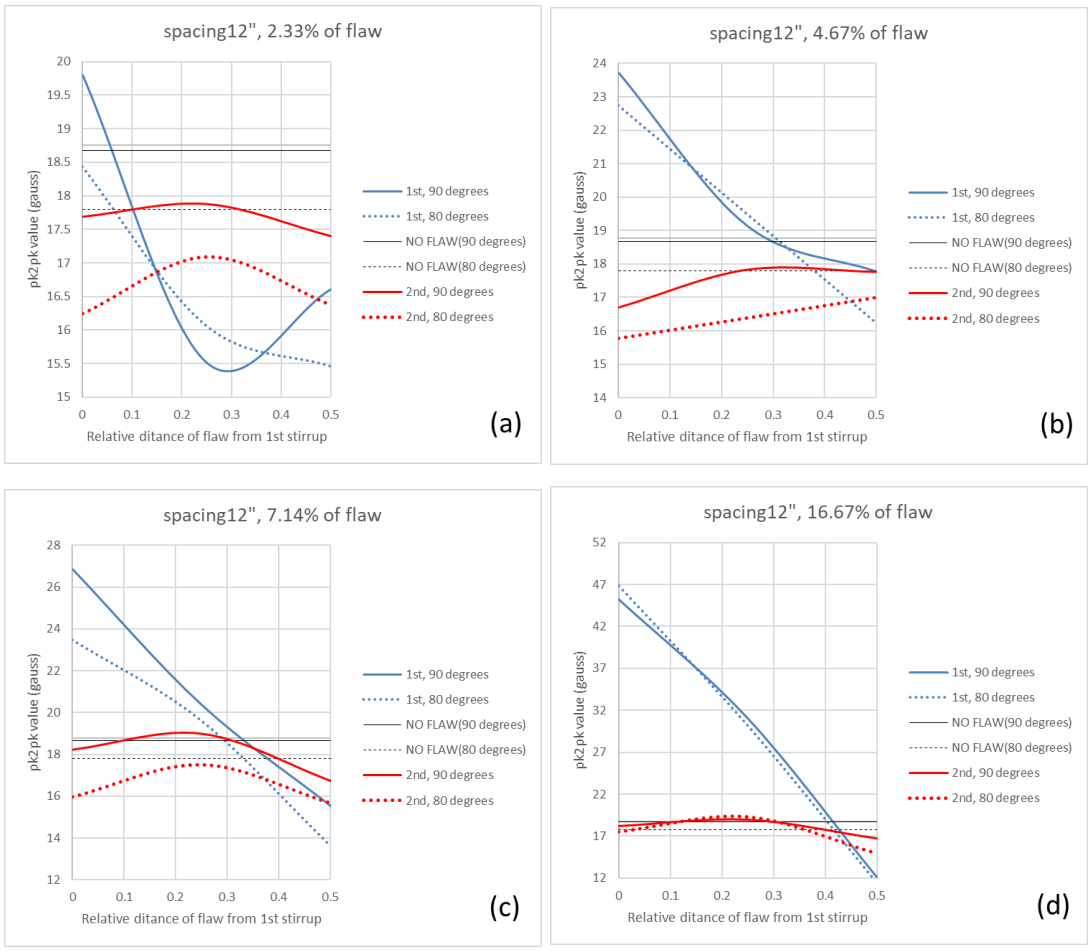

Figure 4-17 a, b, c, & d: Effect of Flaw Relative Position on the First and Second Pulse Amplitude by the Spacing of 12”

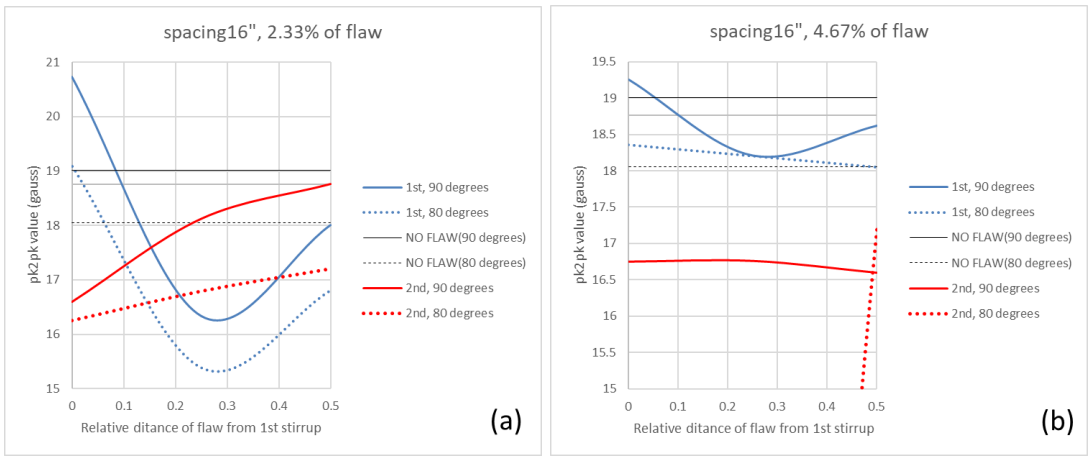

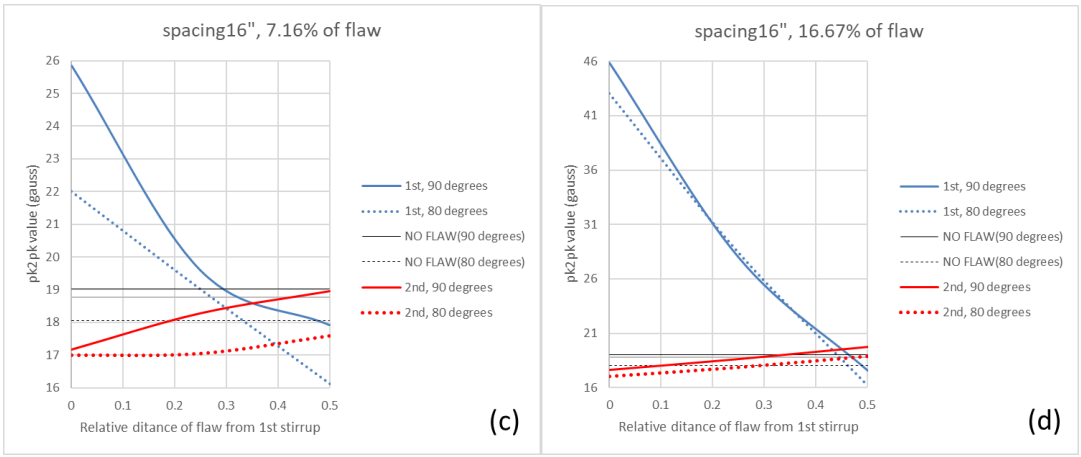

Figure 4-18 a, b, c, & d: Effect of the relative position of the flaw on the first and second pulse amplitude with stirrups' spacing of 16"

Table 4-6: Effects of flaws located outside of two stirrups on the stirrup's amplitudes

flaw (%)	Stirrups spacing (in.)	Angle of stirrups	Distance of flaw from stirrup (in.)	1st Amplitude (Gauss)	2nd Amplitude (Gauss)
4.77	12	90	3	16.95	17.11
4.77	12	90	6	16.76	16.09
4.77	12	90	12	17.91	17.47
4.77	12	80	3	15.82	16.27
4.77	12	80	6	16.08	15.43
4.77	12	80	12	17.07	16.92
4.77	16	90	4	14.72	17.13
4.77	16	90	8	19.16	17.94
4.77	16	90	16	17.78	17.17
4.77	16	80	4	14.63	16.47
4.77	16	80	8	18.33	17.03
4.77	16	80	16	16.96	16.94
7.14	12	90	3	18.13	17.46
7.14	12	90	6	16.52	16.72
7.14	12	90	12	17.94	17.2
7.14	16	90	4	16.59	17.32
7.14	16	90	8	19.31	17.47
7.14	16	90	16	17.53	16.98

It also was necessary to consider the effects of flaws located out of the locations between two stirrups. These tests are configured with flaws of 4.77% and 7.14% at relative distances of 0.25, 0.5, and 1.0, as listed in Table 4-6.

Figure 4-19 shows that the effect of the distance of the flaw on the stirrup's amplitudes is different for 12 inches and 16 inches while the flaw is located outside of two stirrups. For the stirrups' spacing of 12 inches and a flaw of 2.38%, Figure 4-19-a, a significant variation of amplitudes of both stirrups is observed so that the pulses' interference causes minimum amplitude at the relative distance of 0.50. For the stirrups' spacing of 16 inches and a flaw of 4.77%, Figure 4-19-b, a significant variation is recorded for the first stirrup so that the pulses interference causes minimum amplitude at the relative distance of 0.50.

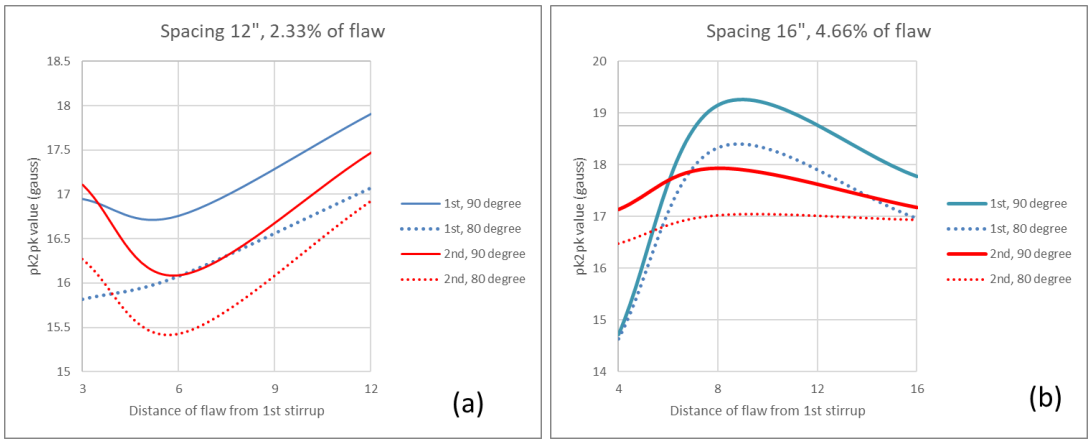

Figure 4-19: Effects of outward located 4.77% flaw on the stirrups amplitudes (a) 12" of spacing with 80 and 90 degrees of orientation angle, and (b) 16" of spacing with 80 and 90 degrees of the orientation angle

Figure 4-21 shows a comparison for two stirrups' amplitudes versus several positions of flaws, which is consistent for both 12 and 16 inches of stirrups' spacing. The flaws' percentages in these plots are calculated per one strand such that the flaws of 28% and 43% are corresponding to 4.77% and 7.14% per all strands.

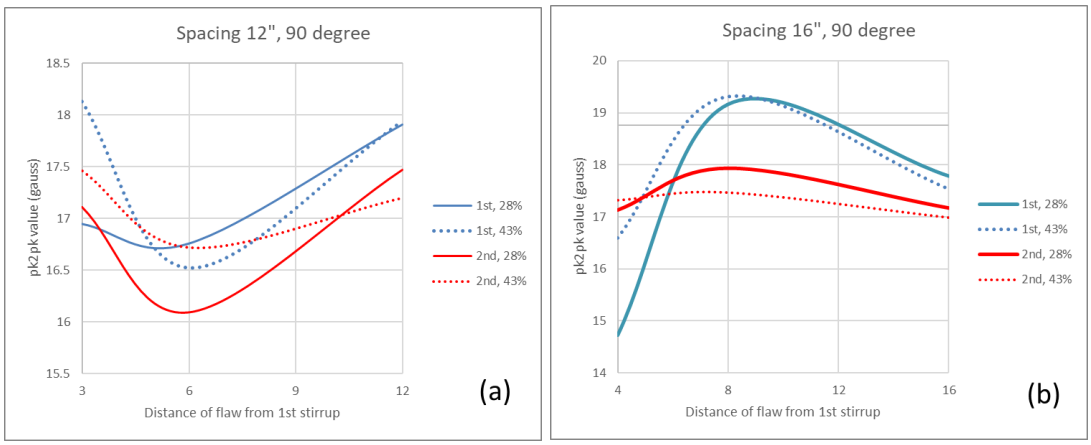

Figure 4-20: Comparison of Outward Located Flaw for Stirrup Spacing of a) 12" and b) 16" distance

4.7 Design of experiment

The MFL apparatus has demonstrated its reproducibility through laboratory and field evaluations earlier (Azari, Ghorbanpoor, & Shams, 2020; A. Ghorbanpoor et al., 1991; A. Ghorbanpoor et al., 2000). Therefore, the experiments have been done with no repetition to validate results through statistical means, and a design of experiments was conducted considering no repetition and only one sample has been tested for each experimental case.

Using full factorial analysis as a Design of Experiment (DoE), the importance level of each parameter in our experiments was evaluated. In this analysis, the flaws' percentage, the stirrup distance (SD), the flaw distance from the first stirrup (FD), and the orientation angle of the stirrups (Angle) were considered as design parameters. The calculated P-Values[3] are shown in Figure 4-21. As expected, the percentage of flaw is the most important factor in our analysis. The FD and the orientation angle are in the next priorities. Uniformity evaluation of standardized error for the first and second stirrup amplitude is presented in Figure 4-22. It shows a normal distribution of residuals

[3] P-value indicates the probability that a factor does not affect the response of the experiment. Considering the confidence interval of 95% for this study, the factors with P-values of less than 0.05 are considered significant on the response, which is the amplitude of stirrups in our study.

for the first and second stirrups' amplitude, confirming that the errors of this factorial analysis are randomly distributed.

Analysis of Variance

Source	DF	Adj SS	Adj MS	F-Value	P-Value
Model	35	3293.21	94.092	169.71	0.000
Linear	7	2118.69	302.670	545.91	0.000
Flaw (%)	3	1066.94	355.645	641.46	0.000
SD	1	0.02	0.023	0.04	0.843
FD	2	1055.80	527.901	952.15	0.000
Angle	1	11.21	11.211	20.22	0.001
2-Way Interactions	17	1107.34	65.138	117.49	0.000
Flaw (%)*SD	3	3.98	1.325	2.39	0.130
Flaw (%)*FD	6	1059.77	176.629	318.58	0.000
Flaw (%)*Angle	3	3.96	1.320	2.38	0.131
SD*FD	2	38.39	19.195	34.62	0.000
SD*Angle	1	0.20	0.198	0.36	0.563
FD*Angle	2	3.50	1.749	3.15	0.087
3-Way Interactions	11	19.88	1.808	3.26	0.036
Flaw (%)*SD*FD	6	18.34	3.057	5.51	0.009
Flaw (%)*SD*Angle	3	1.41	0.469	0.85	0.499
SD*FD*Angle	2	1.39	0.693	1.25	0.328
Error	10	5.54	0.554		
Total	45	3298.75			

Figure 4-21: Factorial Analysis Output

In what follows, using full factorial analysis, Figure 4-23 has been provided to show interactions between design parameters. Considering discussions in the previous section, the variation of the first stirrup's amplitude is of more interest than that of the second stirrup. As expected, there is no major significant interaction of factors for the first stirrup's amplitude, as shown in Figure 4-23, which simplifies the interpretation of results of experimentations. Moreover, the interaction containing flaws presents bigger effects on the response, illustrating the highest importance of the flaw in our analysis.

The 3D plots for variations of the stirrups' amplitudes by the effect of flaw percentage and its relative distance, the stirrups' spacing, and the orientation angle of stirrups are shown in Figure 4-24. The surface response illustrates the higher variability of the first stirrup's amplitude than that of the second stirrup.

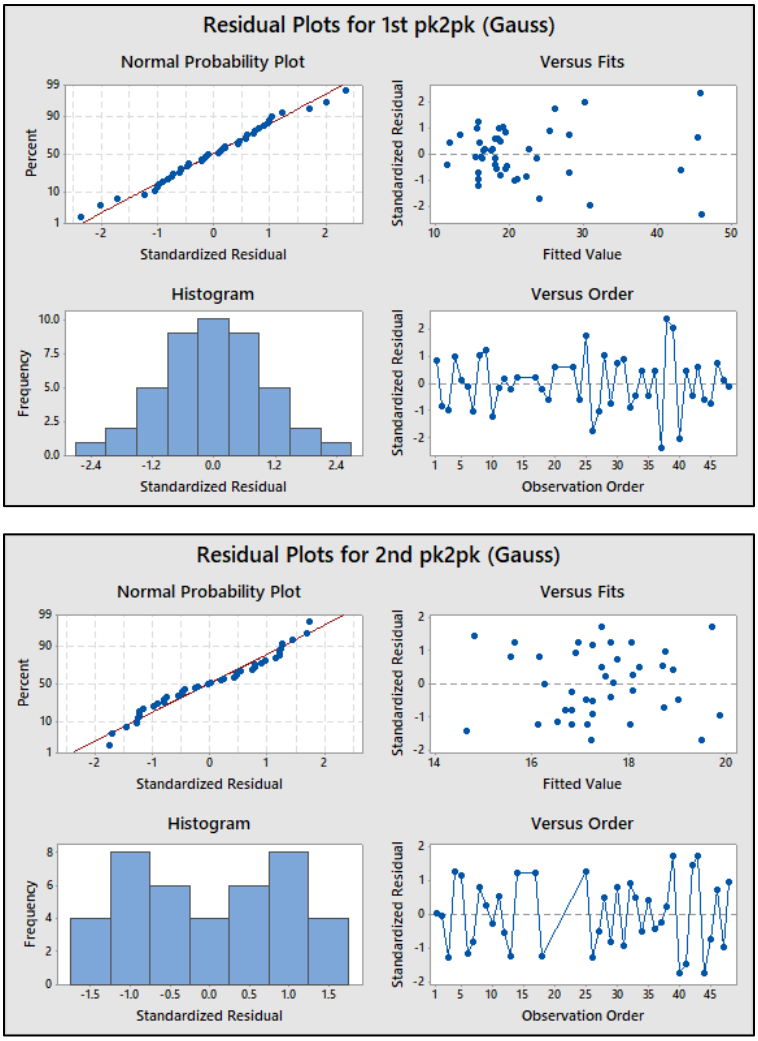

Figure 4-22: Uniformity Evaluation of Results

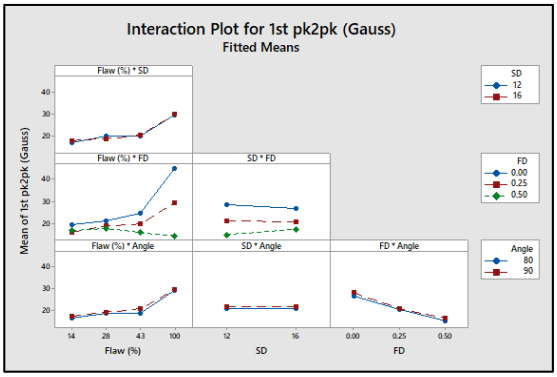

Figure 4-23: Interaction plots

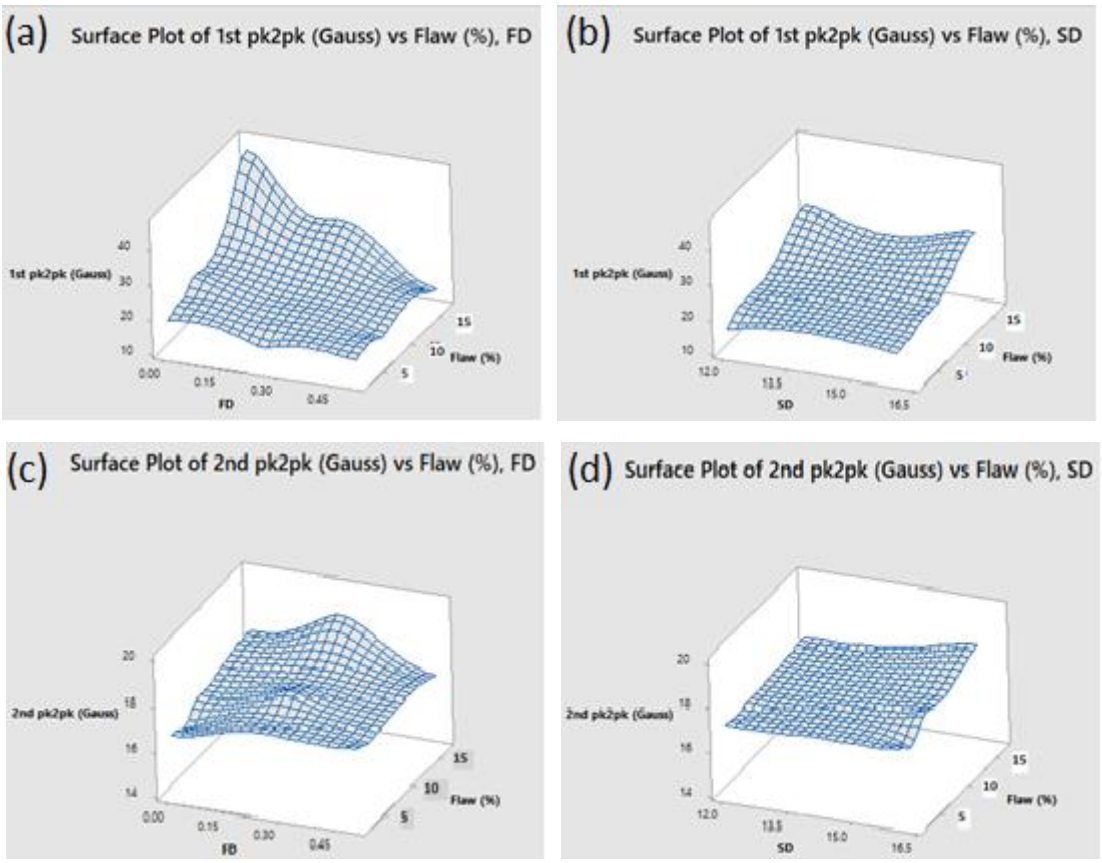

Figure 4-24: 3d plots for first and second stirrups amplitude variation (a), (b),(c), & (d): (a) first stirrup amplitude considering the effects of percentage and distance of flaw from stirrup (FD), (b) first stirrup amplitude considering the effects of the percentage of flaw and stirrups spacing (SD), (c) second stirrup amplitude considering the effects of percentage and distance of flaw from stirrup (FD), (d) second stirrup amplitude considering the effects of the percentage of flaw and stirrups spacing (SD)

4.8 Chapter summary

In this chapter the experimentation results were shown based on several configuration of stirrups, i.e., different spacing and orientation angle. Multiple percentages of flaws are located at different distances from stirrups. The variation of MFL pulses were measured by effects of stirrups spacing and orientation angles, flaw's percentages and, distances of flaw using the MFL apparatus and analyzed through the factorial analysis. The flaw's percentage and its distance from stirrups and, stirrups spacing were found as significant factors on the MFL pulses variation.

Chapter 5 **Flaw Characterization Using Signal Processing**

In this chapter, a methodology is presented to characterize the flaws in prestressed concrete girders to identify the location of a flaw and its geometrical properties through conducting signal processing on the MFL signals. The signal processing is based on employing correlation analysis and pattern recognition.

5.1 Methodology outlines

The proposed methodology (shown in Figure 5-1) is briefly explained in the following:

- *Signal filtering*

  It is possible to have high-frequency noises, outliers, or spikes in the MFL signals from measurement apparatus and artifacts in test subjects. Signal noise is removed through common signal filtering techniques such as wavelet transformation and a median filter.

- *Demonstration of superposition of effects*

  A superposition of effects indicates that the individual effects of stirrups and flaws can be superimposed to generate a test case with multiple stirrups and flaws. This is a primary factor for the next steps of signal processing in which decomposing of signals is necessary.

- *3-D correlation analysis*

  This analysis is based on performing the correlation analysis on the signals given from all channels of the MFL apparatus. Using pattern recognition techniques, the position of a flaw can be obtained. This step provides the following information:

  - The position and orientation angle of stirrups

- The location of the flaws such that it localizes flaws in both *x* and *y* axes, determining which strand contains the flaw and which stirrup(s) is the closest to the flaw.

- *Analytical method*

  Since a flaw affects the signals in the region of neighboring stirrups, an analytical study was done to assess the variation of stirrups' amplitude by the effect of a flaw. This analytical method employs a superposition rule and provides helpful information about how the amplitudes of a signal vary by the effect of a flaw.

- *2-D correlation analysis*

  This analysis is done on a signal from a specific channel. Since the location of the flaw is determined from the 3-D analysis, it is possible to find the nearest signal source, or data sensor (channel) number, to the flaw. Then, the 2-D analysis will be done on the signal produced by that channel. Compared with 3-D analysis, the 2-D analysis identifies the amplitude and duration of the flaw after removing the stirrup's effects from the MFL signals.

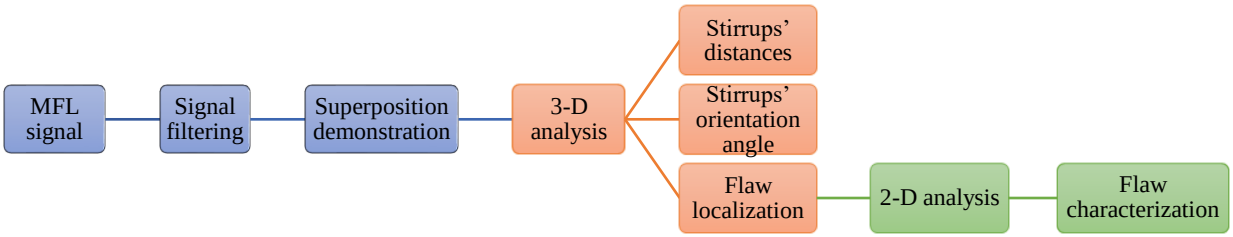

Figure 5-1: flowchart of the flaw detection methodology

The steps explained above requires high computational efforts. On the other hand, a high number of experiments is another challenge for signal analysis. Therefore, all steps are done

through coding in MATLAB that makes it feasible to perform analyses quickly and cost-effectively, in addition to the powerful features of data visualization.

5.2 Signal Filtering

While reading data from the MFL apparatus, digital disturbances may appear as noises in the experimental signals. These disturbances may be noises with a high frequency range or single pulses such as outliers or spikes. Although during the manufacturing of the MFL apparatus, signal filtering hardware and software components were added to the data acquisition unit, the signal filtering step is necessary to prevent any possible digital disturbance before starting the data analysis.

Multiple sources for noises and outliers during the acquisition of MFL signals include the following:

- Vibration due to the motion of the MFL apparatus
- Roughness of the surface of the test in presence of other ferrous parts in the test board, which was anticipated.

The measurement of digital noises has demonstrated that it is reasonable to eliminate the noises with more than 5 Hz frequency. Based on pulses' properties for flaws and stirrups, the frequency range of MFL related pulses is mostly less than 2 Hz. In the worst case, for flaws with a very low section loss percentage (i.e., around 1%) and located in the upper rebar layers (i.e., with an embedment depth of around 6 inches), a frequency of about 5 Hz is determined. Figure 5-2 shows the frequencies determined for a stirrup and a flaw of 2.38% at a depth of 2.25 inches. The stirrup's pulse has a length of 20.8 inches, which corresponds to a low frequency of about 0.3 Hz and a 1.9-inch-long pulse for the flaw has a higher frequency of 3.31 Hz. The flaw in this figure

has a length of a third of an inch, which is a short flaw, corresponding to a higher frequency, in comparison with possible long corrosion-related flaws with much lower frequencies in structures.

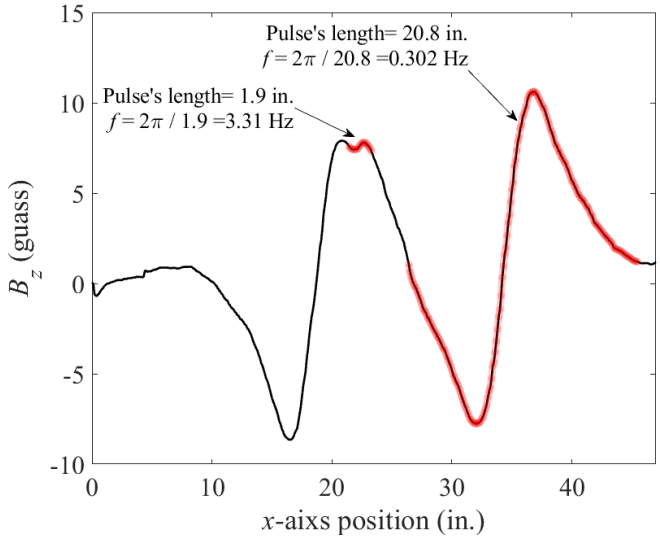

Figure 5-2: frequency determination for MFL pulses

Wavelet transformation to filter out digital noises

To remove high-frequency noises, a wavelet transformation algorithm is selected, which is a pre-defined function in MATLAB by the name of 'wden.' Figure 5-3 shows an example of applying the wavelet transformation result on a noisy signal. Depending on the frequency range of noises, a filtering level would be assigned to a wavelet function such that the smoothness of the signal changes accordingly. As shown in Figure 5-4, level 3 of the wavelet transformation was implemented on the vertical and longitudinal components of magnetic fields. The noises have mostly disappeared after imposing the wavelet transformation so that the signal is prepared for analysis.

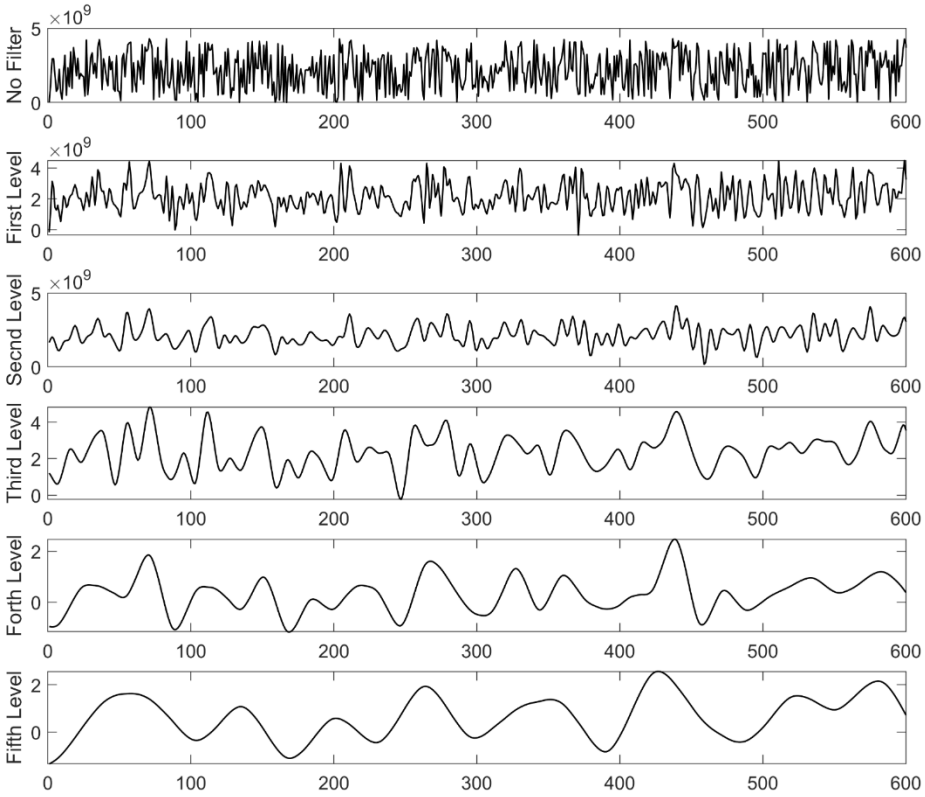

Figure 5-3: Wavelet Transformation Sample, “wden” Function in MATLAB

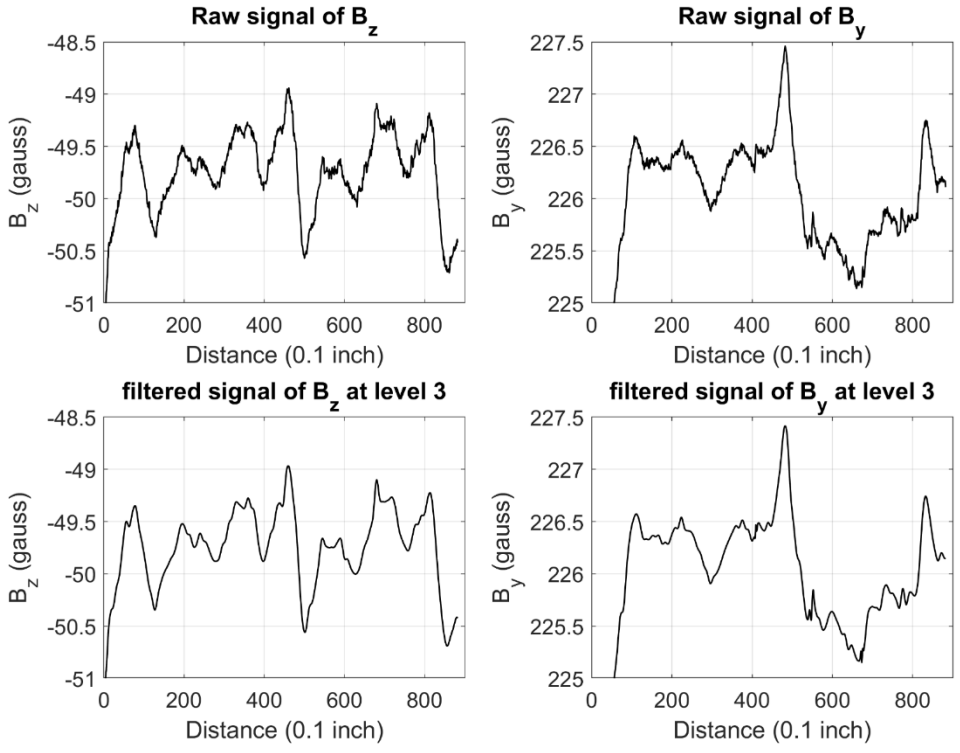

Figure 5-4: a level 3 of wavelet filtering of a noisy sample of MFL signal, wden Function

Median filter to clean spikes

Due to electromagnetic interferences, outliers or spikes may occur in the MFL signal that might adversely affect the data analysis. To clean the signal out, a ‘median’ filter is selected as an effective tool for spikes or outliers removal as shown in Figure 5-5. The ‘median’ filter is implemented using a pre-defined function in MATLAB with the same name.

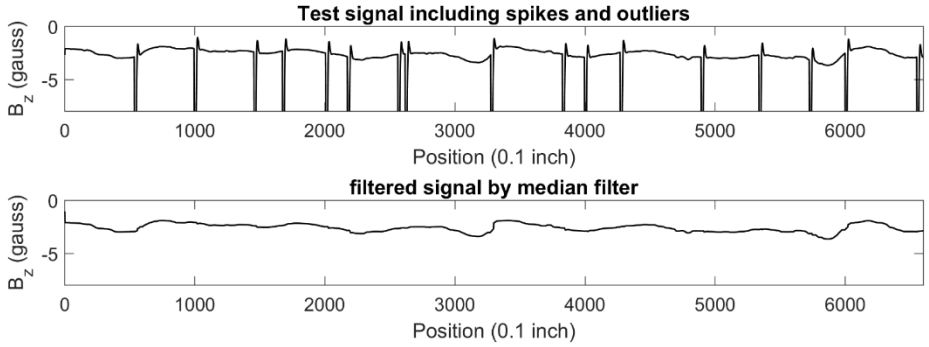

Figure 5-5: Applying Median Effect on the Spike Removal, median Filter Function

5.3 Analytical method of signal generation

This method is developed to construct a digital twin for the magnetic response in test samples to generate virtual signals for any configuration of stirrups and flaws. The analytical method generates artificial signals based on the superposition of equation-based single-pulse signals. The assumption of linear variation of pulses’ amplitudes versus flaw size is crucial to employ the superposition law for this study. This assumption is validated earlier in Figure 3-16 and Figure 4-8. There are two major outputs from the analytical method:

1. *Single-pulse signal* is generated based on equation (5-1) by giving *a*, *b*, and the center-point of the signal as inputs. Accordingly, there is only one pulse may exist with a specified amplitude and duration. In Figure 5-6, the first three signals are single-pulse signals generated by an analytical method with different amplitudes and duration.

2. *Multi-pulse signal* is generated based on the superposition of single pulse signals with the same overall length. A multi-pulse signal may contain pulses with different amplitudes and duration in addition to arbitrary spacing of components. The bottom plot in Figure 5-6 shows the signal B_z that is determined from a summation of three one-pulse signals (B_{z1}, B_{z2}, and B_{z3}).

Multi-pulse signals as shown in Figure 5-7 create a digital twin of experimental MFL signals with an arbitrary configuration of stirrups and flaws.

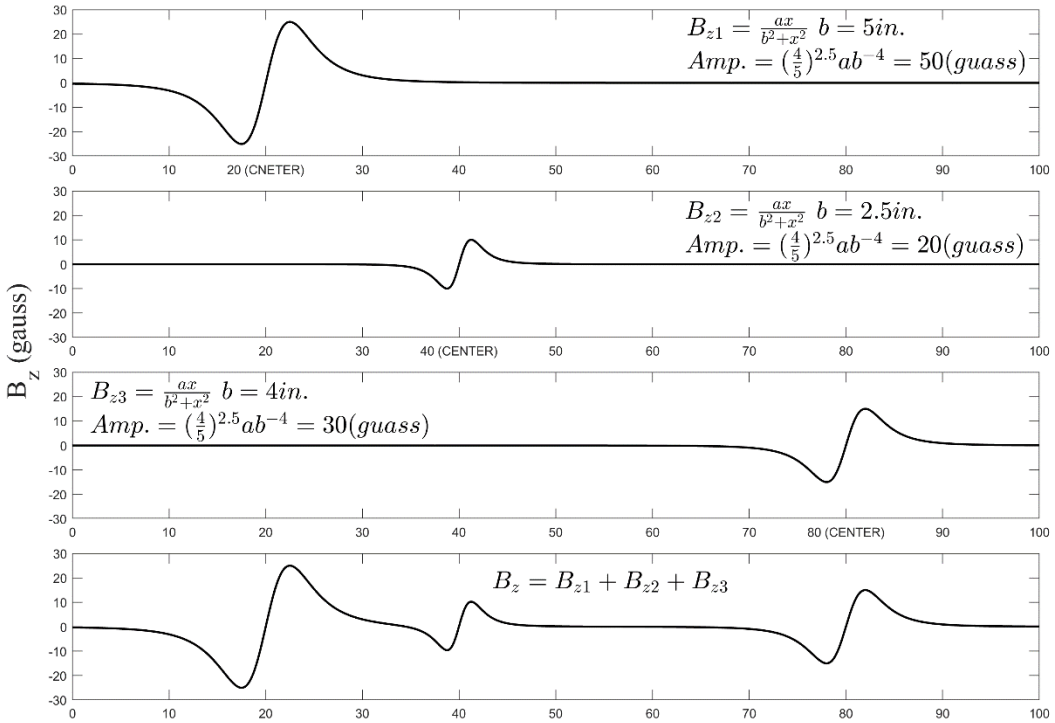

Figure 5-6: equation-based signals generated by analytical method

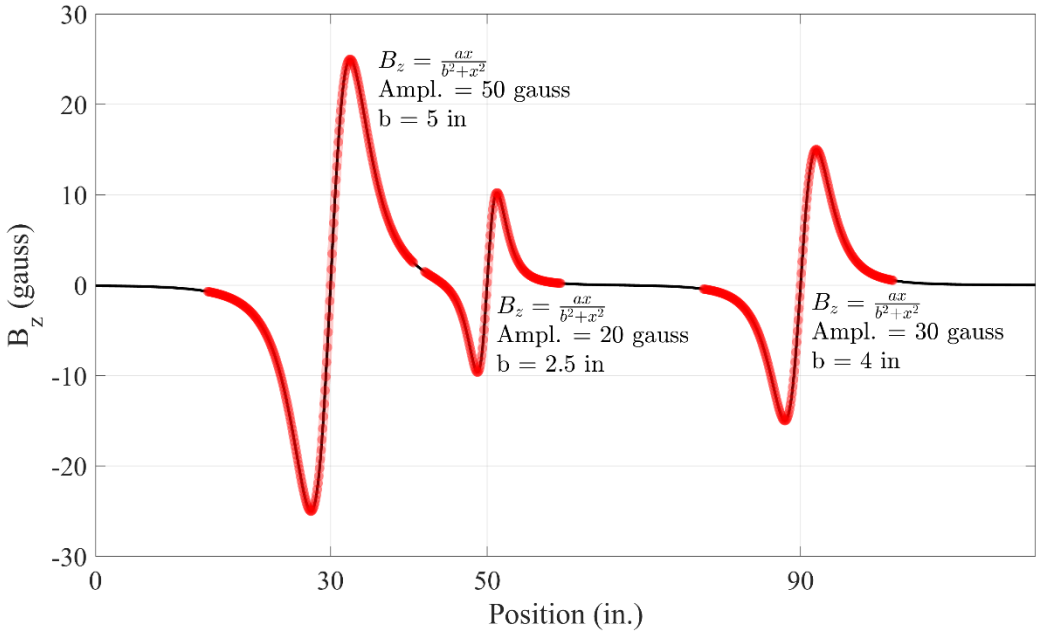

Figure 5-7: a multi-pulse signal from the analytical method

The analytical method enables visualization of each configuration of stirrups and flaws and makes it possible to track the effect of a flaw on a MFL signal. The signals in Figure 5-8 are related to a virtual case with three stirrups spaced by 16 inches. From the top plot to the bottom plot, the flaw's position is marked by a single grid line and changes from the x = 24 inches before the second stirrup to x = 36 inches at the third stirrup. An advantage of the analytical method is its feasibility to assess the variation of amplitudes and duration of stirrups' pulses versus the position of the flaw, which is discussed thoroughly later in this chapter.

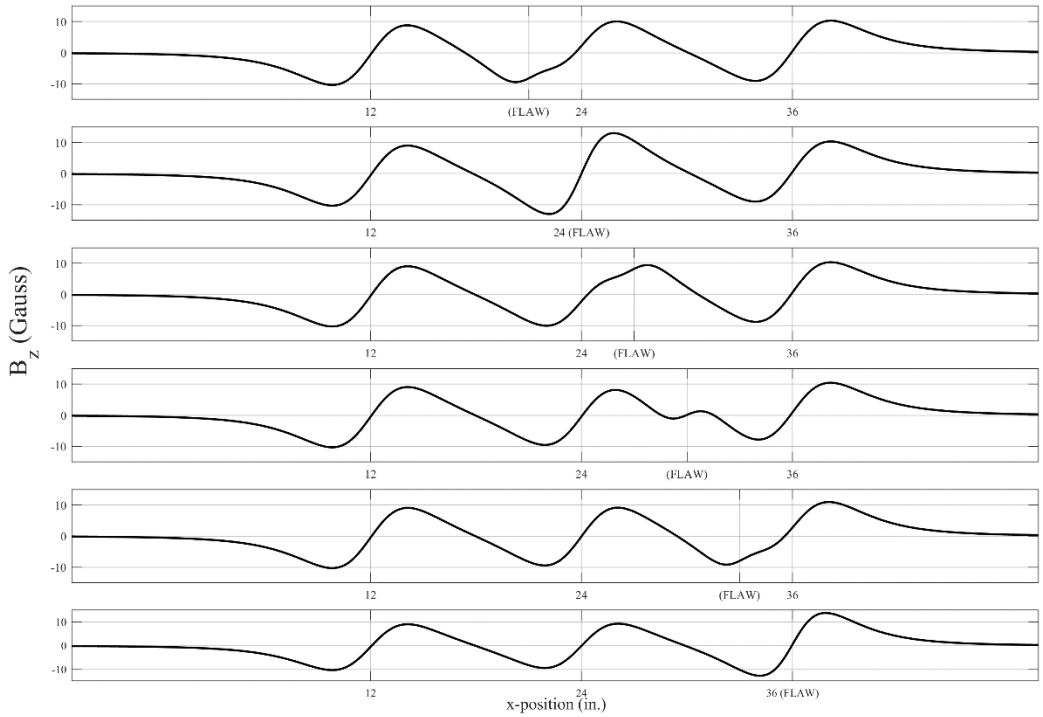

Figure 5-8: simulation of different positions of a flaw in a specific configuration of stirrups

5.4 Demonstration of superposition of effects on MFL signals

To implement the next steps of signal processing in this study, it is necessary to demonstrate the superposition of the effects of individual sources of MFL on the test signals. Since the linear variation of amplitudes for flaw size is demonstrated earlier (see Figure 3-16 and Figure 4-8) it will serve as the basis of implementing the superposition principle to analyze MFL signals from the combined effect of different contributing sources, this section elaborates on how the superposition of effects governs the MFL signals and validates it through the assessment of signals given from the MFL apparatus, simulations, and analytical method.

The magnitude of the vertical field variation for a single pulse, B_z, in the vicinity of a stirrup or flaw can be approximated by Equation (5-1), as shown in Figure 5-9(a), where *b* is the peak-to-peak spatial distance and *x* is the distance of any point on the pulse from the center of the flaw (A. Ghorbanpoor et al., 1991; A. Ghorbanpoor et al., 2000). The coefficient *a* in Equation (1) is taken

as $a = \left(\frac{5}{4}\right)^{2.5} \times Amp \times b^4$ in which *Amp* is the peak-to-peak amplitude of the pulse. The measured magnitudes of *Amp* and *b* values, without any influencing factors, for No. 4 reinforcing steel stirrups and various size flaws, are listed in Table 5-1. The magnet blocks were spaced by 2.25 inches from the center of stirrups.

$$B_z = \frac{ax}{(b^2 + x^2)^{2.5}} \qquad 5\text{-}1$$

These values were measured using the MFL device and test conditions as described above. To study the influence of magnetic signals produced by stirrups and flaws, a series of signal superpositions is performed analytically with varying relative positions of flaws and stirrups. Figure 5-9(b) and 2(c) show magnetic signals in the presence of a small and a large flaw, respectively, between two adjacent stirrups. In the Figures, the unaltered stirrup signal amplitude without the effect of a flaw signal is identified as a_s and the unaltered flaw signal amplitude is shown as a_f. When the stirrup signal amplitude is altered due to the presence of a nearby flaw signal, the stirrup signal amplitude is identified as *a*.

To verify the accuracy of the MFL signal superposition through the analytical method, signals from MFL tests were compared with signals given from analytical and numerical simulation models under the same conditions. The signals are for an experimental case with stirrups #4 and a magnet depth of 2.25 inches. Selected magnetic field signals shown in graphs (a) to (f) in Figure 5-10 offer a good agreement between analytical, numerical simulation, and experimental MFL signals as well as demonstrating the effect of superposition of flaw signals on stirrup signals under different conditions, including different flaw sizes and locations.

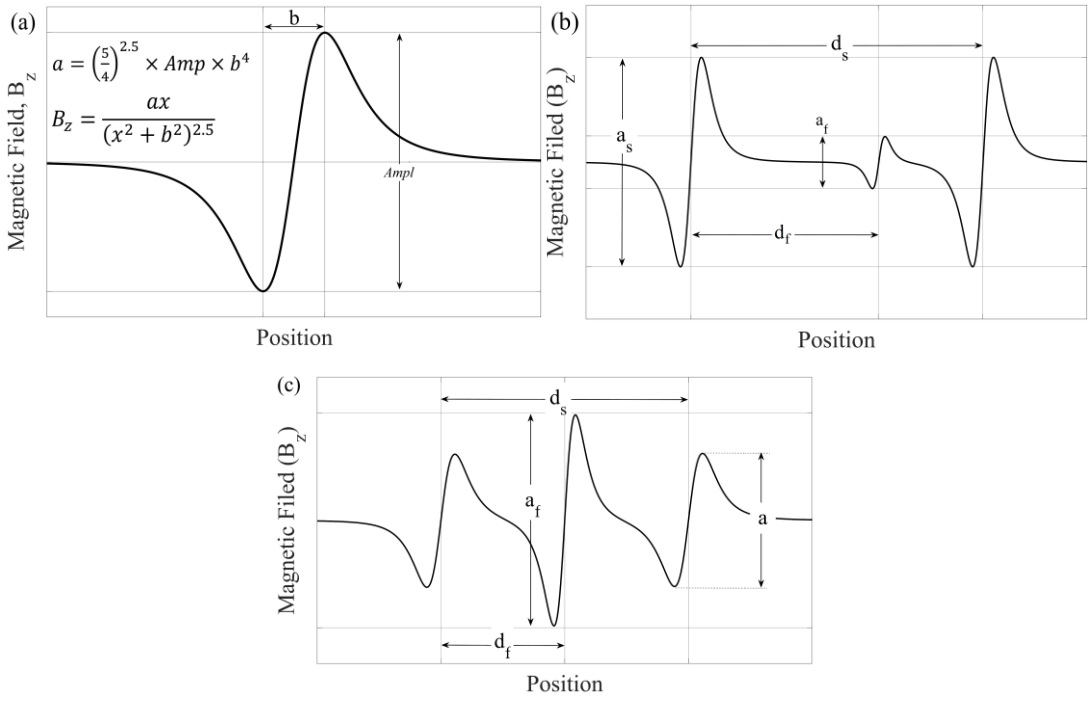

Figure 5-9: schematic view of signals for (a) an individual pulse from a stirrup (or a flaw); (b) a sequence of two stirrups and a small flaw located between the stirrups; (c) a sequence of two stirrups and a large flaw located between the stirrups

Table 5-1: measured magnitudes of amplitudes and durations for embedment depth of 2.25 in.

ID	*Ampl* (Gauss)	*B* (inch)
Stirrup (#4)	18.67	4.4
Flaw of 2.38% (1 wire cut)	4.96	2.4
Flaw of 4.77% (2 wires cut)	6.89	2.6
Flaw of 7.14% (3 wires cut)	10.44	2.6
Flaw of 16.67% (7 wires cut)	29.61	2.6

Figure 5-10(a) shows magnetic field signals from an analytical model, simulation, and a laboratory MFL test for two adjacent #4 conventional reinforcing steel stirrups, a flaw that represents a 16.67% section loss in a group of six prestressed strands, and a magnet depth of 2.25 inches. For this case, the flaw is positioned at the same location as the first (left side) stirrup.

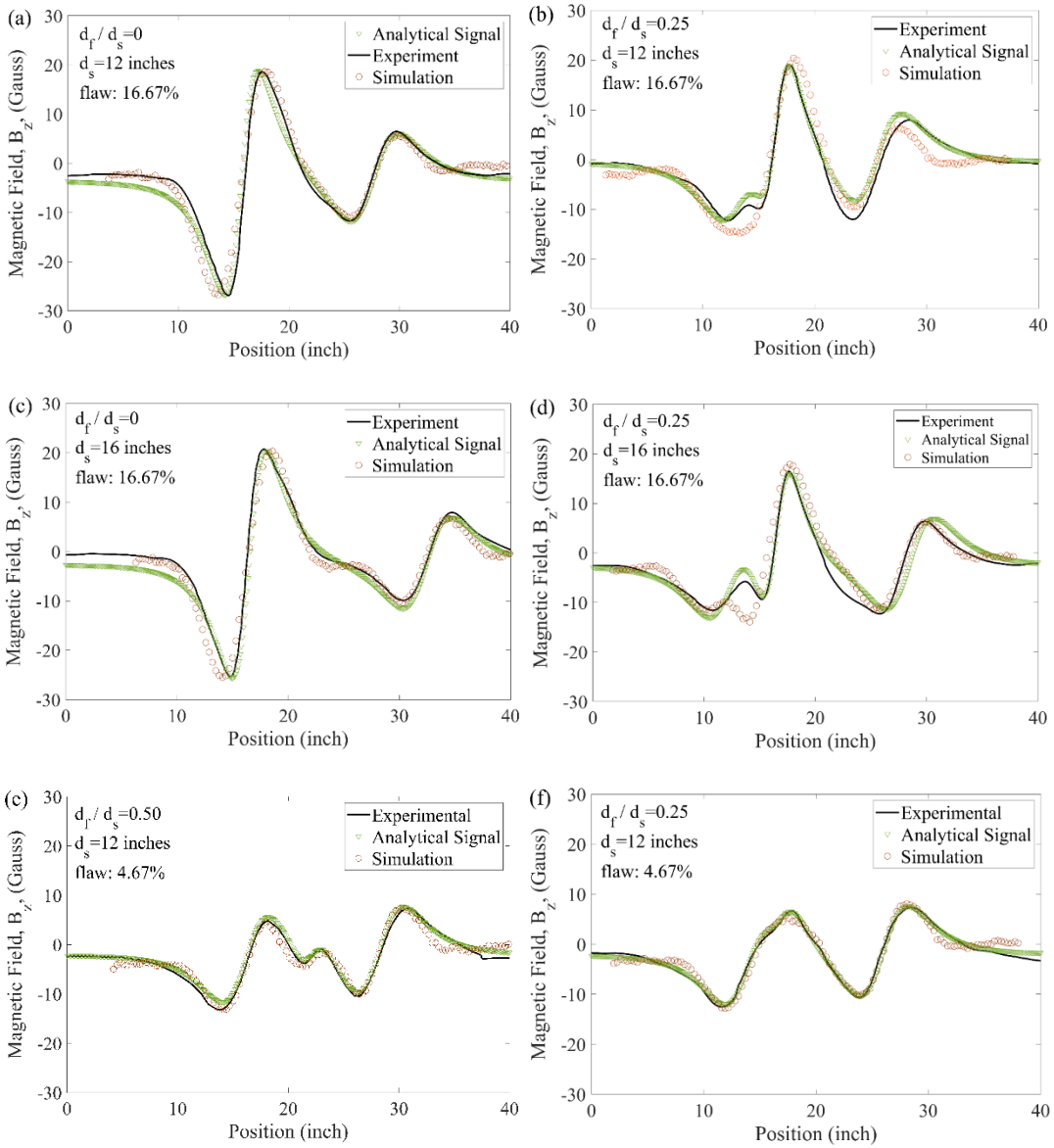

Figure 5-10: comparison of experimental and analytical signals to validate the superposition effects of flaw signals on stirrup signals

It should be noted that without the presence of a flaw, the magnetic field signals from the two adjacent stirrups would be identical; see Figure 5-9(b). However, Figure 5-10(a) shows a clear increase in the peak-to-peak amplitude for the first stirrup. The amplitude increase is the result of the direct superposition of the flaw signal on the signal from the stirrup. No additional features can be seen in the superimposed signal since there is no phase shift between the two superimposed signals. If the flaw location is moved to the first quarter-point between the two stirrups, for

example, additional features from the effect of the flaw will appear in the signal, Figure 5-10(b). The resulting signal shape results from the superposition of the stirrup signal and a strong flaw signal with a phase shift. Other graphs in Figure 5-10 show the results of the superposition of a flaw signal on the first stirrup under different conditions, as indicated in each graph. Similar results were observed for other cases with different flaw sizes, flaw locations, and distances between two adjacent stirrups.

The analytical signals, as artificial signals from superposition of individual effects, in Figure 5-10 have shown a good agreement with experimental and simulation signals that are resulted from sequences of stirrups and a flaw. As shown later in this chapter, artificial signals from analytical method are main part of flaw characterization process.

According to the above discussion and the fact that accurate magnetic signal characteristics may be obtained through MFL tests, it is reasonable to conclude that a good estimate may be made for a flaw size. This estimate may be achieved by considering the relative distance of the flaw with respect to the nearest stirrup (d_f/d_s) and the change of the magnitude of the stirrup signal amplitude as measured in a test. The normalized variation of the signal amplitudes for stirrups because of a nearby flaw signal is defined by the a/a_s ratio, which can be established from the analytical method, simulation, or experimental data for different conditions. This ratio may be considered as a useful index to characterize flaws, including the estimation of flaw size, along the length of prestressed steel strands embedded in concrete. Appropriate charts based on the variations of a/a_s vs d_f/d_s ratios may be constructed for geometric conditions commonly found in prestressed concrete girder construction to estimate flaw sizes after completing appropriate MFL tests. Graphs (a) and (b) in Figure 5-11 show constructed a/a_s vs d_f/d_s charts for selected stirrup spacing of 12 and 16 inches, respectively. Similar graphs may be constructed for other conditions,

including different stirrup spacing, and flaw sizes, and locations. Obtaining the values of a/a_s and d_s from a particular MFL test, as defined in this study, would allow the use of the charts such as those shown in Figure 5-11 that arrive at a good estimate of the flaw size.

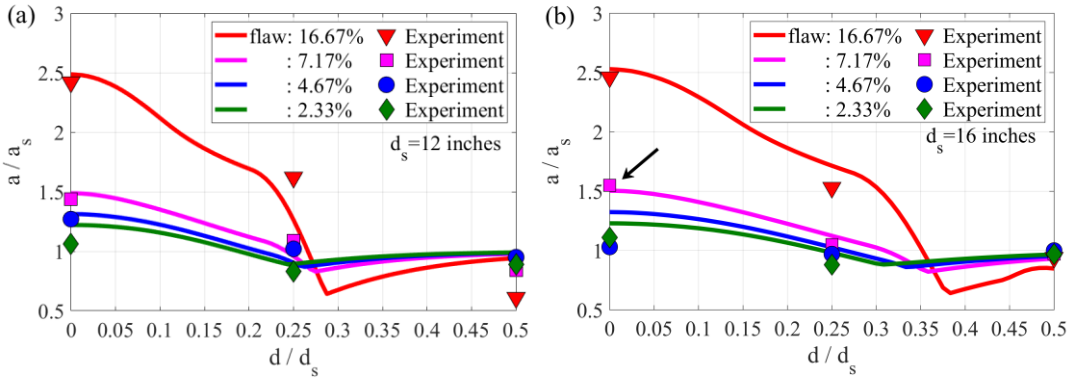

Figure 5-11: verification of analytical method results through experimental signals

To demonstrate the use of the constructed charts shown in Figure 5-11, consider the MFL signal shown in Figure 5-12. The graph shows a test signal obtained under a condition as described earlier but with stirrups' spacing of 16 inches and a known flaw size equivalent to a 7.14% section loss (three wires cut in a group of six strands). An examination of the test signal reveals that the flaw is positioned at the location of the first stirrup (or d_f/d_s = 0.0) and the measured signal amplitude at the location of the first stirrup is a=25.19 G. Accordingly, since $\frac{a}{a_s}$= 1.35 (considering a_s = 18.67 G from Table 5-1), one can arrive at an estimate of the flaw size of slightly less than 7% using chart (b), as shown in Figure 5-11.

To study the effect of stirrups' spacing and the influence from a flaw signal, a graph of the variation of amplitude ratio index (a/a_s) of the first stirrup against the changing values of the d_f/d_s ratios is constructed for different stirrups spacing and a flaw of 16.67% (Figure 5-13). For the rare cases where stirrups' spacing for a test girder cannot be determined from available

engineering drawings or MFL tests, Figure 5-13 shows that the flaw size accuracy may be compromised when a flaw is located within the d_f/d_s ratios of between 0.15 and 0.45.

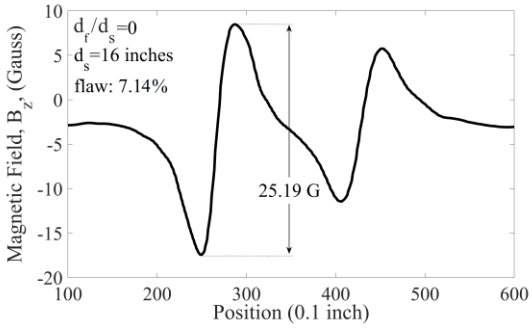

Figure 5-12: the MFL signal for a flaw of 7.14% located at the position of the first stirrup

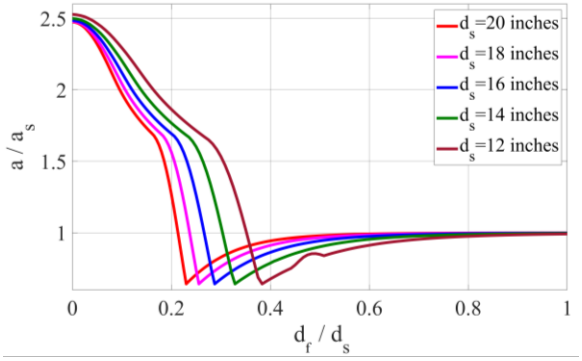

Figure 5-13: variation of first stirrup's amplitude versus relative distance of flaw from first stirrup (d_f/d_s) for several amounts of d_s

Corrosion-related flaws in prestressed steel of concrete girders often produce magnetic signals that include signal characteristics that are different from those produced by man-made flaws. The most distinct difference in such magnetic signals is a relative increase in the peak-to-peak signal duration, b_f. To study the effect of such an increase on the magnetic signals, analytical models were performed considering the stirrup amplitude ratio index $\frac{a}{a_s}$. Figure 5-14 shows the results of the analytical model for a flaw with a section loss equivalent to 2.38%, or a single wire cut, in a group of six strands. As shown in the Figure, an increasing signal peak-to-peak duration can adversely affect the accuracy of flaw size estimation. For most practical cases, however, the

signal duration increases fall within the lower bound of the values shown in the Figure (i.e., b_f = 2 to 5 inches), which would be acceptable for arriving at a reasonable estimate.

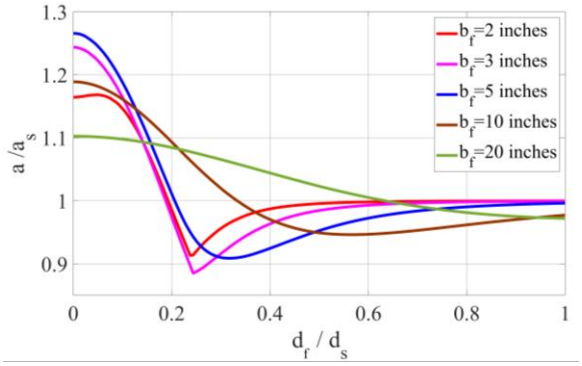

Figure 5-14: variation of first stirrup's amplitude versus relative distance of flaw from first stirrup (d_f/d_s) for several amounts of b_f

5.5 Removing the stirrups' effects using the correlation analysis

Since the cross-section area and length of stirrups in prestressed concrete girders are expectedly constant, the MFL signals at the location of each stirrup would be identical. Moreover, the distance of stirrups may be the only variable factor for stirrups. Therefore, given the spacing information of stirrups, it is feasible to generate an artificial signal containing stirrups' effects through the analytical method.

In this section, the application of correlation analysis is illustrated to determine the stirrups' spacing. As mentioned earlier, the pattern of the MFL signal for a stirrup follows the equation (5-1) (A. Ghorbanpoor et al., 2000). Considering the signal amplitude as the distance between the two peaks of the diagram in Figure 5-9(a), the magnitude of coefficient a in equation (5-1) is calculated as:

$$a = \left(\frac{5}{4}\right)^{2.5} amp \times b^4 \qquad 5\text{-}2$$

and b is the duration of the signal, which is the horizontal distance between two peaks.

Therefore, a generated reference signal based on equation (5-1) can be employed to perform the correlation analysis in which the points with high correlation values are determined as stirrups. The reference signal does not need to be exactly matched with the existing stirrups' signal since the similar pattern provides an adequate correlation value.

There are some considerations in the correlation analysis to detect the stirrups' locations:

1. *Inconsistent pulses amplitude and duration*

   Considering numerous stirrups in real cases, it is easy to identify the amplitude stirrups' pulses in the MFL signal through a statistical assessment such that an average value is identified for amplitude and duration of pulses for stirrups. Then, any other sources of MFL that show different properties will not be reported as a stirrup.

2. *Inconsistent spacing*

   Conveniently, the stirrups' spacing follows consistent patterns such that there are several stirrups with a specific distance next to each other. Because of design provisions, the spacing may change along with the member. Implementing the correlation analysis will determine the spacing patterns used for the member and an inconsistency occurs when any diagnosed stirrup does not follow the spacing pattern.

After identification of stirrups' location, an artificial signal is generated providing the average amplitude and duration at the locations of the diagnosed stirrups.

Figure 5-15 shows the result of correlation analysis on an MFL signal for a series of stirrups #4 spaced by 16 inches along the sample with an embedment depth of four inches. Given experimental signal information for stirrup #4, an artificial reference signal was generated. The correlation diagram shows a high correlation of reference signal that is almost 1.0, illustrating a good performance of the reference signal. Considering the correlation values' diagram, the location of the stirrups was detected, presenting consistency of amplitudes, durations, and spacing.

To find the location of the stirrup it is necessary to define a threshold value for the correlation analysis as an acceptable range, which is set in a range of 0.75 to 1.0 for stirrups.

The next step is the creation of an artificial signal containing the effects of stirrups at the detected positions. This is done through the analytical method by superposition signals from each stirrup as shown in Figure 5-16, which has special characteristics:

1. It is a smooth signal.
2. It does not include other sources of MFL.
3. The amplitude and duration values are provided at the detected location of stirrups.

Subtraction of the artificial signal from the test signal will remove the effects of stirrups and retain other effects on magnetic fields such as flaws, chairs, and other ferrous materials.

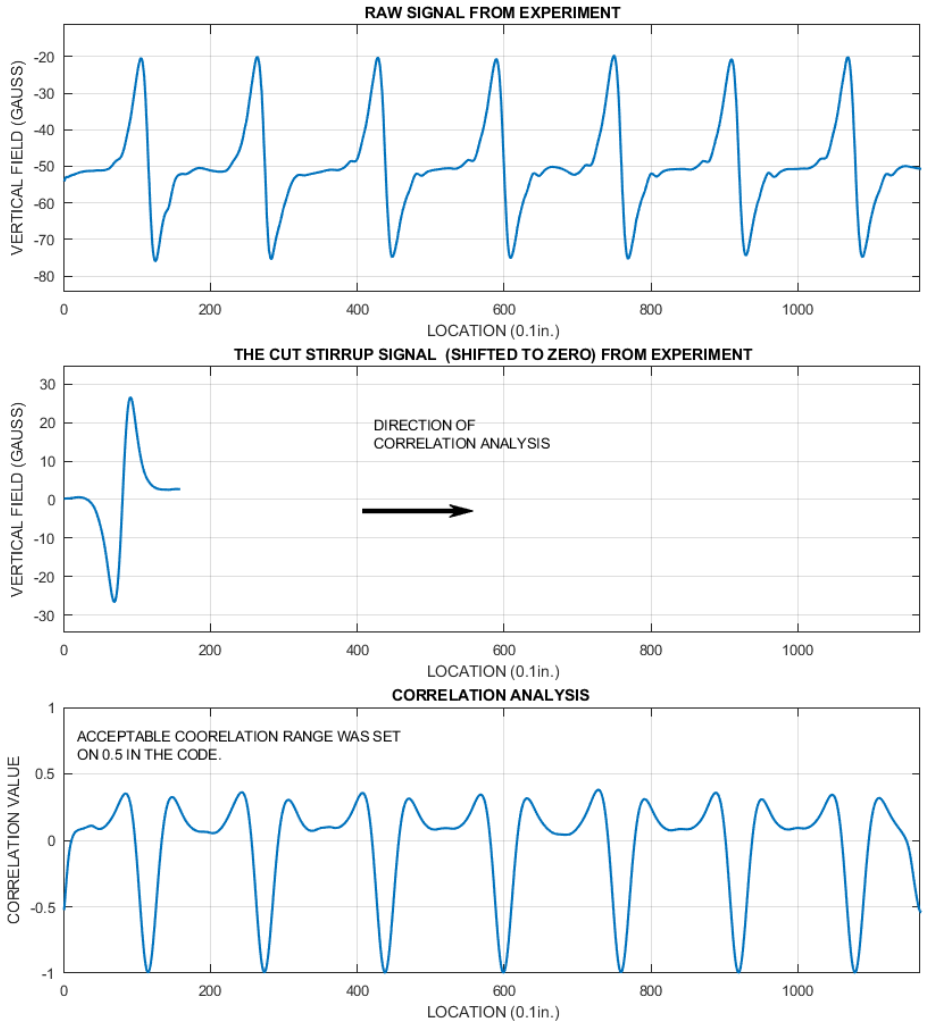

Figure 5-15: Results for Correlation Analysis

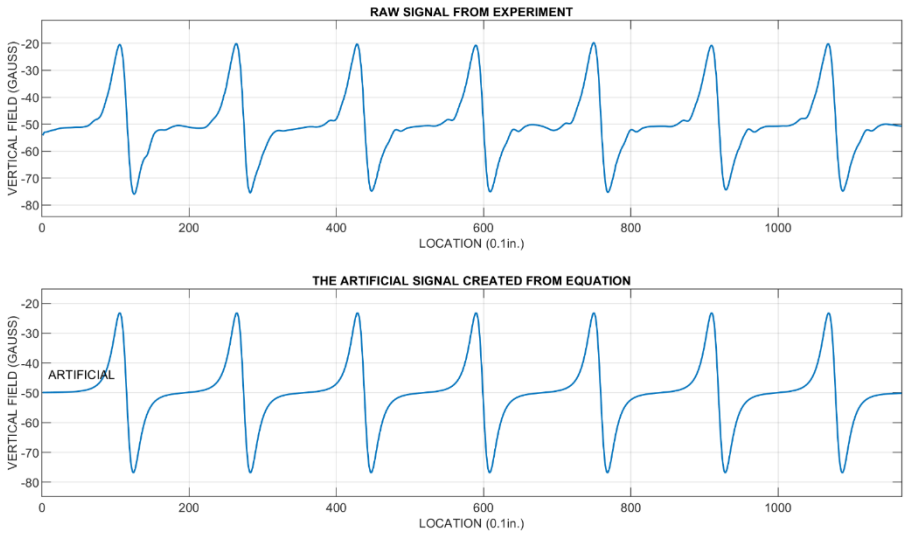

Figure 5-16: Combined Idealized Signal from Stirrups

5.6 3-D correlation analysis to detect flaws

One of the key steps of signal analysis is identification of the stirrups' positions and orientation angles. Knowing the positions of stirrups, it is feasible to remove the stirrups' pulses from a recorded MFL signal. Then, the filtered signal is prepared for characterization of MFL sources rather than stirrups.

The main goal of 3-D analysis is localization of stirrups along with the pre-stressed concrete member and initial localization of possible points of the flaw. Usually there are documentaries of as-built structural drawings relating to the stirrups and strands arrangements for structural members that can be used as a reliable source to verify the position of stirrups detected by 3-D analysis. The spacing of stirrups and their embedment depth are easily extracted from the structural drawing sheets. Moreover, the number, size, splices' positions, spacing, and embedment depths of strands are other important information from the drawing sheets that helps to localize the flaw more accurately. Later in this section, it is shown that how the 3-D analysis approximately identifies which strands contains a flaw. Matching the result with the structural drawings leads to improve the diagnosis.

The 3-D analysis is taken in three general steps to identify the stirrups' arrangement and initial flaws' localization.

1. Conducting the correlation analysis on the MFL signals from all channels
2. Performing a pattern recognition-based algorithm to distinguish between stirrups and flaw and, identification of stirrups orientation angles
3. Detecting the approximate location of the flaw that identifies where the flaw is located along the member and what is the closest channel (or strand) to the law.

These steps require implementing high computational efforts, which is done through coding in MATLAB.

Considering that there are 32 Hall-effect sensors located along the *y*-axis at the center of the MFL apparatus, it is possible to assess the variation of B_z in both the *x* and *y* directions as shown in Figure 5-17. A schematic view of the test configuration is shown in which two stirrups have a distance of *s* and the flaw is in a distance of a fraction of *s* with respect to the left stirrup, which is defined by D. Moreover, the flaw is located on the third strand from the top.

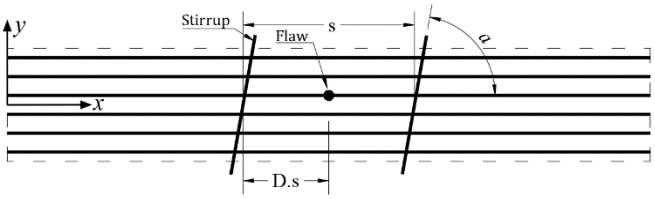

Figure 5-17: schematic view of tests samples defining the stirrups' spacing (s), distance ratio of the flaw from the first stirrup (D), and orientation angle of stirrups (a)

The first step of signal processing is the detection of the stirrups' location through correlation analysis, which removes the pulses of stirrups from the test signal. To perform correlation analysis, a reference signal containing a single stirrup pulse is utilized.

The first case of investigation contains six strands, two stirrups #4 (s=16 in. and α=90°) no flaw, and an embedment length of 2.25 inches. Initial correlation analyses were performed on signals given from all sensor channels. The correlation analysis reports points with correlation values of more than 0.75. Therefore, for each stirrup, it is expected to have 32 detected points from sensor channels as shown in Figure 5-18(a). The linear orientation of detected points (shown by black dots) verifies the orientation angle of α=90° for both stirrups and spacing of 16.2 inches. Figure 5-18(b) represents the MFL signal from all channels, which is drawn in a contour plot (Figure 5-18(c)) all around the test specimen representing the variation of the vertical magnetic

field (B_z) by effects of stirrups. Good conformity of correlation analysis with the experimental contour plot demonstrates the performance of correlation analysis for detection of stirrups.

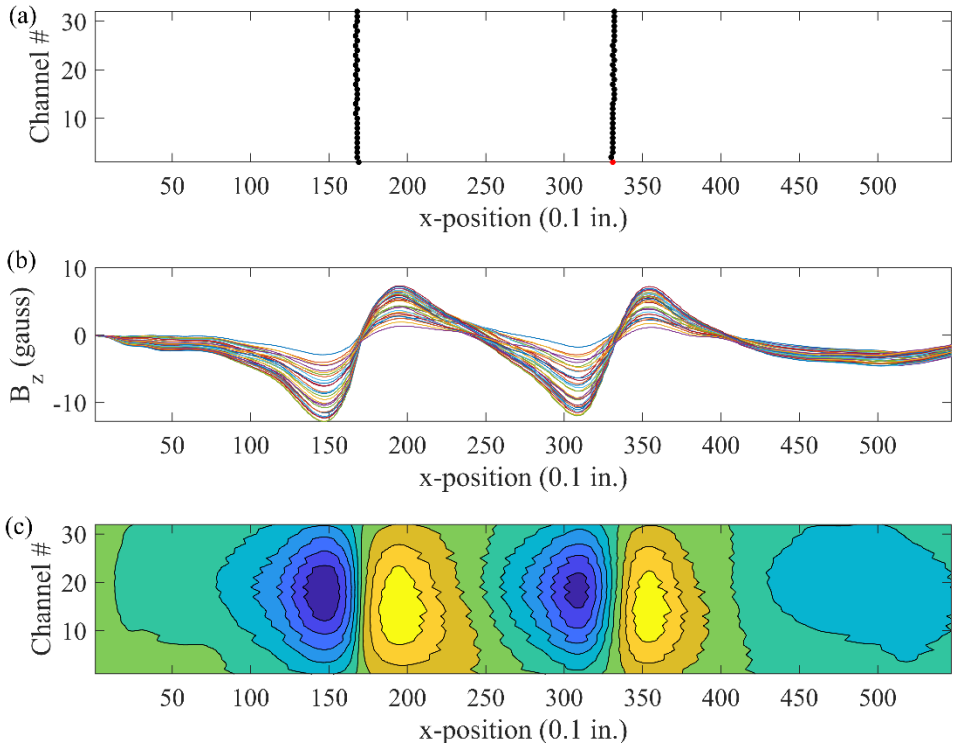

Figure 5-18: correlation analysis result for the case with two stirrups by s=16", *a*=90°; (a) correlation analysis result illustrating the position of stirrups, vertical field (B_z) variation for all channels, and (c) contour plot of vertical field (B_z) variation for all channels

The closed contours on either sides of the stirrups illustrate that the amplitudes of the pulses produced from each stirrup are different for sensors according to their positions, i.e., the maximum amplitudes occur closer to the middle of the stirrups. This is described earlier in section 4.1, Figure 4-1(g). The profile of variation of amplitudes for all channels is shown in Figure 5-19(a) so that it illustrated validity of 97% with a quadratic regression curve. Equation (5-3) shows the quadratic regression model used to define the variation of stirrups' amplitudes along all channels.

$$amp = a(y - b)^2 + c \tag{5-3}$$

Coefficients a and c are defined to generate the quadratic profile so that coefficient c represents the maximum amplitude and coefficient b identifies the y coordinate of the center of the

stirrup. Then, the *b*=0 states that the stirrup is symmetrically located in the sample. Additionally, the interference of two pulses causes a small difference of amplitude of two stirrups as shown in Figure 5-19(a) by red and blue curves. On the contrary, the duration of signals does not vary significantly along channels. As illustrated in Figure 5-19(b) by red and blue curves, the duration of stirrups was identified as 4.7 inches on average.

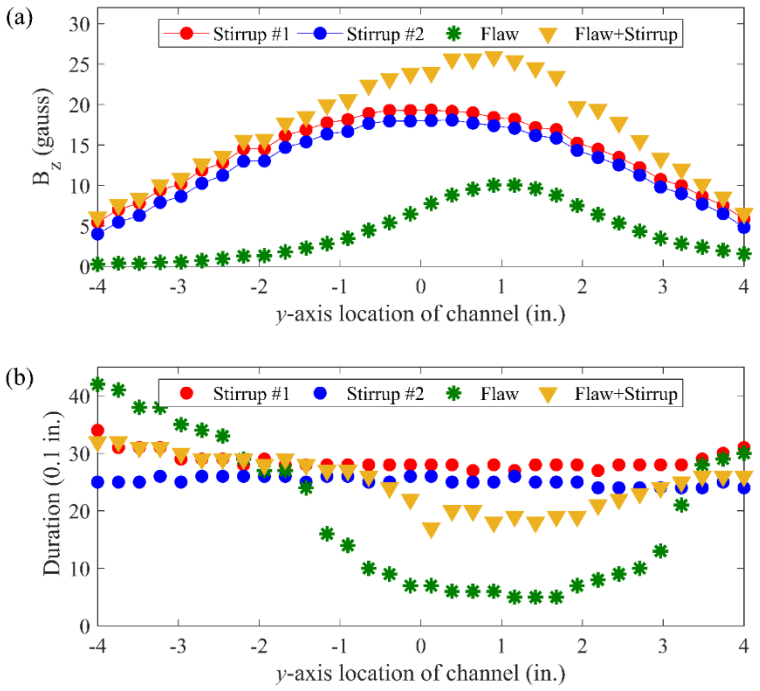

Figure 5-19: The profile of variation of (a) signals amplitudes and (b) durations along the axis of stirrups

A statistical investigation of regression coefficients of equation (5-3) was done through the analysis of multiple tests with the same stirrups. The resulting coefficients *a*, *b*, and *c* from tests were drawn and fitted by the normal distribution shown in Figure 5-20. The coefficient *a* showed a mean value of -0.79, illustrating the downward curvature of the quadratic profile. Coefficient *b* presented a mean value of zero, demonstrating that the stirrups were located symmetrically on the sample. Finally, the coefficient *c* represents the maximum amplitude measured by sensors, which occurs at the position corresponding to *y*=*b* in Equation (5-3).

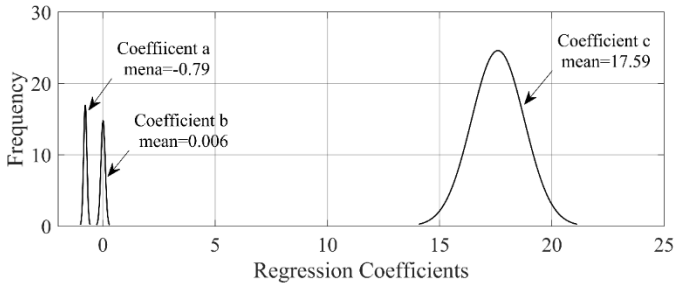

Figure 5-20: fitted normal distribution for regression coefficients of *a*, *b*, and *c* for the cases with two stirrups

The next case of investigation contains six strands and a flaw of 7.14% (corresponding to the cutting of three wires in the length of 1/3 inch) with an embedment length of 2.25 inches, located on the third strand from the top (represented in Figure 5-17). The correlation analysis was implemented in the tests' signals such that the high-correlated points were shown in Figure 5-21(a) by black dots. Opposite to Figure 5-19(a), high correlation values were not detected for all channels such that sensors on channels 8-32 sensed the flaw. Tests signals (Figure 5-21(b)) and a contour plot (Figure 5-21(c)) confirmed that the effect of a flaw on the variation of B_z is a local effect that could not be extended to all channels.

Considering the local effect of a flaw on the magnetic field, the equation (5-4) indicates the regression equation to model the variation of amplitudes by the effect of a flaw. The profile of variation of amplitudes and duration for a flaw were shown in Figure 5-19. The profile of variation of amplitudes is estimated by the following exponential equation:

$$amp = a.e^{\left[-\left(\frac{y-b}{c}\right)^2\right]} \tag{5-4}$$

where the a, b, and c represent the maximum amplitude, the *y*-axis position, and a length-related index of a flaw, respectively.

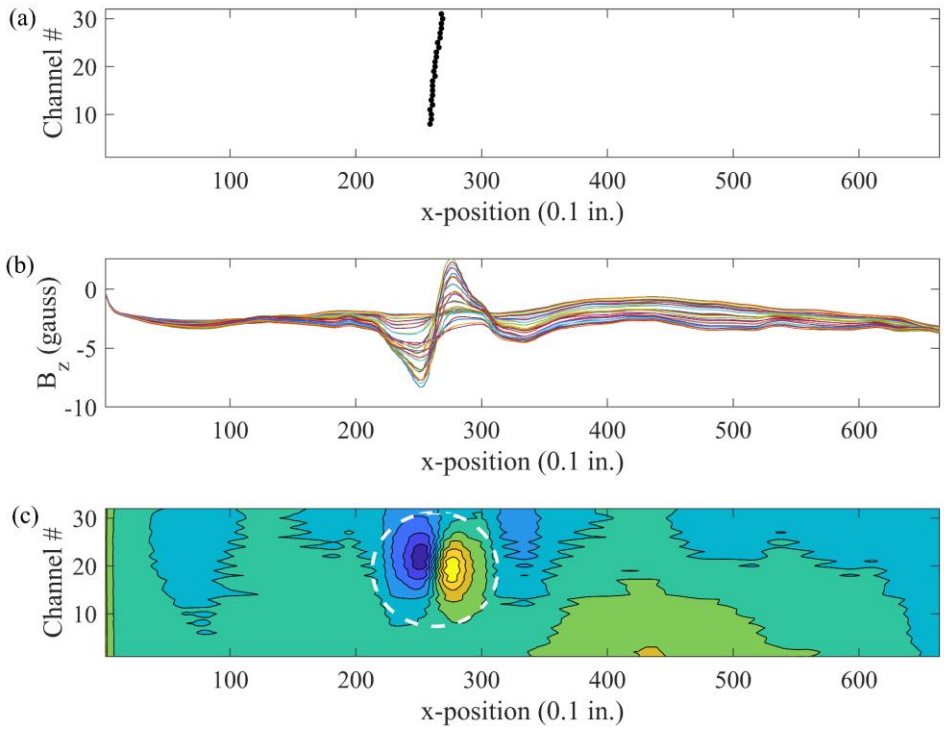

Figure 5-21: correlation analysis result for the case with no stirrup and a flaw of 7.14% and length of 1/3 inch; (a) correlation analysis result illustrating the position of the flaw, vertical field (B_z) variation for all channels, and (c) contour plot of vertical field (B_z) variation for all channels

Therefore, a smaller value of c leads to a sharper profile for amplitudes' variation and consequently a shorter flaw. For the curve shown in Figure 5-19(a) by green asterisks, the coefficient b is obtained as 1.02 inches, demonstrating that the flaw is located on the third strand. On the contrary with stirrups, the duration values for a flaw (shown by green asterisks in Figure 5-19(b)) are significantly varied per channel such that a quadratic variation of durations is observed with a minimum value at $y = b$.

The dashed ellipse in Figure 5-21-c highlighted the region where the flaw affects the vertical magnetic field. It is illustrated that a flaw with 7.14% of section loss and 1/3-inch-long affects the magnetic field in an elliptic area such that its diameters are approximately 10 and 6 inches in x and y directions, respectively. The effective region for flaws changes by its intensity and length.

Conveniently, the stirrups' diameter does not change any more along with the prestressed members, which leads to having the same regression coefficients of equation (5-3) for all stirrups. Therefore, any 3-D variation of the magnetic field, which does not follow the equation (5-3), would address an abrupt volumetric change of steel except stirrups. Therefore, given the diameter of stirrups, properties of the induced magnetic field (and as-built structural drawings in an ideal situation), the 3-D profiles of variation of amplitudes and durations for stirrups can be generated.

Expectedly, the intensity and length of a corroded region may change by many factors such as the severity of the invasive environment or length of cracks in the concrete. Therefore, the corrosion-related flaws are intrinsically unpredictable so that it is not possible to regulate the regression coefficients of equation (5-4).

As demonstrated by experiments and simulations, the MFL associated with different volumetric changes of ferrous materials are superimposed on each other (Elyasigorji, Rezaee, & Ghorbanpoor, 2020). The orange triangular marker plot in Figure 5-19(a) is for a test configuration in which the stirrups and a flaw of 7.14% are at the same position and the superimposition of effects is validated for variation amplitudes. Then, correlation analysis will remove the effects of stirrups from the experimental signals and the next correlation analysis characterizes the effective regions for other discontinuity of steel along with the prestressed member.

In contrast with the amplitude variation, the variation of durations does not follow the superposition rule perfectly. As shown in Figure 5-19(b), the profile of variation of duration (marked by orange triangles) is laid between cases that contain only stirrups or flaws.

As mentioned earlier (referring to section 4.1), the 3-D analysis enables us to detect the stirrups that were assembled aligned or were deviated due to construction processes. Figure 5-22

illustrates the performance of 3-D analysis for a case with two aligned stirrups #4 with a spacing of 12 inches and an embedment length of 2.25 inches. The arrangement of high-correlated points for stirrups in Figure 5-22(a) confirms the alignment of stirrups where the orientation angle of stirrups can be easily obtained by the slope of a line fitted on black dots in Figure 5-22(a). Moreover, the deviation of stirrups is visible in the contour plot shown in Figure 5-22(b). The amplitudes of signals at locations of stirrups showed almost the same variations, which was expected (Figure 5-22(c)).

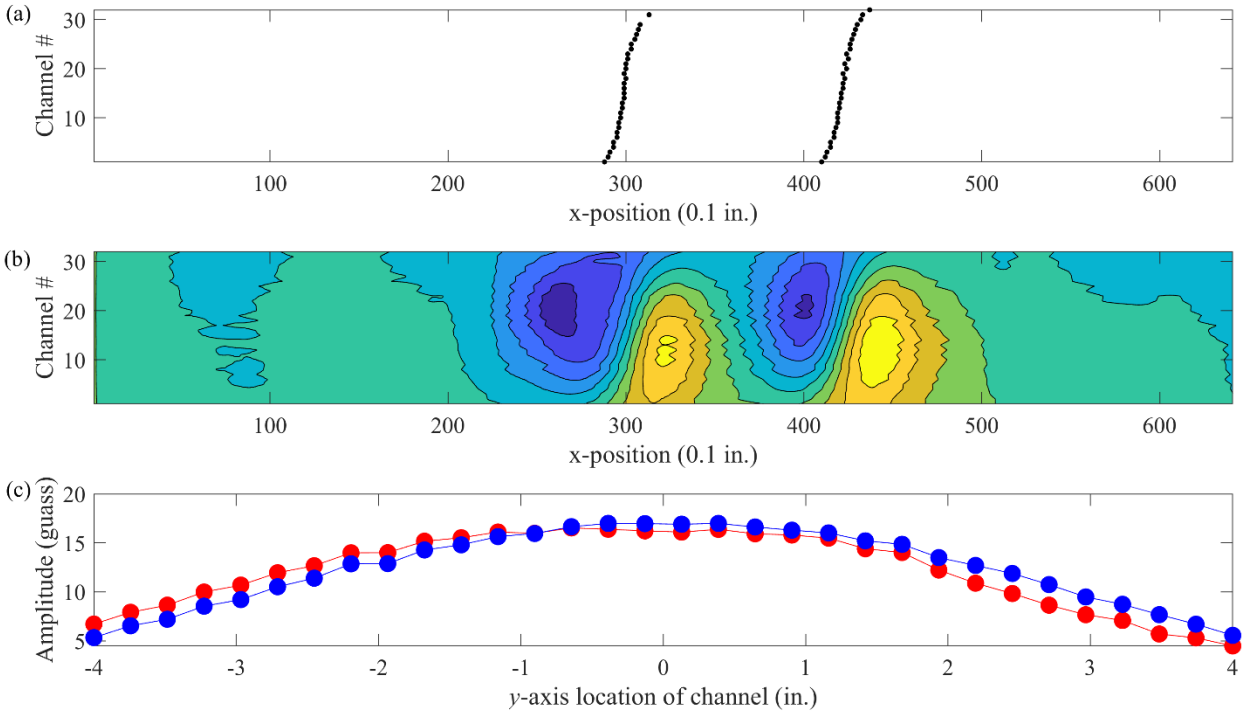

Figure 5-22: 3-D analysis of MFL signal for a case with aligned stirrups

The main responsibility of the 3-D analysis is identification of stirrups' configuration that is crucial for the flaw characterization step. In the following, three test cases are assessed to show how the 3-D analysis helps to determine the locations of stirrups and flaws (if it is possible). The test cases are referred to stirrups #4 with spacing of 12 inches and an orientation angle of 90 degrees, and a flaw of 7.14% with an embedment depth of 2.25 inches. The positions of the flaw

are at the first stirrups' location, 3 inches from the first stirrup, and mid-point of two stirrups, respectively. The correlation analysis in 3-D analysis apparently illustrates the presence of two stirrups spaced by 12 inches for all three cases, as shown in Figure 5-23.

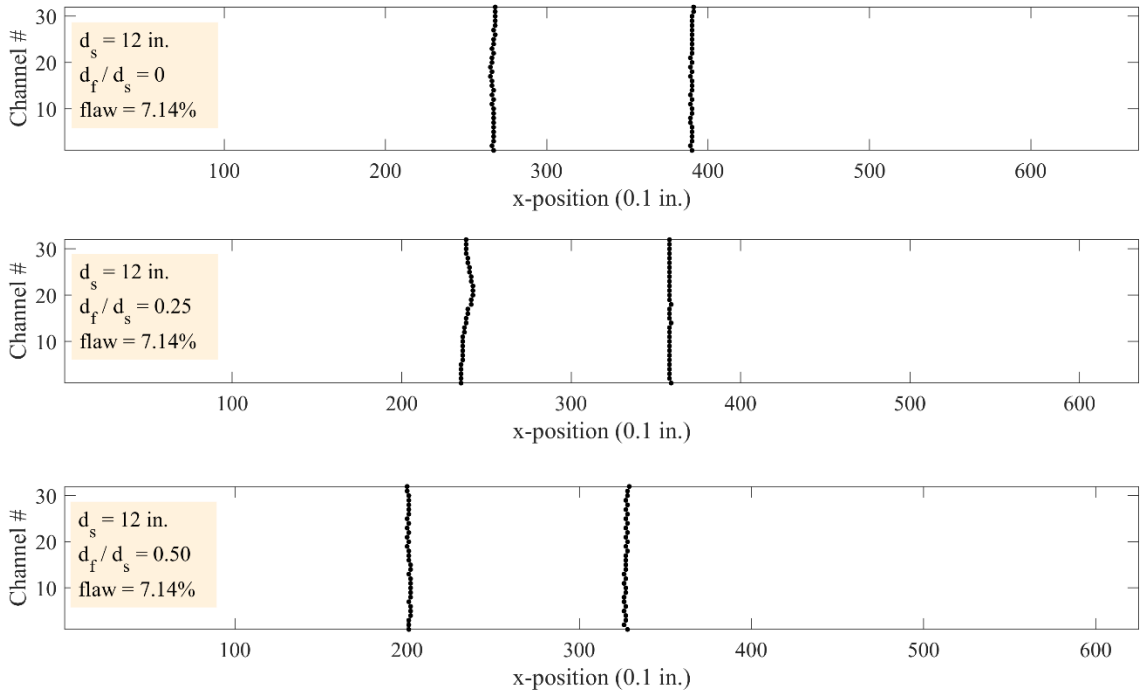

Figure 5-23: correlation analysis results comparison for three experiments

The 3-D analysis provides qualitative and quantitative ways to be informed about the configuration of stirrups and flaws. The first option is looking over the contour plots of MFL signals, which helps to assess the MFL sources qualitatively.

As shown in Figure 5-24, there is evidence in contour plots about stirrups and flaws. For all plots, the presence of two stirrups with spacing of 12 inches is apparent. In the top plot where the flaw is located at the first stirrup location, it is not easy to detect the flaw position although the contours at the first stirrup were shrunk a bit in comparison with the second stirrup. For the second case, the middle plot, the contours are skewed for the first stirrup, demonstrating the presence of

another MFL source. The bottom plot shows a clear disturbance of contours between two stirrups, which refers to a flaw at mid-point of two stirrups.

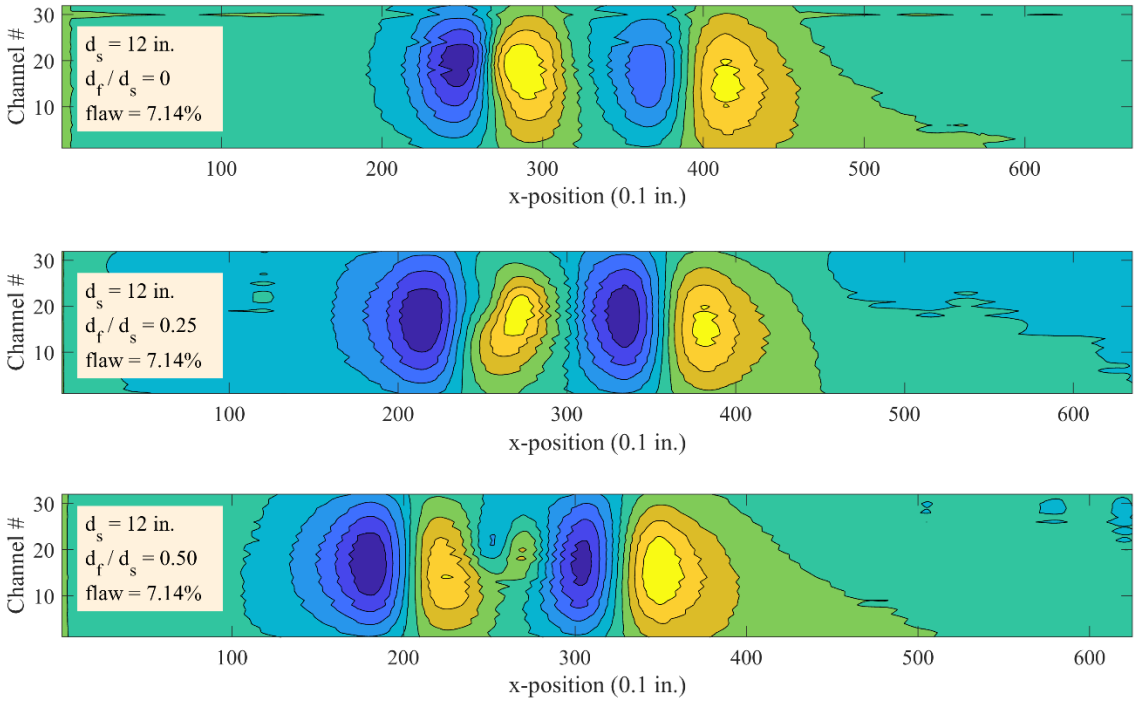

Figure 5-24: contour plots comparison for three experiments

Another way of assessment is using the amplitudes and duration analysis provided by 3-D analysis. The evaluation of the variation of amplitudes and durations is informative to diagnose possible flaws for each experiment both qualitatively and quantitatively. The amplitude analysis (referring to Figure 4-1(g) in section 4.1) of the first case is shown in Figure 5-25 that demonstrates the presence of a flaw close to the first stirrup through an apparent difference of variations of amplitudes and durations in comparison with the second stirrup. The flaw's approximate position is obtained in y~1 inch, which is corresponding to channel #20.

The amplitude analysis (referring to Figure 4-1(g) in section 4.1) of the second case is shown in Figure 5-26 that demonstrates the presence of a flaw close to the first stirrup through a slight difference in variations of amplitudes but noticeable difference of durations in comparison

with the second flaw. The flaw's approximate position is obtained in *y*~0.9 inch, which is corresponding to channel #19.

The amplitude analysis (referring Figure 4-1(g) in section 4.1) of the third case is shown in Figure 5-27. It is not easy to diagnose the flaw by looking into the variation of amplitudes and duration since they showed same variations; however, the magnitudes of amplitudes for the second stirrup are slightly higher than for the first stirrup. As mentioned above, these differences are not easy to analyze. For such a complicated case, the contour plots help to detect the area of potential flaws. Moreover, even for this complicated case, the 3-D analysis will identify the positions of stirrups, which is its main responsibility for the next steps of signal analysis (i.e., 2-D analysis as discussed later in this chapter).

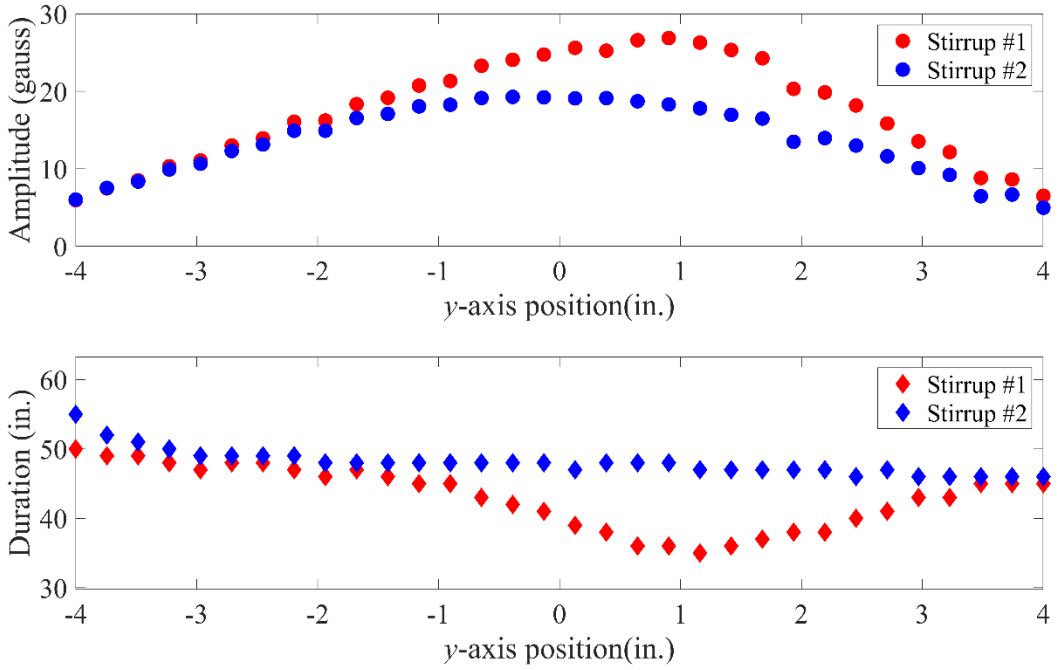

Figure 5-25: amplitudes and durations analysis for the case with two stirrups spaced by 12 inches and a flaw of 7.14% located at the first stirrup's position

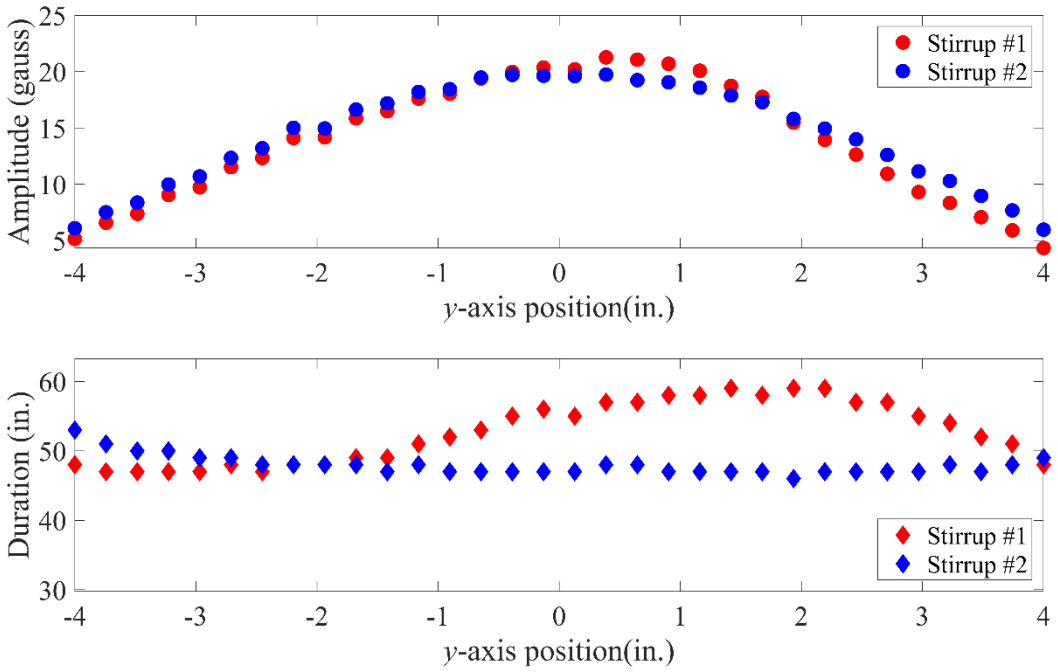

Figure 5-26: amplitudes and durations analysis for the case with two stirrups spaced by 12 inches and a flaw of 7.14% located at 3 inches from the first stirrup's position

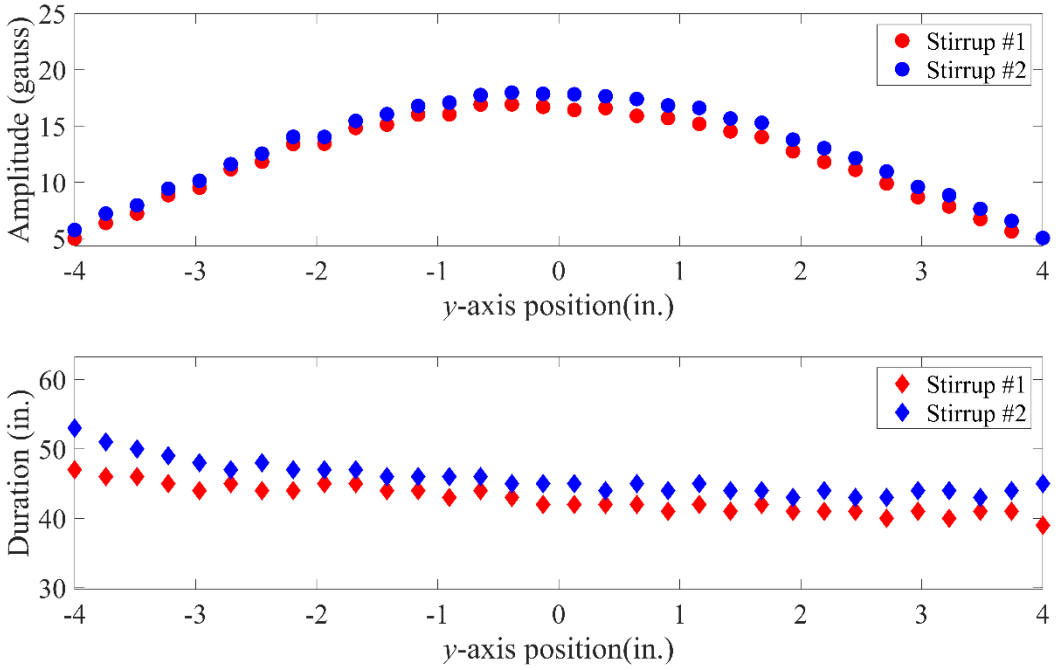

Figure 5-27: amplitudes and durations analysis for the case with two stirrups spaced by 12 inches and a flaw of 7.14% located at mid-point of two stirrups

In conclusion, the 3-D analysis of MFL signals provides information about the configuration of test specimen as follows:

- The pattern of stirrups' spacing is identified.
- The orientation angle of stirrups is determined.
- The exact position of the flaw is obtained.

5.7 2-D correlation analysis to detect flaws

The 2-D correlation analysis is performed on a signal by the following steps:

1. Creation of an artificial signal including the effects only of stirrups.
2. Removing the stirrups' pulses from the test signal.
3. Identifying the amplitude and duration of flaws detected by the 3-D analysis.

As discussed earlier, after filtering noises and stirrups' pulses from the test signal, another correlation analysis could be done to characterize the flaws or other discontinuities that were detected by 3-D analysis. The correlation analysis in this part may be done using a reference signal. Because of the non-specified geometry of flaws, in comparison with a correlation analysis done for stirrups, a lower threshold for a correlation value of 0.5 is selected for the correlation analysis.

The next step is the calculation of amplitude and duration values for detected flaws. The amplitude and duration values could be calculated easily by finding peak values in the vicinity of the detected flaw.

As an example, a case by the following configuration is analyzed to find the location of the flaw that belongs to category 4 (defined in section 4.6):

- Six strands, each with a diameter of 0.5 inch

- Two stirrups of #4 spaced at 16 inches
- A flaw of 16.67% section loss with a cut length of 1/3 of an inch and, an embedment length of 2.25 inches.

The output from the code in Figure 5-28 shows the location of the flaw and its distance from the start point of the data reading. A flaw with the amplitude of 29.922 Gauss was detected at the location of the first stirrup with a duration of 2.58 in. that is corresponding to a flaw with 16.67% section loss with 1/3-inch length as reported in Table 5-2.

The test's signal is shown in Figure 5-29(a) and the artificial signal, which is generated by the analytical method, is shown in Figure 5-29(b). The signal in Figure 5-29(c) shows the filtered signal that was identified after subtracting the artificial signal from the test signal. The correlation analysis gave the position and amplitude of the flaw at the position 26.40 inches. The results illustrated the ability of 2-D analysis to detect the flaw for the case with two stirrups and one flaw, which was located at the same position as the first stirrups (Elyasigorji et al., 2020).

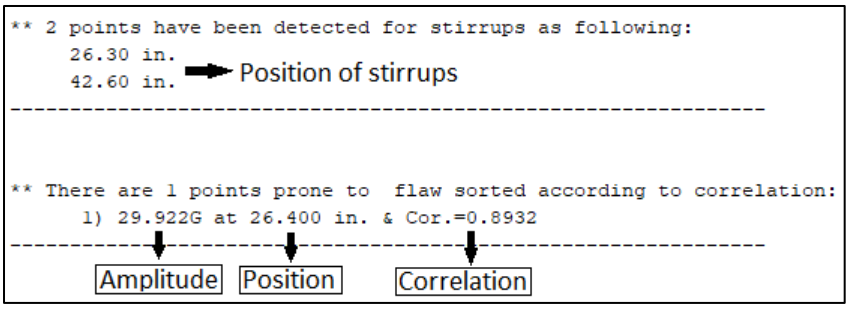

Figure 5-28: Result from MATLAB

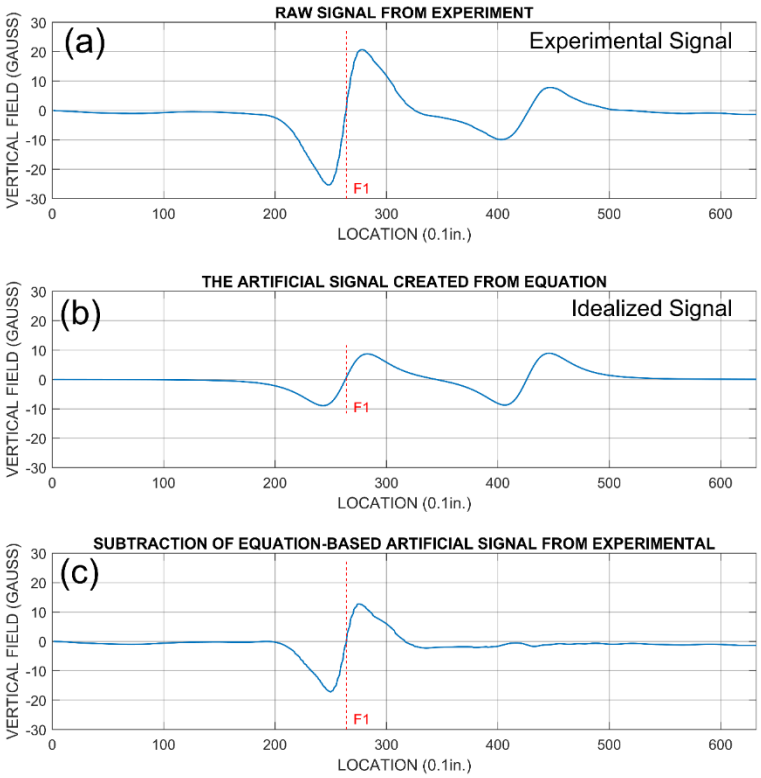

Figure 5-29 a, b, & c: Sample Diagrams for Flaw Detection Process

Occasionally, complex cases are expected in real tests such as variable geometrical properties of the flaw, non-uniform stirrup spacing, different orientation angles of stirrups, and other sources of signal perturbations. These complexities are discussed in the following. Based on the experiments, by varying the percentage and length of flaws, the resulting signal amplitude and duration values can change significantly. Considering this approach, various parameters in the correlation analysis equation, equations 5-1 and 5-2, can be established for different conditions to arrive at a precise flaw location. This will require additional work to be performed in this study.

5.8 Individual effects of flaw on the MFL

To estimate the section loss percentage and length associated with a flaw, it is necessary to have information about the individual effects of flaws on the MFL. Gathering data from the experiments and simulations, the following data were given in Table 5-2 to Table 5-5.

Table 5-2: The individual effects of flaw with several section loss percentages and lengths on the MFL when the clear space of magnet and flaw is 2.25 inches.

Depth = 2.25 in.		flaw length: 1/3 in.		flaw length: 2/3 in.		flaw length: 1.0 in.	
Section loss (%)	# of cut wires	Amplitude (gauss)	Duration (in.)	Amplitude (gauss)	Duration (in.)	Amplitude (gauss)	Duration (in.)
2.38	1	4.96		5.00		5.10	
4.76	2	6.89		8.76		10.64	
7.14	3	10.44		15.14		18.82	
9.52	4	16.33	2.60	23.87	2.80	28.22	3.00
11.90	5	20.41		31.08		36.51	
14.29	6	24.49		38.29		44.80	
16.67	7	28.59		46.17		53.66	

Table 5-3: The individual effects of flaw with several section loss percentages and lengths on the MFL when the clear space of magnet and flaw is 3.0 inches.

Depth = 3.0 in.		flaw length: 1/3 in.		flaw length: 2/3 in.		flaw length: 1.0 in.	
Section loss (%)	# of cut wires	Amplitude (gauss)	Duration (in.)	Amplitude (gauss)	Duration (in.)	Amplitude (gauss)	Duration (in.)
2.38	1	3.472		3.5		3.57	
4.76	2	4.4785		5.694		6.916	
7.14	3	6.786		9.841		12.233	
9.52	4	10.6145	1.69	15.5155	1.82	18.343	1.95
11.90	5	13.2665		20.202		23.7315	
14.29	6	15.9185		24.8885		29.12	
16.67	7	18.5835		30.0105		34.879	

Table 5-4: The individual effects of flaw with several section loss percentages and lengths on the MFL when the clear space of magnet and flaw is 3.0 inches.

Depth = 4.0 in.		flaw length: 1/3 in.		flaw length: 2/3 in.		flaw length: 1.0 in.	
Section loss (%)	# of cut wires	Amplitude (gauss)	Duration (in.)	Amplitude (gauss)	Duration (in.)	Amplitude (gauss)	Duration (in.)
2.38	1	2.3808		2.4		2.448	
4.76	2	2.65265		3.3726		4.0964	
7.14	3	4.0194		5.8289		7.2457	
9.52	4	6.28705	1.00	9.18995	1.08	10.8647	1.16
11.90	5	7.85785		11.9658		14.05635	
14.29	6	9.42865		14.74165		17.248	
16.67	7	11.00715		17.77545		20.6591	

Table 5-5: The individual effects of flaw with several section loss percentages and lengths on the MFL when the clear space of magnet and flaw is 6.0 inches.

Depth = 6.0 in.		flaw length: 1/3 in.		flaw length: 2/3 in.		flaw length: 1.0 in.	
Section loss (%)	# of cut wires	Amplitude (gauss)	Duration (in.)	Amplitude (gauss)	Duration (in.)	Amplitude (gauss)	Duration (in.)
2.38	1	1.0416		1.05		1.071	
4.76	2	1.04039		1.32276		1.60664	
7.14	3	1.57644		2.28614		2.84182	
9.52	4	2.46583	0.39	3.60437	0.42	4.26122	0.45
11.90	5	3.08191		4.69308		5.51301	
14.29	6	3.69799		5.78179		6.7648	
16.67	7	4.31709		6.97167		8.10266	

These tables were prepared for several depths of magnets, which is defined as the clear distance of magnet and strands. Conveniently, a reinforced concrete girder may have tension strands (or rebar) in multiple levels. Therefore, the clear distance of any possible flaw on the strands is defined as the depth (or embedment depth) of each layer of rebar.

The above tables are informative after conducting the 2-D correlation analysis where the amplitude and duration of the detected flaw are given. Then, finding the pair of amplitude and duration will lead to estimate the flaw's properties from Table 5-2. To provide graphical representation of the above tables, Figure 5-30, Figure 5-31, and Figure 5-32 visualize the results based on the flaw's length.

Obviously, the volume of the flaw is an important factor in the magnitude of amplitude while it does not affect the duration of the pulses. Therefore, results listed in the above tables were converted to the volumetric information of flaws and drawn in Figure 5-33. It is demonstrated that the amplitude of the MFL signal changes with a roughly linear trend versus the volume of the flaw. This plots were drawn in a semi-log scale for multiple depths to be more informative in estimation of the flaw.

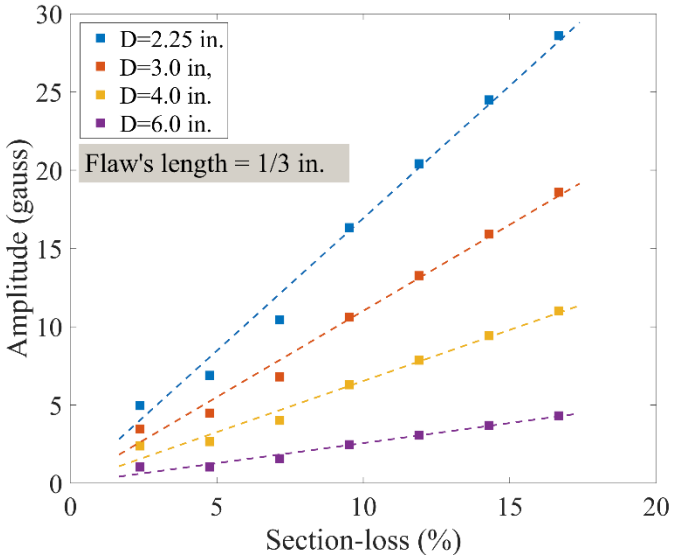

Figure 5-30: variation of amplitudes versus flaws' percentages and depth of magnet for flaws with a length of 1/3 in.

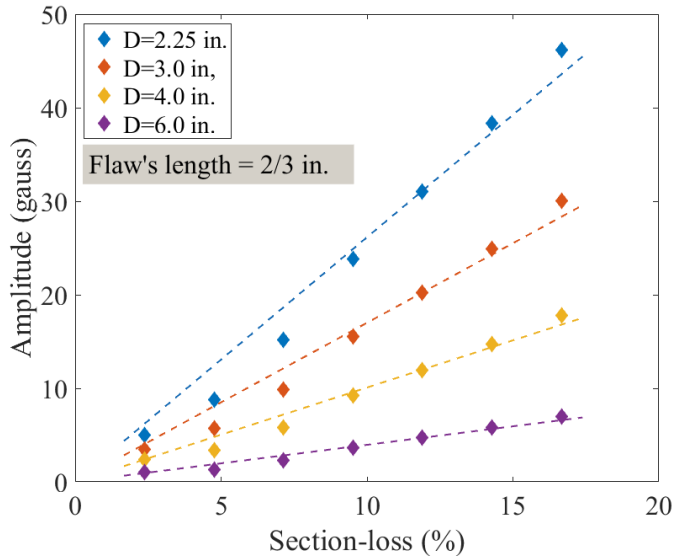

Figure 5-31: variation of amplitudes versus flaws' percentages and depth of magnet for flaws with a length of 2/3 in.

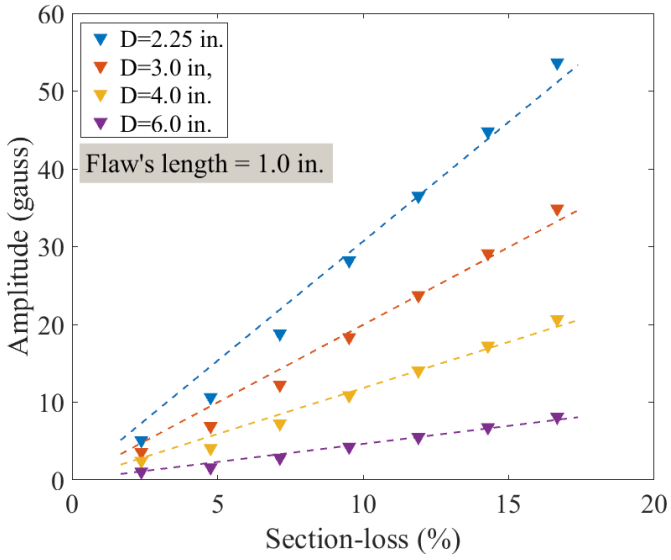

Figure 5-32: variation of amplitudes versus flaws' percentages and depth of magnet for flaws with a length of 1.0 in.

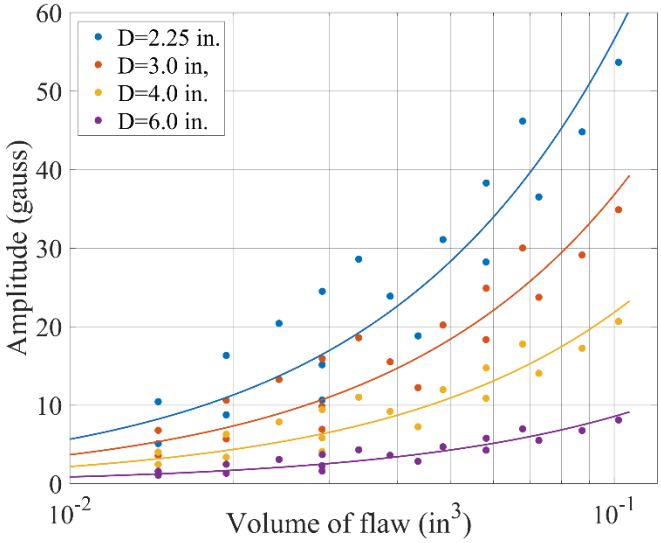

Figure 5-33: Volumetric effects of flaw on the magnitude of amplitude of MFL

5.9 Flaw characterization

Based on the discussion provided in this chapter, a flaw would be characterized through the following steps:

- Clean up noises and spikes from the MFL signal
- Detect stirrups' locations through the 3-D analysis

- Identify locations of the flaws from the 3-D analysis
- Characterize flaws' properties by 2-D analysis and estimate flaw's properties using Table 5-2 to Table 5-5.

Although the flaw is found from the steps explained above, the analytical method provides an alternative way to confirm the findings of 3-D and 2-D analyses.

The presence of a flaw changes the amplitudes of MFL pulses at the position of the stirrups. Then, tracking the relative variation of the stirrups' amplitudes can be used as a tool to estimate the position of the flaw, which is utilized as a confirmation step for the 3-D analysis. The relative variation of amplitudes is defined as the ratio of the actual amplitude of a stirrup over the average amplitude of a stirrup (without a flaw's effect) and is called *Relative Amplitude* (*RA*). To present the relative amplitude graphically, it was calculated for a combination of several factors as listed below:

- 6 strands with an overall diameter of ½ inch and stirrups #4 are used.
- Multiple flaws were examined corresponding to the cutting of 1, 2, …, 7 wires that are equivalent to section loss of 2.38, 4.77, 7.14, 9.52, 11.90, 14.28, and 16.67 percent, respectively.
- Several lengths of the flaw were added to the model as 1/3, 2/3, and 1.0 inches to assess the effect of the flaw's length on the MFL signal.
- The relative amplitudes were identified for the relative distance of flaw, D, varying from 0 to 0.50.
- The embedment depth of flaws is 2.25 inches.

The analytical method reports the *RA* of stirrups that are located on two sides of a flaw. From the MFL signal and 3-D analysis, the average magnitude of stirrups' amplitudes is given and performing a comparison of amplitudes identifies the stirrups affected by flaws.

As demonstrated by the analytical method, a flaw of shorter than one inch may affect the MFL signal in the interval between two neighbor stirrups. The (RA_{left}, RA_{right}) pair is defined as *RA* values for stirrups located on the left and right side of a flaw, respectively, which is obtained from the MFL signals. For $RA_{left} > RA_{right}$, the flaw may be closer to the left stirrup and vice versa. For the cases in which two *RA*s are not close numerically, it is easy to estimate the location and percentage of the flaw but, for close *RA* values, the analytical graphs may lead to more than one answer. The good news is that the stirrups' spacing is determined from the 3-D analysis, which plays a significant role in the variation of the *RA* ratio.

For the stirrups' spacing of 16 inches, the variation of *RA* ratios was plotted in Figure 5-34, Figure 5-35, and Figure 5-36 with flaws' lengths of 1/3, 2/3, and 1.0 inches, respectively. Each figure contains two sets of plots so that the left plot shows the *RA* ratio for the stirrup located on the left side of the flaw and the right plot indicates the variation *RA* ratio for the stirrup on the right side of the flaw. The *RA* ratios were reported based on D values from 0 to 0.5 and, for the values of D between 0.5 and 1.0, it is necessary to swap two plots. It means that for $0.5 < D < 1.0$, the left plot will show the *RA* ratios for the right stirrup and vice versa.

The variation of *RA* for the left stirrup has shown a significant difference for multiple flaws up to D=0.25 such that beyond this point, it is not easy to distinguish between flaws' plots. Moreover, beyond D=0.25, the *RA* ratios for the right stirrup look more distinguishing for multiple

flaws. Considering spacing of 16 inches and a short flaw, the *RA* ratios for the right stirrup in Figure 5-34 have shown a small reduction of less than 7 percent.

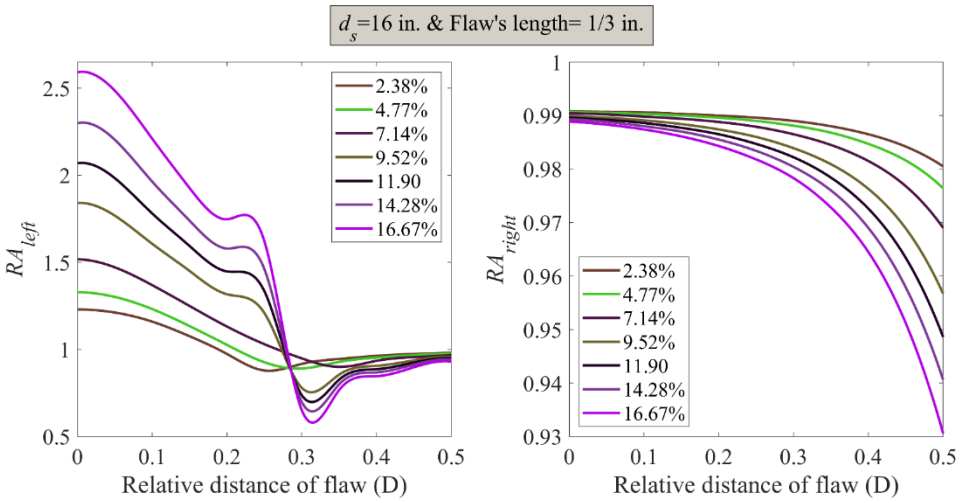

Figure 5-34: Relative amplitudes for a flaw of 1/3 of an inch and stirrups' spacing of 16 inches

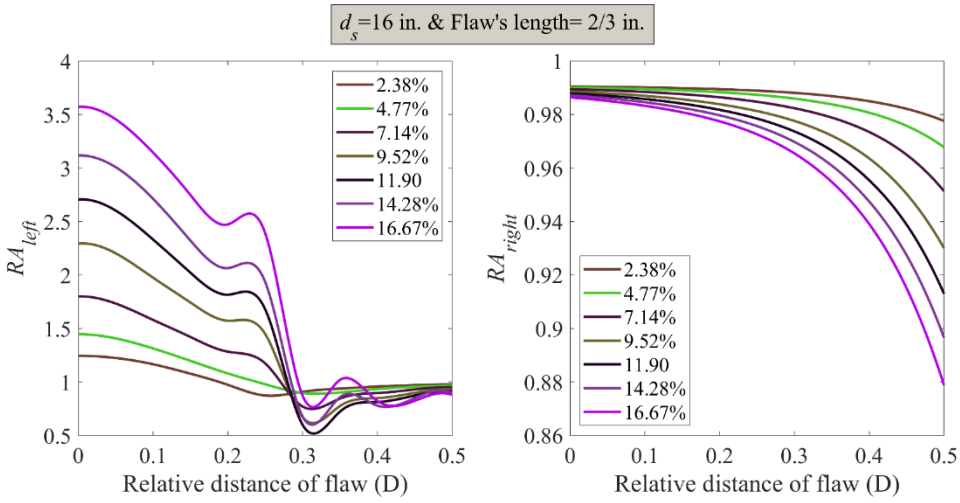

Figure 5-35: Relative amplitudes for a flaw of 2/3 of an inch and stirrups' spacing of 16 inches

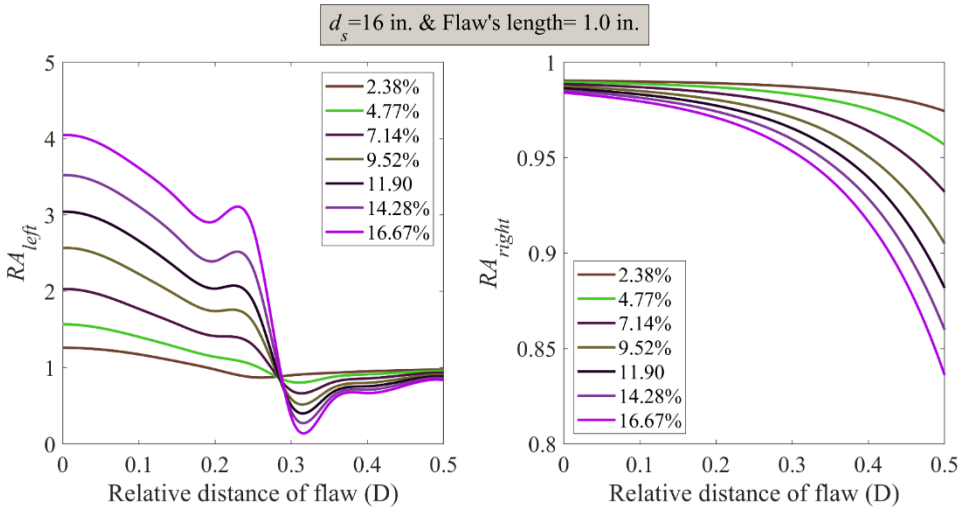

Figure 5-36: Relative amplitudes for a flaw of 1.0 of an inch and stirrups' spacing of 16 inches

For closer stirrups, the variation of *RA* ratio shows more sensitivity to the percentage of the flaw since the interference of pulses of the flaw and stirrups is more noticeable especially for longer flaws. For the stirrups' spacing of 12 inches shown in Figure 5-37, Figure 5-38, and Figure 5-39, considering the left stirrup, the variation of *RA* values is distinguishing versus different flaws for D<0.30. Moreover, the variation of *RA* ratios for the right stirrup could reach out to 20%, 30%, and 40% for the flaw's length of 1/3, 2/3, and 1.0 inch, respectively.

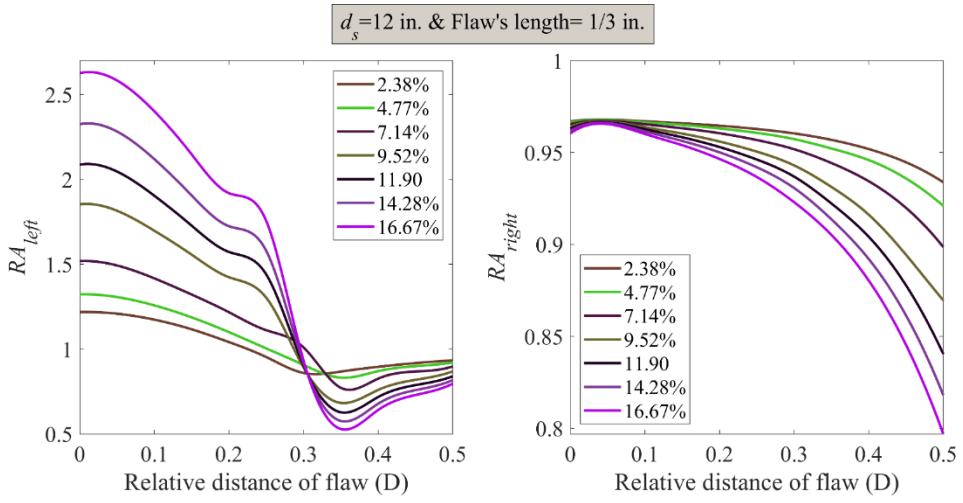

Figure 5-37: Relative amplitudes for a flaw of 1/3 of an inch and stirrups' spacing of 12 inches

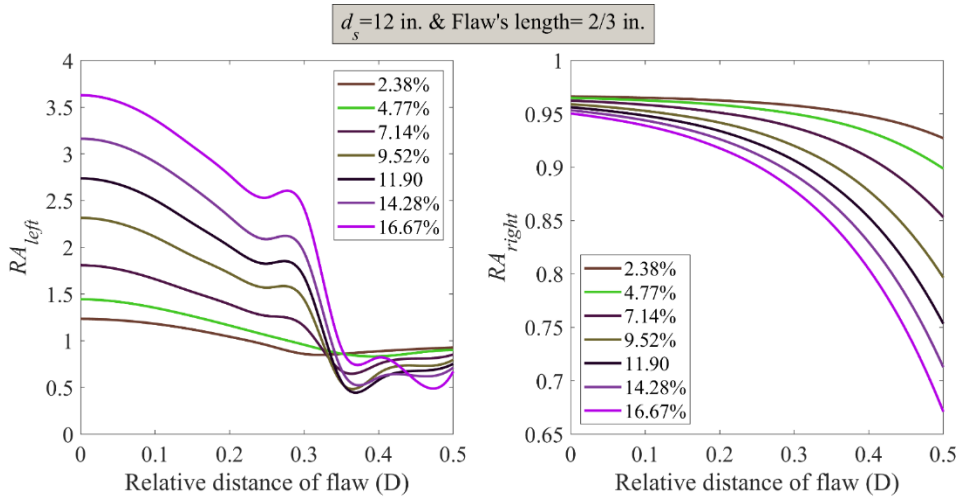

Figure 5-38: Relative amplitudes for a flaw of 2/3 of an inch and stirrups' spacing of 12 inches

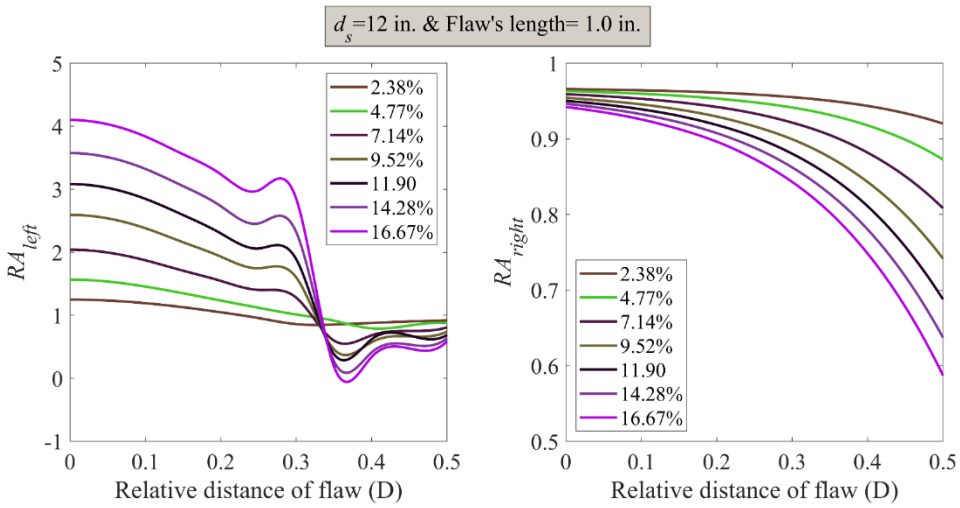

Figure 5-39: Relative amplitudes for a flaw of 1.0 of an inch and stirrups' spacing of 12 inches

The variation of *RA* ratio is presented for stirrups with a distance of 8 inches in Figure 5-40, Figure 5-41, and Figure 5-42. Since the stirrups' spacing is relatively short, more dominant signal interference is anticipated in presence of a flaw. For the left stirrup, the variation of *RA* values is distinguishing versus different flaws for D<0.40. Moreover, the variation of *RA* ratios for the right stirrup could reach out to 60%, 80%, and 90% for the flaw's length of 1/3, 2/3, and 1.0 inch, respectively.

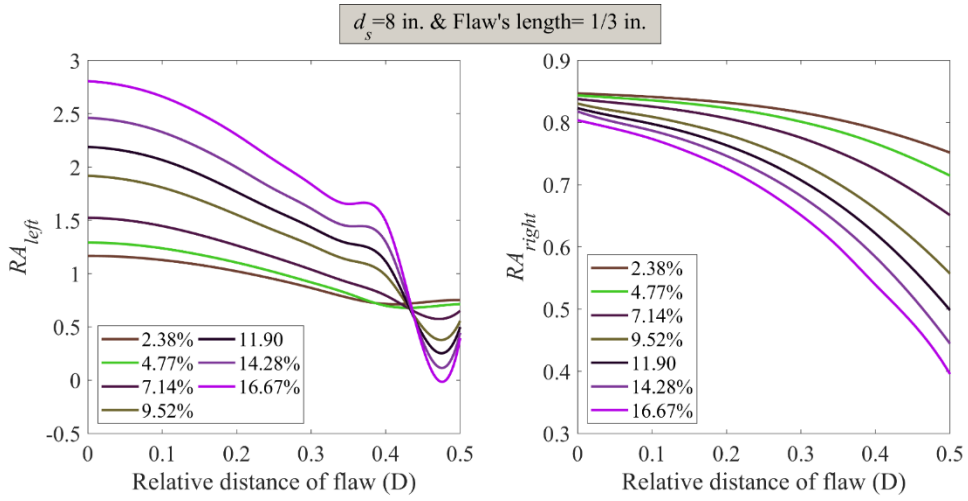

Figure 5-40: Relative amplitudes for a flaw of 1/3 of an inch and stirrups' spacing of 8 inches

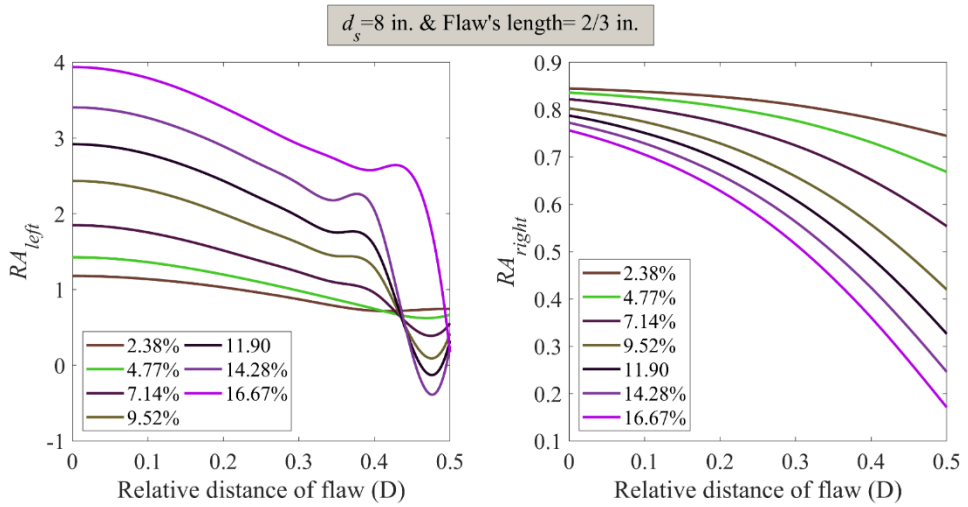

Figure 5-41: Relative amplitudes for a flaw of 2/3 of an inch and stirrups' spacing of 8 inches

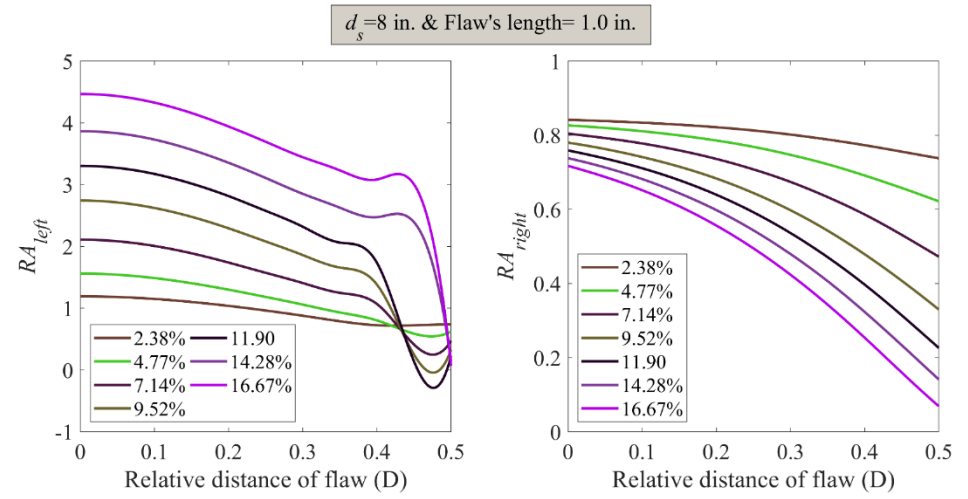

Figure 5-42: Relative amplitudes for a flaw of 1.0 of an inch and stirrups' spacing of 8 inches

Considering the plots from the analytical method, the following highlights can be obtained for the variation of stirrups' amplitudes by effects of a flaw:

- The stirrups' spacing strongly dominates the variation *RA* ratio such that a bigger spacing leads to smaller variations of the right stirrup's amplitude and vice versa.
- The length and percentage of the flaw is another significant factor in the *RA* ratio. A bigger length or percentage causes bigger variations of stirrups' amplitudes.
- In samples with bigger stirrups' spacing, the analysis of amplitudes of stirrups has fewer difficulties because the right stirrup shows a small range of variation of amplitude.

In conclusion, the analytical method can be used as a tool to provide an estimation about the possible flaw that is located between two stirrups. The estimation can be done by measuring the *RA* ratios for all stirrups in the sample. Then, stirrups with significantly different *RA* ratios are expected to be close to a flaw. The estimation of the flaw's percentage and length would be obtained from the plots provided above while the stirrups' spacing is given from the 3-D analysis.

5.10 Case studies

In this section, two examples are analyzed to localize the flaw and estimate its properties. From the experimental data, it is known that the embedment depth of strands is 2.25 inches. The result of 3-D analysis of a MFL signal (the **first example)** is shown in Figure 5-43 in which the detected point for stirrups (Figure 5-43(a)) demonstrates that two stirrups are located with a distance of 12 inches and an orientation angle of 90 degrees. The irregularity of the MFL contour as marked by a dashed ellipse in Figure 5-43(b) illustrates the presence of another source of MFL, which is a flaw. It is confirmed by amplitude analysis (referring to Figure 4-1(g) in section 4.1)

through a local reduction of amplitudes of the first stirrup in Figure 5-43(c), which is shown by blue dots. The reduction of magnitude has an extremum on y=0.64 inch, which is corresponding to the third strand and channel #19.

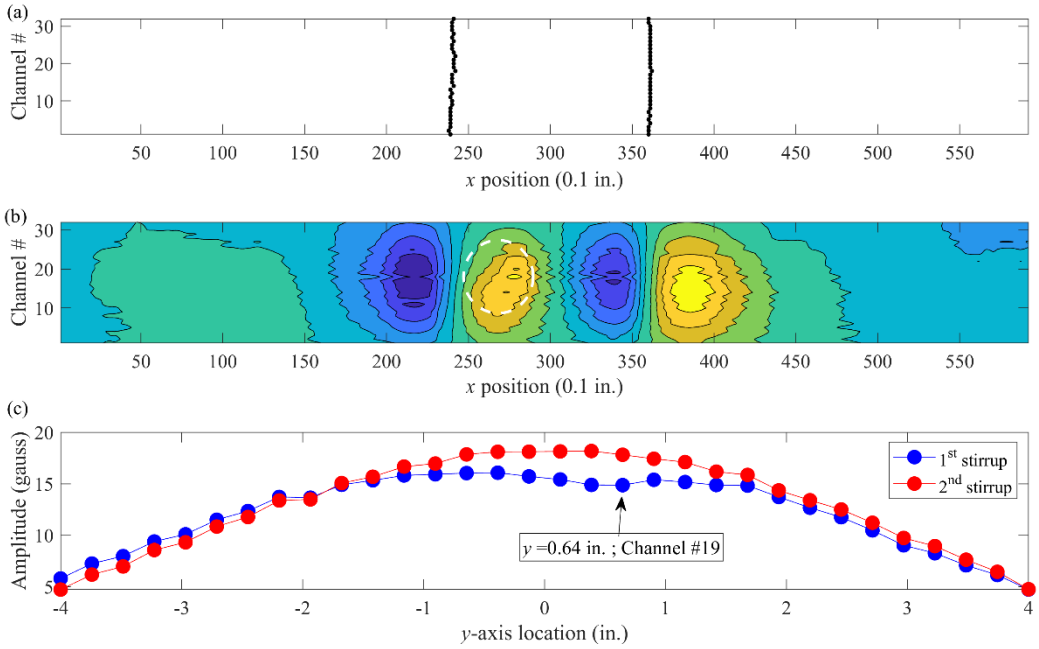

Figure 5-43: the 3-D analysis of the first example

The next step is conducting the 2-D analysis of the MFL signal for channel #19, which was detected as the channel closest to the flaw's center. The MFL signal for channel #19 is shown in Figure 5-44(a). It is not easy to locate the flaw observationally. Considering the spacing of the stirrups of 12 inches, an artificial signal was built up using the analytical method and shown in Figure 5-44(b). The filtered signal was obtained after subtracting the artificial signal from the experimental signal and was shown in Figure 5-44(c). The filtered signal has shown a residual pulse with an amplitude of about 11 gausses and a duration of 2.6 inches.

Referring to Table 5-2, a flaw of range of *7-9 percentage of section loss* is expected with a *length of about 1/3 of an inch*. Moreover, the flaw is located at a distance of about 3 inches from the first stirrup and between two stirrups. From Figure 5-33, it is anticipated to have a flaw with

an overall volume of 6×10^{-4} in^3, which is corresponding to a third of an inch long flaw with about 7% section loss.

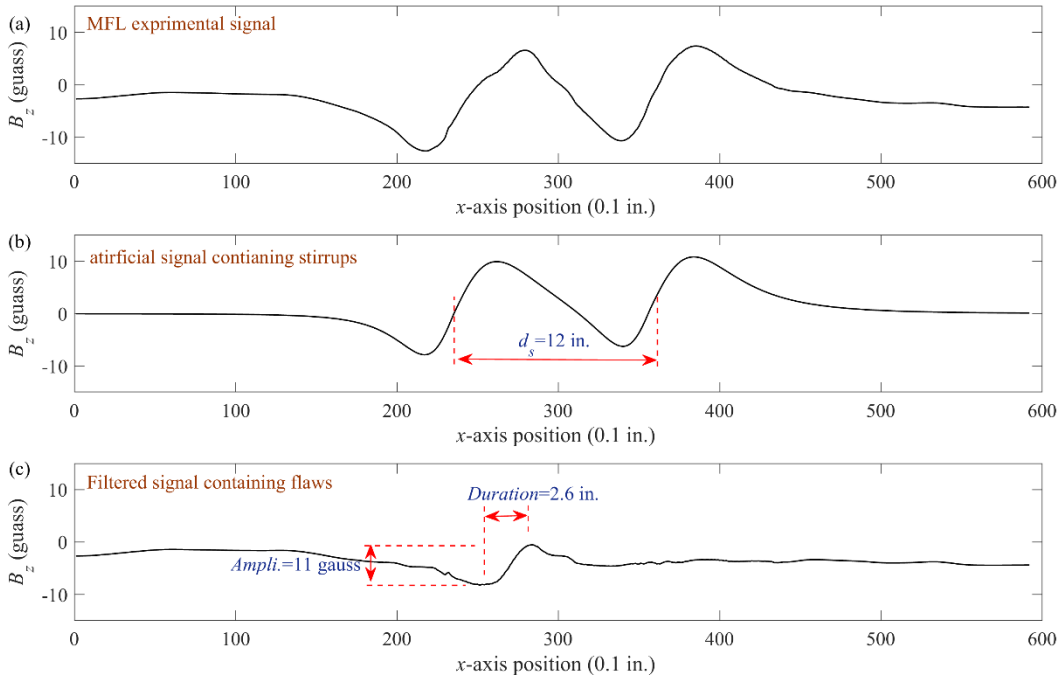

Figure 5-44: 2-D analysis of MFL for channel #19 for example 1

The result of 3-D analysis of another MFL signal (the **second example)** is shown in Figure 5-45 in which the detected point for stirrups (Figure 5-45(a)) demonstrates that two stirrups are located with a distance of 16 inches and an approximate orientation angle of 90 degrees. From the experimental data, it is known that the embedment depth of strands is 2.25 inches. A more in-depth look at Figure 5-45(a) reveals that the first stirrup has deviated slightly during the test, which demonstrates the usefulness of 3-D analysis for detection alignment of stirrups. The irregularity of MFL signals and contours as marked by a dashed ellipse illustrates the presence of another source of MFL, which is a flaw. Similar to the first example, the amplitude of the second stirrup is reduced so that it has an extremum on y=0.64 in, which is corresponding to the third strand and channel #19.

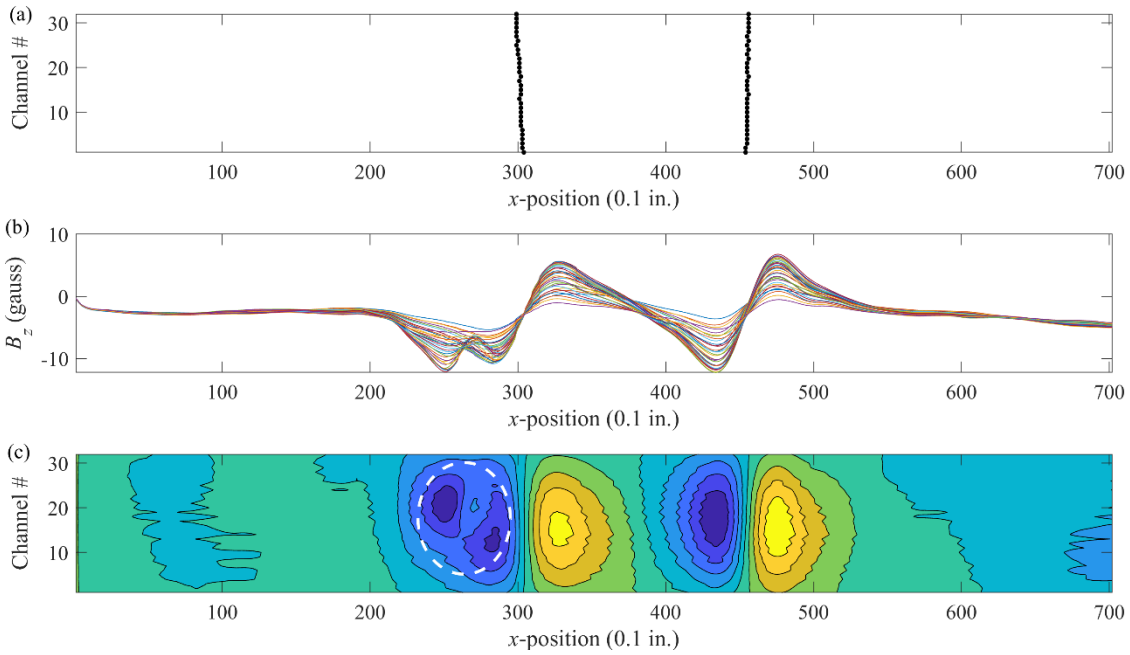

Figure 5-45: the 3-D analysis of the second example

The next step is conducting the 2-D analysis of the MFL signal for channel #19, which was detected as the channel closest to the flaw's center. The MFL signal for channel #19 is shown in Figure 5-46(a). Considering the spacing of the stirrups of 16 inches, an artificial signal was built up using the analytical method and shown in Figure 5-44(b). The filtered signal was obtained after subtracting the artificial signal from the experimental signal and was shown in Figure 5-46(c). The filtered signal has shown a residual pulse with an amplitude of about 11 gausses and a duration of 2.6 inches.

Referring to Table 5-2, a flaw of range of *7-9 percentage of section loss* is expected with a *length of about 1/3 of an inch*. Moreover, the flaw is located at a distance of about 4 inches from the first stirrup and outside of two stirrups. From Figure 5-33, it is anticipated to have a flaw with an overall volume of 6×10^{-4} in^3, which is corresponding to a third of an inch long flaw with about 7% section loss.

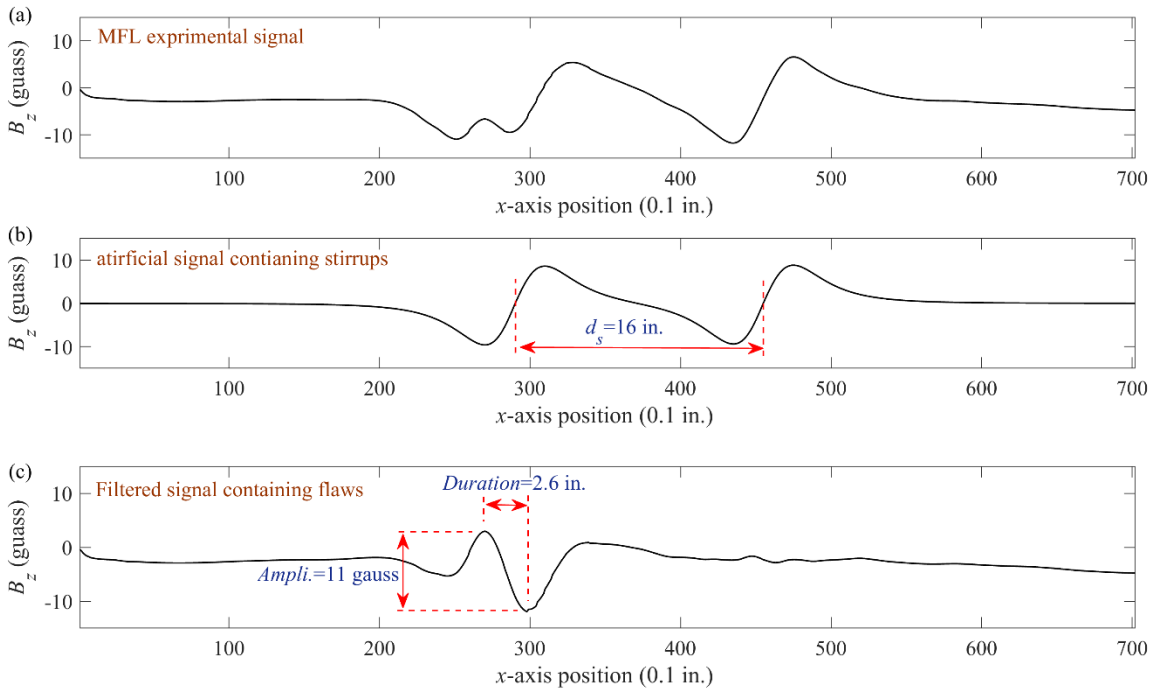

Figure 5-46: 2-D analysis of MFL for channel #19 for example 2

Chapter 6 **Summary and Future Works**

In this study, a non-destructive evaluation method is developed to detect corrosion of ferrous components in pre-stressed concrete girders. The method utilizes the magnetic flux leakage (MFL) phenomenon in which the magnetic field leaks out in a magnetically saturated region in the presence of an abrupt volumetric change of ferrous materials under test.

6.1 **Summary**

- The MFL concept application in prestressed concrete members is elaborated through experiments and numerical simulations by ANSYS MAXWELL.
- The experimentation was designed based on effective parameters on the MFL signals such as the stirrups' size and spacing, the flaws' properties, and the embedment length of strands.
- The numerical simulation was conducted using ANSYS MAXWELL and verified by experimental result. A few cases of investigation were generated using numerical simulation.
- After confirming the superposition of individual effects on MFL signals, an analytical method was developed that enabled a thorough comparative study of the effects of flaws on the MFL signals.
- 3-D analysis of MFL signal was developed in which the arrangement of stirrups, including spacing and the orientation angle, is determined through performing correlation analysis on signals given from all channels of the MFL apparatus.

- The 3-D analysis gives an approximation of the flaw's location about the position of flaws along with the girder and which strand contains a flaw.

- 2-D analysis was conducted on the MFL signal given from a specific channel, which was identified by 3-D analysis as the channel closest to the flaw. The 2-D analysis determined the amplitude and duration of what? after removing the stirrups' pulses from the MFL signal.

- Sets of tables and graphs were provided for estimation of the flaws' properties based on amplitude, duration, and embedment length of strands. These tables and graphs were prepared by results given from experiments and numerical simulation.

- Since the 2-D analysis determines the magnitudes and duration associated with flaws, the geometrical properties of flaws, such as section loss percentage and length, are obtained from the provided tables (graphs) as small as 2.38% of section loss.

- The flaw detection methodology presented in this study is based on experimental results done on flaws with section losses in the range of 2.36-16.67% percent and stirrups spacing of 12 and 16 inches. Several depths of magnets from strands were examined as 2.25, 3.0, 4.0 and, 6.0 inches.

6.2 **Future works:**

The analysis of vertical component of magnetic field was the main focus of this study. In comparison to horizontal component, the vertical component has a simpler pattern in addition to producing a larger amplitude variation that makes it more appropriate for signal analysis. One disadvantage of working with the vertical component of the magnetic field is having similar pattern

of variation for both stirrups and flaws, which imposes some complexity for distinguishing between stirrups and flaws. Since the magnetic signal patterns for stirrups and flaws are dissimilar when the horizontal component of the field is considered, it would be helpful to extend this work to consider this effect. This method of data analysis normally encounters more complex magnetic signal patterns, but it could enhance the flaw detection accuracy and reliability using the MFL technique.

This study was based on an experimentation for a range of flaw sizes, a pre-defined stirrups size, spacing and, orientation angles in addition to specific embedment lengths of strands within concrete bridge girders. In real inspection cases, it is likely to face additional configurations of stirrups and strand, flaw shapes and sizes, depths of embedment, or even different inspection systems with varying parameters like the magnet powers, and sensor sensitivities. Considering these variables, it will be advantageous to employ advanced pattern recognition-based methodologies such as machine learning or deep learning. These techniques would be able to regulate such variations of MFL signals to develop a more general, but automated, methodology that would be applicable to a vast range of flaws, stirrups, magnets, and test samples.

Chapter 7 **References**

Antipov, A. G., & Markov, A. A. (2014). Evaluation of transverse cracks detection depth in MFL rail NDT. *Russian Journal of Nondestructive Testing*, *50*(8), 481–490. https://doi.org/10.1134/S1061830914080026

ARTBA Bridge Report. (2020). Retrieved May 29, 2021, from https://artbabridgereport.org/reports/2021-ARTBA-Bridge-Report.pdf

Azari, H., Ghorbanpoor, A., & Shams, S. (2020). Development of Robotic Nondestructive Testing of Steel Corrosion of Prestressed Concrete Bridge Girders using Magnetic Flux Leakage System. *Transportation Research Record: Journal of the Transportation Research Board*, 036119812092547. https://doi.org/10.1177/0361198120925471

Beattie, A. (2013). *Acoustic emission non-destructive testing of structures using source location techniques.* Albuquerque, NM, and Livermore, CA (United States). https://doi.org/10.2172/1096442

Belblidia, F., Michael Cameron, I., Sienz, J., Zhang, L., Cameron, I., Sienz, J., … Pearson, N. (2015). Influence of Specimen Velocity on the Leakage Signal in Magnetic Flux Leakage Type Nondestructive Testing . *Journal of Nondestructive Evaluation*. https://doi.org/10.1007/s10921-015-0280-1

Bridge Replacement Unit Costs 2020 - Federal Highway Administration. (n.d.). Retrieved May 29, 2021, from https://www.fhwa.dot.gov/bridge/nbi/sd2020.cfm

Demma, A., Evans, M., Alleyne, D., Fong, J., Vogt, T., & Vine, K. (2007). Guided Wave

Training and Certification. In *5th International Conference on Certification and Standardization in NDT - Lecture 20*. London.

Elyasigorji, A., Rezaee, M., & Ghorbanpoor, A. (2019). Magnetic Corrosion Detection in Concrete Structures. In *International Conference on Sustainable Infrastructure 2019* (pp. 175–184). Reston, VA: American Society of Civil Engineers. https://doi.org/10.1061/9780784482650.018

Elyasigorji, A., Rezaee, M., & Ghorbanpoor, A. (2020). Characterization of Corrosion in PS Concrete Girders by Correlation Analysis. In *Structures Congress 2020 - Selected Papers from the Structures Congress 2020* (pp. 285–292). American Society of Civil Engineers (ASCE). https://doi.org/10.1061/9780784482896.027

Ghorbanpoor, A., Steber, G. B., & Shew, T. E. (1991). *Evaluation of steel in concrete bridges : the Magnetic Field Disturbance (MFD) System*. U.S. Dept. of Transportation, Federal Highway Administration.

Ghorbanpoor, Al, Borchelt, R., Edwards, M., & Abdel Salam, M. (2000). *MAGNETIC-BASED NDE OF PRESTRESSED AND POST-TENSIONED CONCRETE MEMBERS - THE MFL SYSTEM*. Federal Highway Administration.

IAEA. (2013). *Training Guidelines in Non-Destructive Testing Techniques: Manual for Visual Testing at Level 2*. Vienna. Retrieved from https://www-pub.iaea.org/MTCD/Publications/PDF/TCS_54_web.pdf

James Li, C., & Li, S. Y. (1995). Acoustic emission analysis for bearing condition monitoring. *Wear*, *185*(1–2), 67–74. https://doi.org/10.1016/0043-1648(95)06591-1

Kamaitis, Z. (2002). Damage to concrete bridges due to reinforcement corrosion: Part II-design considerations. *Transport*, *17*(5), 163–170. https://doi.org/10.1080/16483840.2002.10414037

Krause, H. J., Wolf, W., Glaas, W., Zimmermann, E., Faley, M. I., Sawade, G., … Krieger, J. (2002). SQUID array for magnetic inspection of prestressed concrete bridges. *Physica C*, *368*, 91–95. https://doi.org/10.1016/S0921-4534(01)01145-5

Lohith, M. (2009). *Ultrasonic Non Destructive Testing*.

Mandal, K., & Atherton, D. L. (1998). A study of magnetic flux-leakage signals. *Journal of Physics D: Applied Physics*, *31*(22), 3211–3217. https://doi.org/10.1088/0022-3727/31/22/006

Manson, G., Worden, K., Holford, K., & Pullin, R. (2001). Visualisation and Dimension Reduction of Acoustic Emission Data for Damage Detection. *Journal of Intelligent Materials Systems and Structures*, *12*(8), 529–536. https://doi.org/10.1177/10453890122145375

Okolo, C. K., & Meydan, T. (2018). Pulsed magnetic flux leakage method for hairline crack detection and characterization. *AIP Advances*, *8*(4), 047207. https://doi.org/10.1063/1.4994187

Park, S. H., Kim, J. W., Nam, M. J., & Lee, J. J. (2012). Magnetic Flux Leakage Sensing-Based Steel Cable NDE Technique Incorporated on a Cable Climbing Robot for Bridge Structures. *Advances in Science and Technology*, *83*, 217–222. https://doi.org/10.4028/www.scientific.net/ast.83.217

Park, S., Kim, J. W., Lee, C., & Lee, J. J. (2014). Magnetic flux leakage sensing-based steel cable NDE technique. *Shock and Vibration*, *2014*. https://doi.org/10.1155/2014/929341

Permeh, S., Vigneshwaran, K. K. K., Echeverría, M., Lau, K., & Lasa, I. (2018). Corrosion of post-tensioned tendons with deficient grout, part 2: Segregated grout with elevated sulfate content. *Corrosion*, *74*(4), 457–467. https://doi.org/10.5006/2568

Radiographic Testing – SITAS. (n.d.).

Rockley, J. C. (1977). INDUSTRIAL RADIOGRAPHY. *Electronics and Power*, *23*(4), 321–325. https://doi.org/10.1049/ep.1977.0176

Sawadw, G., & Krause, H, -J. (2010). Magnetic fl ux leakage (MFL) for the non- destructive evaluation of pre-stressed concrete structures. In *Non-destructive evaluation of reinforced concrete structures.* Oxford: Woodhead: Boca Raton : CRC Press.

Schumacher, T. (2009). *Title: New Acoustic Emission Applications in Civil Engineering*.

Shi, Y., Zhang, C., Li, R., Cai, M., & Jia, G. (2015). Theory and Application of Magnetic Flux Leakage Pipeline Detection. *Sensors*, *15*(12), 31036–31055. https://doi.org/10.3390/s151229845

Usamentiaga, R., Venegas, P., Guerediaga, J., Vega, L., Molleda, J., & Bulnes, F. (2014). Infrared Thermography for Temperature Measurement and Non-Destructive Testing. *Sensors*, *14*(7), 12305–12348. https://doi.org/10.3390/s140712305

Verstrynge, E., Lacidogna, G., Accornero, F., & Tomor, A. (2021, January). A review on acoustic emission monitoring for damage detection in masonry structures. *Construction and Building Materials*. Elsevier Ltd. https://doi.org/10.1016/j.conbuildmat.2020.121089

Wang, Z. D., Gu, Y., & Wang, Y. S. (2012, February). A review of three magnetic NDT technologies. *Journal of Magnetism and Magnetic Materials*. North-Holland. https://doi.org/10.1016/j.jmmm.2011.08.048

Zhou, J., Qiu, J., Zhou, Y., Zhou, Y., & Xia, R. (2018). Experimental study on residual bending strength of corroded reinforced concrete beam based on micromagnetic sensor. *Sensors (Switzerland), 18*(8). https://doi.org/10.3390/s18082635

Chapter 8 **Curriculum Vitae**

Educational Backgrounds:

- Ph.D. Candidate: Civil Engineering**,** University of Wisconsin-Milwaukee, GPA=3.954 (Spring 2015-present) Dissertation Title: "MFL- Based Detection of Flaws of Prestressed Concrete Girders".
- M.Sc.: Civil Engineering, Shahrood University of Technology (Fall2004-Spring 2007)

  Thesis Title: "Application of Graph Theory (Laplacian Matrix) in Stability Analysis of Structures".
- B.Sc.: Civil Engineering, Shahrood University of Technology (Fall 2000-Spring2004)

Professional Experiences:

- Working as a Co-Op Engineer, ECS Limited Inc. (Summer 2019)
- CEO (Chief Executive Officer) of Construction Firm (Firm Title: Arshad Niyaresh Sazeh (ANS), Iran, Mazandaran Province (Spring 2010- Fall 2014)
- Mentor of Students worked as an Internship Students (Fall 2007- Fall 2014)
- Inspector Engineer: Buildings of Behshahr City (Both Design and Supervision) (2009- 2012); certified supervisor of construction site to assess the construction codes requirements implementation.
- Architectural and Structural Designer and supervisor: Buildings Over 70000 $m^2$and up to the 8-Story Buildings (2007- Fall 2014); as a consultant for architectural design; manager of structural design team; lead inspector in construction site to assess the implementation of constructional codes.
- Structural Designer: Steel Framed Flour Factory with an Area over 4000 m^2,Iran, Mazandaran Province, Neka (2010); manager of structural design team.
- Architectural and Structural Designer and Supervisor: Rural Buildings of Behshahr City, Job Appointed by Government (2010); as a consultant for architectural design; manager of structural design team; lead inspector in construction site to assess the implementation of construction codes.
- Structural Designer: Arvin Bana Consulting Engineering Inc. (2008); structural design using SAP2000 & ETABS software.
- Structural Designer: Sepehrar Consulting Engineering Inc. (2008); structural design using SAP2000 & ETABS software.
- Internship: 240 Hours working, Drawing of As-Built Plots, Retrofitting and Surveying of some Structurers, Municipality of Behshahr City, Mazandaran Province (Summer 2003)

Certificates:

- FE (Fundamental Engineering Exam): NCEES, Board of Wisconsin. (Spring 2020)
- Nuclear Gauge Safety, Troxler Electronic Laboratories Inc. (Summer 2019)
- ACI Concrete Field-Testing Technician – Grade I (Summer 2019)
- Hazmat Transportation Safety, Required by U.S DOT and IATA, Troxler Electronic Laboratories Inc. (Summer 2019)
- Employment Licensure, Privilege to Work as a Designer and Supervisor: Grade 1 in Civil Engineering (highest Engineering Grade) of Iran Construction of Engineering Organization (IRCEO) which is Equivalent to Have FE (Fundamentals of), PE (Professional Engineer), and SE (Structural Engineering), Licensed by "Ministry of Roads, Housing, and Urban Development", Mazandaran Province, Iran (2007-present)
- Chemical Hygiene Plan (CHP) and Laboratory Safety, UWM (Fall 2015)

- The Following Certificates Were Obtained from "Ministry of Roads, Housing, and Urban Development" and "Iran Construction of Engineering Organization (IRCEO)":
- Modern Technology of the Intelligent Buildings, Improvement and Optimization of the Foundation Systems (Aug 2014); Energy Management; The Role of Consulting Engineers in the Construction (July 2014); Strengthening of Foundation and Undergoing Soils (Feb 2011); New Technologies of the Intelligent Construction (Nov 2011); Supervision over Construction of Steel Structures, Contractor (Construction project) Obligations (Feb 2010); Precautions Throughout Building Operations (Jan 2010); Geotechnical Seismic, General Principles of Engineering Services (Dec 2009); Construction Methods of Foundations, Geotechnical and Foundation Design (Nov 2009); Significant Points of Designing Steel Structures, Introduction to the Construction Materials (Sep 2009); Buildings with Masonry Constructions (Oct 2009); Welding Inspection (Apr 2008); Responsibilities of an Operating Engineer, Excavation and retaining Walls(Feb 2007)
- Athletic: Taekwondo, Blue Belt (2012)

Computer Skills:

- Design: ETABS, SAP, SAFE; Applied: AutoCAD, Revit
- Familiar with MATLAB* and ANSYS Maxwell*, LabView*
- Frequent Use of Microsoft Office Package and Photoshop
- In progress: ABAQUS

* Applied in my Dissertation at UWM, (Thesis Title: MFL-Based Detection of Flaws of Prestressed Concrete Girders), MATLAB also used in my Master thesis.

Teaching Experiences:

- Teaching Assistant, UWM, (Covered Some Chapters as an Instructor in each Semester Rather than Course Professor), Course Title: CE 372- Introduction to structural Design (Spring2015- Spring 2020)
- Instructor, UWM, Course Title: Strength of Material (summer 2017)
- Instructor, Iran, National and Islamic Azad Universities:
- Courses Titles: Static, AutoCAD, Geology and Construction Materials, Applied Drawing, Applied Software (ETABS, SAP, SAFE), Design of Concrete and Steel Structures, Mechanics of Materials, Structural Analysis, Laws and Relations of a Construction Site, Wood Structures, Technical Drawing, Maintenance of Structures, Management and Equipment of a Construction Site, Concrete Structures, Open Channel Hydraulics (Fall 2005- Fall 2014)
- Some Courses Passed in UWM as a Ph.D. Student: Finite Element Methods, Design of Steel Structures, CEAS Graduate Seminar, Advanced Steel Design, Analysis and Design of Bridges, Advanced Strength of Materials, Advanced Engineering Math II

Honors and Awards:

- UWM Distinguished Dissertation Fellowship (DDF): Recognized as an Elite Graduate Scholar at UWM (Fall 2020 & Spring 2021)
- Graduate Student Excellence Fellowship (GSEF): Recognized as an Elite Graduate Scholar at UWM (Fall 2019 & Spring 2020)
- Scholars Emergency grant (Summer 2020)
- UWM Graduate School Travel Award (Fall 2020& Spring 2021)
- Chancellor's Graduate Student Award, UWM (Spring 2021, Spring 2020, Spring 2019, Fall 2018, Spring 2017, Fall 2017, Spring 2016, Fall 2016, Fall 2015)
- Awarded Winner of Student Research Poster Competition, UWM –College of Engineering and Applied Science (Spring 2017)

- Tuition Waiver Award for bachelor's degree of Civil Engineering, Shahrood University of Technology (2000-2004)
- Tuition Waiver Award for master's degree of Structural Engineering, Shahrood University of Technology (2004-2007)
- Honored as the First Civil Engineer Woman and the First Civil Engineer Achieved Master of Civil-Structural Engineering among Civil Engineers of Behshahr City, "Iran Construction of Engineering Organization", Mazandaran Province (Spring 2009)

* Athletic: Ranked 1st in the Wrist Wrestling Cup Contests among women students at Shahrood University of Technology (Fall 2001)

* Athletic: Ranked 1st in the Physical Fitness Contests among women students at Shahrood University of Technology (Fall 2000)

Research Interests:

Non-Destructive Evaluation Methods, Electromagnetic Fields, Applied Mathematics on Structural Engineering like Graph Theory, Multiphysics Simulations and Numerical Methods such as Finite Element Methods (FEM)

Publications:

- Rezaee Maysam, Li-Chih Tsai, Azam Elyasigorji, Muhammad Istiaque Haider, Armin Yazdi, and Nathan P. Salowitz. "Quantification of the Mechanical Strength of Thermally Reduced Graphene Oxide Layers on Flexible Substrates". https://doi.org/10.1016/j.engfracmech.2021.107525, Engineering Fracture Mechanics (Spring 2021)
- Elyasigorji Azam, Rezaee Maysam, Ghorbanpoor Al "Characterization of Corrosion in Prestressed Concrete Girders by Correlation Analysis, ASCE Structural Congress (SEI), "Selected to be Presented in the Conference", USA (Spring 2020)
- Elyasigorji Azam, Rezaee Maysam, Ghorbanpoor Al, "Magnetic Corrosion Detection in Concrete Structures", ASCE International Conference on Sustainable Infrastructures, Los Angles, California, USA (Fall 2019)
- Rezaee M., Elyasigorji A., Elyasigorji S., "Analytical Evaluation of Inter-Story Beam Effects on Lateral Stiffness of Moment Frames", 10th International Congress of Civil Engineering, Tabriz, West Azarbaijan, Iran (2015)
- Elyasigorji A., Rezaee M., Elyasigorji F., "The Assessment of Eigenvalues Using New Graph and Laplacian Matrix of Form II", 8th National Congress of Civil Engineering, Tabriz, West Azerbaijan, Iran (2014)
- Elyasigorji F., Rezaee M., Elyasigorji A., "Influence of Persian Garden as Urban Green Space on Promotion of Social Interactions Citizens; Case Study: Garden Chehel Sotun (Mellat Park) of Behshahr City", Journal of Civil Engineering and Urbanism (JCEU) (2014)
- Elyasigorji A., Mansour Khaki A., Shariatmohaymany A., Sadatibaladehi S. H., "The Methodology for Reconstruction Significance of Transportation Network Links Under the Flood Damage", Life Sci J;10(6s):211-221, (2013)
- Elyasigorji A., Rahimi S., "An Efficient Method for Identifying Laplacian Spectrum", 38th International Conference of Mathematics, Zanjan University, Zanjan, Iran (2007)
- Azam Elyasigorji, Al Ghorbanpoor, "Magnetic Flux Leakage Signal Characterization for Detection of Corrosion in Prestressed Concrete Girders", NDT& E International Journal (submitted Spring 2021)
- Maysam Rezaee, Azam Elyasigorji, and Nathan P. Salowitz. "Cohesive Zone Characterization Using Semi-Nonlinear analysis of peel test." Composite Science and Technology (2021) (In Preparation).

Presentations:

- Magnetic Flux Leakage Signal Characterization for Detection of Corrosion in Prestressed Concrete Girders, TRB 2021 Annual Meeting, Poster Presentation, USA (January 2021)
- Elyasigorji Azam, Rezaee Maysam, Ghorbanpoor Al, "Magnetic Corrosion Detection in Concrete Structures", ASCE International Conference on Sustainable Infrastructures, Poster, Los Angles, California, USA (Fall 2019)
- MFL Based Detection of Flaw of Prestressed Concrete Girders, 3 Minute Thesis, UWM, (Spring 2019)
- Corrosion Detection by Magnetic Flux Leakage in Reinforced Concrete Beams Using the Transient 3D FEM Simulations, 3 Minute Thesis, UWM, (Spring 2018)
- MFL signals of the Reinforced Concrete Girders, Student Research Poster Competition, UWM (College of Engineering and Applied Science) (Spring 2018)
- Corrosion Detection by Magnetic Flux Leakage in the Reinforced Concrete Beams Using 3D Transient FEM Simulations, Student Research Poster Competition, UWM– College of Engineering and Applied Science (Spring 2017)
- Application of Laplacian Matrix in Stability Analysis of Structures with Symmetry to the Forms of Two and Three, Shahrood University of Technology (Spring 2007)
- Assessment of Eigenvalues Using New Graph and Laplacian Matrix of Form II, Shahrood University of Technology (Spring 2006)

Leadership, Performances, and Memberships:

- Director of UWM Startup Challenge, Co-Curricular Mentorship Scholastic of Helmet Challenge of Electrical and Mechanical Students, Funded by National Science Foundation (NSF) I-Corps for Interactive Art Startup, New NFL Helmet's Shape (Design Several 3D-Printed and Creative Prototypes, and Design Hardware Kit (Spring 2020)
- Assistant Coordinator, Contribution in providing of ABET Files for Professors, Faculty members, and TAs at UWM (Fall 2019)
- Collaboration in writing a book in the field of Structural design for CE372 Course, Supervisor: Professor Habib Tabatabai (Summer 2015- Spring 2016)
- Participation in Student Startup Challenge Primer, held for 3 days at Entrepreneurship Building at UWM (Summer 2019)
- Contribution to Milwaukee Choir Project, It Was the First "Choir Project" Held in UW-Milwaukee, UWM (Spring 2019)
- Member of ASCE, American Society of Civil Engineers (Spring 2019- Present)
- Participation in the ASCE/SEI Conference, Florida, Orlando Spring (2019)
- Vice- President of Structural Engineering Society at UWM (2018- Present)
- Active Member of UWM Panther Executive in Pink Organization, its Aim is to Empowering People Who are Underrepresented to Encourage and Back them in Executive Roles (Spring 2019- Summer 2020)
- Member of Basketball Team of UWM (Spring 2019)
- Contribution in Organizing GRAPES (Grid-connected Advanced Power Electronic Systems) Conference, An NSF Funded Program, held at UWM Continuing Education Center (May 2017)
- Mentoring UWM Bachelor Students to Cast and Test the Concrete Specimens (Fall 2015- Spring 2020)
- Member of the Society of Women Engineers at UWM (SWE) (2015-present)
- Member of the Construction Firm (Firm Title: Arshad Niyaresh Sazeh (ANS), Iran, Mazandaran Province (Fall 2010- present)
- Member of the "Iran Construction of Engineering Organization" of Mazandaran Province and Iran (2007-Present)
- Member of the "Construction Engineering Association" of Behshahr City (2007- Present)

- Commission Member of Education in the “Construction of Engineering Association” of Behshahr (2010-2014)
- Member of the Poetry and Literature Association of Shahrood University of Technology (2000- 2007)
- Member of Engineers’ Swimming Association of Behshahr City (2008- 2014)

Extracurricular Interests

Dance, Paragliding, Gliding, Rock Climbing, Mountain Climbing, Hiking, Swimming, Taekwondo, Basketball, Philosophy, Mathematics, Poem, and Choir